POLITECNICO DI TORINO

Master's Degree in Biomedical Engineering

Master's Degree Thesis

Development and Characterization of Wearable Raman Scattering System for Optical Biosensing

Supervisors

Prof. Danilo DEMARCHI

Prof. Sandro CARRARA

Eng. Ata GOLPARVAR

Candidate

Marco FRANCHINI

March 2023

Abstract

Recent advancements in wearable technology have led to a significant improvement in personalized health monitoring. Researchers in biosensing are developing innovative devices and techniques for analyzing biomolecules, such as lactate, glucose, uric acid, DNA, and antibodies, to diagnose and monitor diseases and biological processes. A promising area of research is Raman scattering-based optical biosensing, a non-destructive, label-free analytical technique that identifies chemical compounds enabled by the inelastic scattering of light. This method has been widely utilized in several fields, such as biology, chemistry, and medicine. Indeed, the potential of Raman spectroscopy in detecting chemical compounds and properties of biomolecules is driving the development of new biosensor platforms based on the Raman effect.

Translating bulky bench-sized or handheld Raman spectroscopy instruments to Wearable systems is crucial for the usability of optical Raman biosensing. They allow for continuous monitoring of biomolecules in real-time, providing more accurate information about a person's health status and eliminating the need for frequent sample collection and analysis. These systems can improve the efficiency and cost-effectiveness of healthcare delivery and patient outcomes, especially for those with chronic conditions or those in remote or resource-limited settings.

This research was conducted at the Bio/CMOS Interfaces Laboratory (BCI) at EPFL Neuchâtel, Switzerland. The aim of the thesis was to address the current limitations in the field of wearable technology by developing a wearable proof-of-concept Raman scattering-based biosensing system. The research resulted in the development of an 8.8 x 9.5 x 6.7 cm^3 prototype using innovative 3D printing techniques, which allowed for a modular design that facilitated the easy placement of components and flexible mountings for optics. In addition, we also developed a laser driver and optimized the temperature control system for the laser source using the well-established Nichols-Zeigler method. This ensures the device's operation with optimal efficiency and accuracy. The completed wearable platform and its results are presented, showcasing the device's suitability for biosensing. The thesis also provides a comprehensive comparison of the benefits and drawbacks of the wearable Raman spectroscopy configuration compared to other optical wearables.

Keywords: Wearable Technology, Personalized Health Monitoring, Biosensing, Biomolecules, Raman Scattering-Based Optical Biosensing, Chemical Compounds, Inelastic Scattering of Light, Biosensor Platforms, Continuous Monitoring, Healthcare Delivery, Patient Outcomes, Chronic Conditions, 3D Printing, Modular Design, Laser Driver, Temperature Control System, Nichols-Zeigler Method.

Sommario

Gli ultimi progressi nella tecnologia indossabile hanno notevolmente migliorato il monitoraggio personalizzato della salute. I ricercatori nel campo del biosensing stanno sviluppando dispositivi e tecniche innovative per analizzare biomolecole come lattato, glucosio, acido urico, DNA e anticorpi, al fine di diagnosticare e monitorare le malattie e i processi biologici. Un'area di ricerca promettente è il biosensing ottico basato sulla diffusione Raman, una tecnica analitica non distruttiva e senza etichetta che identifica i composti chimici attraverso la diffusione anelastica della luce. Questo metodo è stato ampiamente utilizzato in diverse discipline, come la biologia, la chimica e la medicina. Il potenziale della spettroscopia Raman nel rilevare i composti chimici e le proprietà delle biomolecole sta portando allo sviluppo di nuove piattaforme di biosensori basati sull'effetto Raman.

Il passaggio da ingombranti strumenti di spettroscopia Raman da banco o portatili in sistemi indossabili è fondamentale per l'usabilità della biosensibilità ottica Raman. Essi consentono il monitoraggio continuo delle biomolecole in tempo reale, fornendo informazioni più precise sullo stato di salute di una persona ed eliminando la necessità di raccogliere e analizzare frequentemente i campioni. Questi sistemi possono migliorare l'efficienza e l'economicità dell'erogazione dell'assistenza sanitaria e i risultati dei pazienti, soprattutto per coloro con condizioni croniche o che si trovano in contesti remoti o con risorse limitate.

Questa ricerca è stata condotta presso il Bio/CMOS Interfaces Laboratory (BCI) dell'EPFL a Neuchâtel, Svizzera. L'obiettivo della tesi era quello di affrontare le attuali limitazioni nel campo della tecnologia indossabile, sviluppando un sistema di biosensing indossabile basato sulla diffusione Raman. La ricerca ha portato allo sviluppo di un prototipo di 8.8 x 9.5 x 6.7 cm^3 utilizzando tecniche innovative di stampa 3D, che hanno permesso un design modulare che ha facilitato il posizionamento dei componenti e il montaggio flessibile delle ottiche.

Inoltre, abbiamo anche sviluppato un driver laser e ottimizzato il sistema di controllo della temperatura per la sorgente laser, utilizzando il consolidato metodo Nichols-Zeigler. Questo garantisce il funzionamento del dispositivo con efficienza e precisione ottimali. La piattaforma indossabile completata e i suoi risultati sono

presentati, mostrando l'idoneità del dispositivo per il biosensing. La tesi fornisce anche un confronto completo dei vantaggi e degli svantaggi della configurazione della spettroscopia Raman indossabile rispetto ad altri dispositivi ottici indossabili.

Acknowledgements

I would like to express my sincere appreciation to my relator and co-relator, Prof. Demarchi and Prof. Carrara, for their exceptional guidance, mentorship, and unwavering support throughout this thesis journey. I am also deeply grateful to my thesis supervisor, Ata, for entrusting me with his research work and for sharing with me every secret on Raman spectroscopy. Furthermore, I would like to extend my gratitude to the entire Bio/CMOS Interfaces Laboratory (BCI) group at EPFL for creating a welcoming and collaborative research environment. The countless coffee breaks and mental breakdowns have made this journey all the more memorable.

Table of Contents

List of Tables xiii

List of Figures xiv

Acronyms xxi

1 Wearable Raman System 5
- 1.1 Raman spectroscopy: principles and physics . . . 5
  - 1.1.1 Quantum theory . . . 7
- 1.2 Wearable optical sensing methodology . . . 8
  - 1.2.1 Functional near-infrared spectroscopy (fNIRS) . . . 8
  - 1.2.2 Near infrared spectroscopy (NIRs) . . . 10
  - 1.2.3 Diffuse optical tomography (DOT) . . . 13
  - 1.2.4 Optical coherence tomography (OCT) . . . 15
  - 1.2.5 Time-of-flight mass/Terahertz Time-Domain spectrometry (TOF/THz-TDS) . . . 18
- 1.3 State of art in compact Raman systems . . . 21
  - 1.3.1 Smartphone/Handheld Raman System . . . 21
  - 1.3.2 Portable Raman System . . . 24
  - 1.3.3 Wearable Raman System . . . 27
  - 1.3.4 Home-made Raman system . . . 31

2 Design and characterization of Raman laser driver 37
- 2.1 Temperature effects on laser performance . . . 38
- 2.2 Thermoelectric cooler (TEC) systems . . . 41
- 2.3 PID optimization . . . 42
  - 2.3.1 Nichols–Zeigler optimization method . . . 43
  - 2.3.2 Optimization results . . . 46
- 2.4 Final system test . . . 48
  - 2.4.1 40 mW custom-made configuration . . . 49
  - 2.4.2 Commercial butterfly laser . . . 51

3 3D Printed Wearable Raman Prototype 53
3.1 Introduction to Different 3D Printing Techniques 54
3.1.1 Fused Deposition Modeling (FDM) 54
3.1.2 MultiJet Modeling (MJM) 56
3.1.3 Digital Light Processing (DLP) 58
3.2 Optomechanics Design 60
3.3 Optics 64
3.4 Wearable Device Design 65
3.4.1 First prototype 65
3.4.2 Final prototype 68

4 Results 71

5 Conclusions and Future Developments 77
5.1 Limitations and Future Developments 78

A Additional Content 79
A.1 PID optimization 79
A.2 Laser test 84

Bibliography 89

List of Tables

1.1 This table provides a comprehensive overview of the key information gathered during our literature review on wearable Raman systems. It allows for easy comparison of the different strategies developed by various research groups across a range of applications, providing a valuable resource for understanding the current state of the field and identifying potential areas for further exploration. 36

3.1 Here are presented the costs of all the optics components 64

4.1 This table provides an overview of the characteristic Raman bands observed for each compound analyzed in our work. Furthermore, the table includes a brief explanation of the peak assignment, providing an insight into the molecular vibrations responsible for the Raman scattering signal [164, 165, 166, 167, 168, 169, 16]. 73

List of Figures

1.1 Idealised model of Rayleigh scattering and Stokes and anti-Stokes Raman scattering. E_{AS}, energy of anti-Stokes photon; E_R, energy of Rayleigh scattered photon; E_S, energy of Stokes photon; E_{vib}, energy of molecular vibrational transition, after ref. [28] 7

1.2 The NIRS-EEG prototype comprises various parts such as fNIRS-EEG caps (A), a control module (B), optodes for gathering signals from superficial layers (C), and a specific optode design (D). The spatial sensitivity profile, generated using AtlasViewer software, is provided for each measurement channel for both visual (top) and language (bottom) tasks (E). The prototype design includes the integration of EEG electrodes between NIRS sockets (red arrows) and openings in the cap (green arrows) to facilitate better removal of dense long hair, reprinted from [39]. 9

1.3 (a) This figure illustrates the process of measuring the reflected light (I) from an arterial blood vessel, known as photo-plethysmography (PPG) signal. The measurement is taken at multiple optical wavelengths to obtain the PPG signal. (b)The figure also shows the decomposition of PPG signal into its different components for further examination, reprinted from [35]. 12

1.4 (a) A photograph from the side of a baby wearing a cap with small tiles over the left side of the head. The photograph shows the Velcro straps that connect the cap to the infant's head, running over the middle of the head. (b) A single image of a cloud of points, taken at the same time as the photograph in (a), of the same infant. (c) A complete 3D model of the infant, created from numerous point cloud images, including milestones on the skull (green points) and areas of the light sources (magenta points). (d) The positions of the light sources (red points) and detectors (blue points) are shown on a six-month-old anatomical atlas model that has been registered to the subject. (e) A 2D representation of the full array of 12 tiles, showing channels with source-detector separation of approximately 45 mm or less, reprinted from [51]. 15

1.5 A compact and wearable diagnostic imaging device that utilizes OCT technology. (a) The device includes a broadband laser source, a collimator, a capture button, a diffraction grating, a fiber coupler, a galvano scanner, a lens, a liquid crystal display, a line scanning camera, a mirror, a polarization controller, and a sample. (b) Example of the wearable OCT system working. r, reprinted from [60]. 17

1.6 (a) Metamaterial biosensor schematic illustration: THz beams routinely incident via the biosensor on which the MDA MB 231 cell was cultivated; (b) the metamaterial biosensor construction. The geometrical parameters are as follows: l1 = l2 = 20 mm, r1 = 5 mm, r2 = 1.5 mm, and t = 15 m; (c) a double U-shaped metamaterial structure. The geometrical parameters are as follows: p1 = p2 = 44 m, w1 = w2 = 36 m, w3 = 2 = 0 m, and g = 4 m; (d) physical picture of 4-inch biosensor; (e) physical photograph of 20 20 mm biosensor; and (f) micrograph of the metamaterial, reprinted from [88]. 20

1.7 (A) detailed illustration of XITM showing the components of the A1 smartphone by CloudMinds, including the laser output, Raman optical module, electronic control board, and casing. Additionally, (B) a diagram is provided to demonstrate how SERS measurement is performed using the clever SERS terminal, adapter, and SERS chips., after ref. [94, 93]. 23

1.8 Example of portable Raman system (A) BRAVO system [89] and (B) portable Raman-Spectrometer Cora 100 [106]. 27

1.9 Two example of wearable Raman system from (A) the University of Missouri [115], and (B) from MIT research group [116]. 29

1.10 (A) A diagram is provided to show the design of a wearable SERS patch sensor that is capable of label-free detecting drug molecules in sweat. [107], and (B) illustration of using this highly scalable and wearable technology for surface-enhanced Raman spectroscopy. [117]. 30

1.11 (A) An illustration of the top view of the in-house built Raman spectrometer system, (B) a labeled and assembled version of the system, and (C) a fully assembled 3D printed Raman spectrometer., reprinted from [120]. 33

2.1 Experimental evidence in the literature of the impact of temperature on (A) Wavelength and (B) Laser power, reprinted from [132, 133] . 40

2.2 Experimental evidence of the impact of temperature on (A) Wavelength and (B) Laser power. 41

2.3 A schematic illustration of (A) a thermoelectric cooler (TEC), (B) a thermoelectric power generator (TEG) and (C) a thermoelectric module, reprinted from [139] 42

2.4 Figure A presents the control system response with the P-Gain held constant and the I-term adjusted, while figure B displays the control system response with the I-term held constant and the P-Gain adjusted 45

2.5 Experimental setup designed to enhance and optimize the temperature control system with real-time visualization of temperature changes, providing instant verification of the control system's response. 46

2.6 Flow diagram depicting the implementation process of the Nichols-Zeigle optimization method. 46

2.7 Figure illustrates the results of the experiment aimed at characterizing the system before PID optimization. 47

2.8 This figure illustrates the outcome of the optimized PID system performance. Figure A demonstrates the improvement in overshoot reduction and time response, while Figure B presents a characterization experiment showcasing the system's response to multiple-step temperature inputs. 47

2.9 This figure illustrates the two different heat dissipations solution adopted. In figure A the in-house-build configuration while in figure B the butterfly laser module structure: 1 – laser crystal, 2 – monitor photodiode, 3 – thermistor, 4 – thermoelectric cooler, 5 – collimating lens, 6 – collecting lens, 7 – optical isolator, 8 – electrical leads. . . 48

2.10 This figures presents the results of the experiment in which the 40 mW laser was tested without the use of a temperature control system. Figure A displays the dynamic relationship between Power and Temperature over the course of the experiment, presenting a clear illustration of the fluctuations in both variables over time. Meanwhile, Figure B explores the correlation between Power and Temperature, offering a deeper understanding of how changes in one variable impact the other. 49

2.11 This figures presents the results of the experiment in which the 40mW laser was tested without the use of a temperature control system. Figure A displays the dynamic relationship between Power and Temperature over the course of the experiment, presenting a clear illustration of the fluctuations in both variables over time. Meanwhile, Figure B explores the correlation between Power and Temperature, offering a deeper understanding of how changes in one variable impact the other. 50

2.12 This figure presents the results of the experiment in which the butterfly laser was tested with the use of the optimized temperature control system. Figure A displays the dynamic relationship between Power and Temperature over the course of the experiment, presenting a clear illustration of the stability in both variables over time. Meanwhile, Figure B explores the correlation between Power and Temperature, offering a deeper understanding of how changes in one variable impact the other. 51

2.13 In this figure is possible to evaluate an eventual peak shift aviation during the time for (A) butterfly laser and (B) 40mW DPSS laser. . 52

3.1 Primary elements of an FDM printer are depicted in the figure. The movement in the x, y, and z directions can be accomplished through the motion of the extrusion head (represented by purple arrows) or the build platform (represented by green arrows), or a combination of both. For example, movement in the x and y directions is carried out by the extrusion head while the build platform accomplishes movement in the z-direction. Reprinted from [148] 55

3.2 Schematic illustration of a MJM 3D printer. Reprinted from [153] . 57

3.3 Schematic illustration of a stereolithography (SLA) and digital light processing (DLP) 3D printer. Reprinted from [157] 59

3.4 This figure provides a visual comparison of three different optics mounting solutions, with each solution utilizing a different method for holding the lens in place. (a) a ring stopper is used to fix the lens in position. (b) utilizes a flexible material to hold the lens in position. (c) employs a more traditional screw stopper to hold the lens in place. 60

3.5 (a) presents the 3D model of the second prototype for the lens mounter. This model was developed using TPU, with a protrusion on the base of the mounter to hold the lens securely in place. (b) shows the proof-of-concept constraint mechanism developed to test the functionality of the mounting solution. This mechanism was designed with a hole insertion point for the mounted lens, which allowed us to control the optics path using the platform design. . . 63

3.6 (a) presents the 3D model of the third prototype for the lens mounter. (b) shows the actual model was developed using E-gum, with a protrusion on the base of the mounter to hold the lens securely in place. 63

3.7 Schematic of the first wearable prototype optics. 67

3.8 3D model of (A) the first wearable Raman system prototype and (B) optic platform. 67

3.9 Actual prototype of (A) the first wearable Raman system prototype and (B) optic platform. 68

3.10 Schematic of the final wearable prototype optics. 69

3.11 The 3D model shown in this figure represents the second version of the wearable Raman system, which showcases the integration of the butterfly commercial laser, the CMOS sensor, and the band connectors, the focusing lens, dichroic mirror, and filters. 69

3.12 The actual all-in-one wearable device worn by a subject using an elastic band. 70

4.1 In this figure is shown the experimental setup we designed and constructed to explore its behaviour. 71

4.2 The figure represents the Raman spectrum of several chemical compounds that are involved in many biochemical reactions. 72

4.3 This figure presents a comprehensive overview of the results obtained from the solutions analyzed using our wearable Raman system. In fig. a, several spectra of fluorescence papers were obtained. In fig. b, the Raman spectrum of olive oil solution acquired with our wearable Raman system is compared with the spectrum obtained using a commercial Raman system and the spectrum sourced from literature (fig. c). The Raman spectra of Urea solutions at 5 M and 2.5 M both with (fig. d) and without (fig. e) a bandpass filter were also analyzed. 75

Acronyms

SERS
Surface Enhanced Raman Spectroscopy

AgNPs
Silver Nanoparticles

AuNPs
Gold Nanoparticles

CCD
Charge-Coupled Device

API
Active Pharmaceutical Ingradients

fNIRS
Functional near-infrared spectroscopy

NIR
Near-infrared

NIRS
Near-infrared spectroscopy

OCT
Optical coherence tomography

DOT
Diffuse optical tomography

TOF

Time-of-flight mass spectrometry

THz-TDS

Terahertz Time-Domain Spectroscopy

CNNs

Convolutional Neural Networks

OP

Optical Polarimetry

MEMS

Micro-Electromechanical Systems

PID

Proportional-integral-derivative

TEC

Thermoelectric cooler

N-Z

Nichols-Zeigler

NTC

Negative Temperature Coefficient

DPSS

Diode-Pumped Solid-State

PCB

Printed Circuit Board

FDM

Fused Deposition Modeling

MJM

MultiJet Modeling

DLP

Digital Light Processing

ABS

Acrylonitrile butadiene styrene

TPU

Thermoplastic polyurethane

EFL

Effective focal length

Introduction

Recent innovations in wearable technology have led to an incredible breakthrough in personalized health monitoring. In the field of biosensing, researchers are working to develop devices and techniques for detecting and analyzing biomolecules, such as lactate, urea, glucose, creatinine, uric acid, pesticides, hydrogen peroxide, DNA and antibodies to diagnose and monitor diseases, as well as various other biological processes [1, 2, 3]. One promising area is optical biosensing and, in particular, Raman scattering-based optical biosensing, which is a non-destructive analytical technique that uses the inelastic scattering of light to identify chemical compounds. The potential of Raman spectroscopy methods in detecting chemical compounds, as well as structural and functional properties of biomolecules, is driving the rising interest in the development of novel platforms for the use of Raman spectroscopy techniques in biosensor technologies [4]. Raman spectroscopy has been widely used in various fields such as chemistry for ultrasensitive chemical analysis [5], biology to identify different species and interpret physiological and metabolic responses to environmental stressors [6], and medicine for detecting pre-malignant lesions [7].

A wearable Raman system is crucial for biosensing applications because it allows for continuous monitoring of biomolecules in real-time, providing more accurate and detailed information about a person's health status [8, 9]. Furthermore, it eliminates the need for frequent sample collection and analysis, which can be invasive, time-consuming, and costly [10]. Wearable Raman systems can be especially useful in monitoring patients with chronic conditions, such as diabetes [11], who require frequent monitoring but may not need to be hospitalized [12]. These systems can also be useful in monitoring patients who have been discharged from the hospital but still need to be closely monitored to ensure that their condition does not worsen [13]. Additionally, wearable Raman systems can be useful in remote or resource-limited settings where traditional diagnostic equipment is not available. As the total healthcare load rises and hospital bed deficits cause hastened discharges, there is growing interest in the use of remote monitoring in the outpatient context [12]. Overall, wearable Raman systems have the potential to improve the efficiency and cost-effectiveness of healthcare delivery while also improving patient outcomes. Although there has been a growing interest in wearable technology, for instance, for

non-invasive glucose monitoring or sweat analysis [14], it is currently rare (if not impossible) to find a Raman scattering-based biosensing unit that is fully integrated into a wearable device. Most of the proposed sensors in this field have only a small part that is attached directly to the skin, such as the sensor itself, while the rest of the device, including the Raman spectrometer, laser, and beam shaping optics, is not worn by the patient and is connected via optical fiber or directly laser light is perturbated to skin focused with objective using a handheld device [15]. This raises the question of whether it is accurate to refer to these devices as truly "wearable". Indeed, wearable technologies are referred to self-contained electronic devices designed to be worn on the body. They are characterized by having all their components, such as sensors, processors, and displays, integrated into a compact, wearable case, enabling convenient and comfortable use for the user in their daily activities.

Therefore, the goal of this thesis is to address this gap in the current field of wearables and to introduce a noval optical biosensors platform by developing, and characterizing a wearable Raman scattering-based biosensing system that can be worn for biosensing applications, specifically in in situ analysis such as sweat biomarker monitoring or transdermal in vivo analysis such as blood glucose monitoring. The proposed device will be a major step forward in the field of wearable optics and non-invasive bio-sensing, as it aims to ensure the device is truly wearable and convenient for the user. Additionally, this research aims to evaluate the benefits and drawbacks of a wearable Raman spectroscopy configuration in comparison to traditional biochemical sensors and other wearable devices, such as infrared and near-infrared spectroscopy or optical coherence tomography. The data obtained from the tests were analyzed to determine the feasibility of using this device in a real-world setting and to identify potential areas for improvement. To

achieve this goal, in this work we have used different 3D printing techniques for the realization of the prototype of this device, we managed to create a list of all the components that were needed, and we have also worked on the optimization of the temperature control system for cooling down the laser source. To be more specific, in chapter 1 you will find extensive literature research on the subject using different keywords and analyzing the characteristics of each type of wearable/portable biosensing optical system. In chapter 2, we optimize the temperature control system for this specific application, including a description of the cooling system used for the laser and results from testing with different power lasers. Chapter 3 explores various 3D printing techniques that were utilized in the production of optomechanical parts, with detailed descriptions provided. The results of the completed wearable Raman platform are presented in chapter 4. Finally, chapter 5 offers final thoughts and future perspectives on the topic. We anticipate by developing a truly wearable Raman system, we can provide valuable insights into

the health and well-being of the user, and potentially revolutionize the field of biosensing.

Chapter 1

Wearable Raman System

1.1 Raman spectroscopy: principles and physics

Raman spectroscopy is a method that exploits the inelastic scattering of light by a compound to offer comprehensive information about its chemical structure and bonding [8]. When a molecule is hit by light of a given frequency, a tiny fraction of the light is scattered at a different frequency owing to the activation of vibrational, rotational, or other low-frequency modes of the molecule [16]. This difference in frequency is known as the Raman shift, which is directly connected to the energy of the excited mode. The following equation can describe the Raman effect:

$$I(\omega_s) = I0(\omega_s) + B|E(\omega_s)|^4 * S(\omega_s, \omega_i) \tag{1.1}$$

Where I(ω_s) is the intensity of the scattered light at frequency ω_s, I0(ω_s) is the background intensity, B is the Raman scattering coefficient, E(ω_s) is the electric field of the scattered light, and S(ω_s,ω_i) is the Raman scattering cross-section. The Raman shift, that is the difference in frequency between the incident and scattered light, is directly related to the energy of the excited mode and can provide information about the vibrational modes of the molecule [16]. The Raman cross-section is a measure of the ability of a molecule to scatter incident radiation and produce a Raman effect. It represents the probability that a photon interacts with a molecule and causes a Raman scattering event. The Raman cross section is related to the polarizability of a molecule, which describes how easily a molecule's electron cloud can be distorted by an electric field [17]. The Raman scattering coefficient represents the number of Raman scattering events per unit volume of sample per unit time per unit solid angle per unit incident power [17].

The Raman effect is a second-order nonlinear optical process that occurs when light

interacts with a material in such a way that the material's nonlinear susceptibility is proportionate to the square of the light's intensity [18]. A second-order nonlinear optical process is a phenomenon in which two photons interact with a material in a way that results in the generation of a new photon with twice the energy (and half the wavelength) of the incident photons [19]. This process is governed by the second-order nonlinear susceptibility of the material, which describes the material's response to an applied electric field. The Raman effect is a relatively weak process, which is typically on the order of 1 in 10^6 of the incident light [20]. This means that Raman spectroscopy is a challenging technique, as it requires the use of intense and stable light sources, which in the past made the technique difficult and expensive to use. Furthermore, Raman spectroscopy has been historically less popular than other techniques like absorption spectroscopy which are faster and less expensive [21]. Raman spectroscopy and its associated methods are now being widely used in various fields of research and are becoming common techniques in both academic and industrial research labs [22]. An example is On-chip Raman which refers to the integration of Raman spectroscopy onto a microchip or integrated circuit (IC). This technology allows for the miniaturization of Raman spectrometers, making them more portable, efficient, and cost-effective. On-chip Raman systems typically use waveguides or resonators to confine the excitation laser light and collect Raman scattered light and can be integrated with other components, such as microfluidics, to enable real-time and on-site analysis of samples [23].

A variety of techniques can be employed to analyze Raman spectra, such as peak fitting, principal component analysis (PCA), linear discriminant analysis (LDA) and univariate data processing [24]. These methods help in extracting in-depth information about the vibrational modes of a molecule and identifying unknown compounds. Univariate data processing specifically, involves analyzing individual variables or features in a data set without considering the relationships between them [24]. In Raman spectroscopy, this technique is commonly used to process raw spectra by removing noise, correcting the baseline and smoothing the data, making the spectral features more visible. This step is crucial in obtaining a clear and accurate representation of the Raman spectrum, which is necessary for proper analysis.

In summary, Raman spectroscopy is a strong analytical method that is based on the inelastic scattering of light by a molecule. The Raman effect is a second-order nonlinear optical process that can provide detailed information about the chemical structure and bonding of a molecule, and it is typically used with a laser as the excitation source and analyzed using various techniques such as peak fitting, principal component analysis and linear discriminant analysis.

1.1.1 Quantum theory

The approach to Raman scattering based on quantum theory acknowledges that the energy of vibrations in a molecule is quantized [25]. Normal vibrations in a non-linear molecule are 3N-6, whereas normal vibrations in a linear molecule are 3N-5, where N indicates the number of atoms in the molecule [26].

Any of these vibrations' energy is quantified using the following relationship:

$$E_\nu = h\nu(\nu + 1/2) \tag{1.2}$$

where ν is the frequency of the vibration and ν is the vibrational quantum number, which controls the energy of that particular vibration and has values of 0, 1, 2, 3, and so on [25].

Quantization is introduced into the Raman scattering theory using perturbation theory. Simple words, this method entails perturbing the ground state molecule wavefunctions until new wavefunctions that characterize the vibrationally excited state are achieved. The transition from the ground state is then accomplished by a perturbing wave function, that is the sum of the perturbations applied [27]. This perturbing wavefunction will have associated energy and serves as a valuable graphical representation of Raman scattering, with vibrational transitions occuring through this virtual energy level [27].

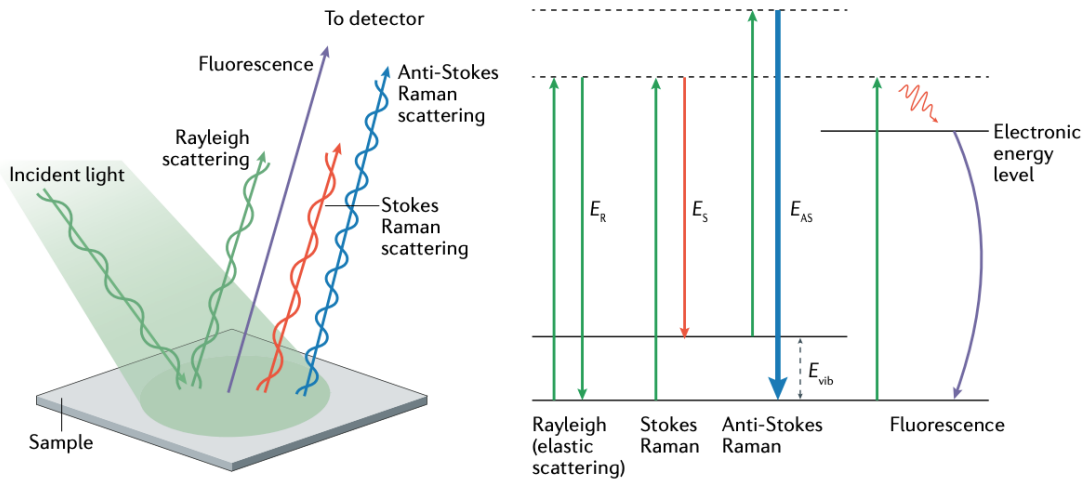

Figure 1.1: Idealised model of Rayleigh scattering and Stokes and anti-Stokes Raman scattering. E_{AS}, energy of anti-Stokes photon; E_R, energy of Rayleigh scattered photon; E_S, energy of Stokes photon; E_{vib}, energy of molecular vibrational transition, after ref. [28]

Rayleigh scattering is triggered by transitions that begin and end at the same vibrational energy level. Stokes Raman scattering occurs as a result of transitions from the ground state vibrational energy level to a higher vibrational energy level, while anti-Stokes Raman scattering occurs as a result of a shift from a higher to a lower vibrational energy level [29]. Because most molecule vibrations are in the ground state ($\nu = 0$) at typical ambient temperature, anti-Stokes transitions are far less inclined to occur than Stokes transitions, leading in more strong Stokes Raman scattering [29][30]. This increased relative intensity grows as vibrational energy rises, and the higher vibrational energy levels is less inhabited at any specific temperature. As a result, the Stokes-Raman scattering is often researched and suggested in Raman spectroscopy [30].
[31]

1.2 Wearable optical sensing methodology

In addition to Raman spectroscopy, there are other non-invasive wearable optical sensing techniques that have been developed for monitoring various physiological parameters. These include functional near-infrared spectroscopy (fNIRS) [32], near infrared spectroscopy (NIRS) [32], diffuse optical tomography (DOT) [33], and optical coherence tomography (OCT) [34]. It should be noted that fNIRS and NIRs have made significant advancements in recent years in terms of developing wearable platforms for real-time biosensing and monitoring of brain activity [35, 36]. These advancements have opened up new possibilities for research and practical applications in fields such as neuroscience, psychology, and medicine. Each of these approaches has advantages and disadvantages but they all have the same goal: to measure physiological data in real time. While Raman spectroscopy has its own unique advantages, such as the ability to identify specific chemical compounds and detect small changes in molecular vibrations, other techniques like fNIRS and DOT provide deeper insights into changes in neural and hemodynamic activity [37, 38]. On the other hand, OCT offers high-resolution images of tissue microstructure. All of these techniques have specific applications and can be used in combination to gain a more comprehensive understanding of physiological processes.

1.2.1 Functional near-infrared spectroscopy (fNIRS)

Wearable functional near-infrared spectroscopy (fNIRS) is a non-invasive optical sensing procedure that is used to monitor various physiological parameters in real-time. The method depends on the absorption of near-infrared (NIR) light by haemoglobin and deoxyhemoglobin, which allows for the assessment of changes in

oxygenated and deoxygenated blood in the brain.

The physics of fNIRS is based on the principle of near-infrared spectroscopy. NIR light, which has a wavelength range of 700-1100 nm, is able to penetrate through the skull and scalp and reach the brain tissue. Haemoglobin and deoxyhemoglobin have distinct absorption spectra in the NIR range, which allows for measuring changes in oxygenated and deoxygenated blood in the brain. By measuring the changes in NIR light absorption, fNIRS can provide information about neural and hemodynamic activity in the brain.

Wearable fNIRS systems are designed to be worn by the subject and are used to take measurements in naturalistic environments. These systems typically consist of multiple optodes placed on the scalp, and a data acquisition unit. The optodes contain both emitters that emit NIR light, and detectors that measure changes in light absorption. The data acquisition unit is responsible for collecting and analyzing data from the optodes.[39] [40]

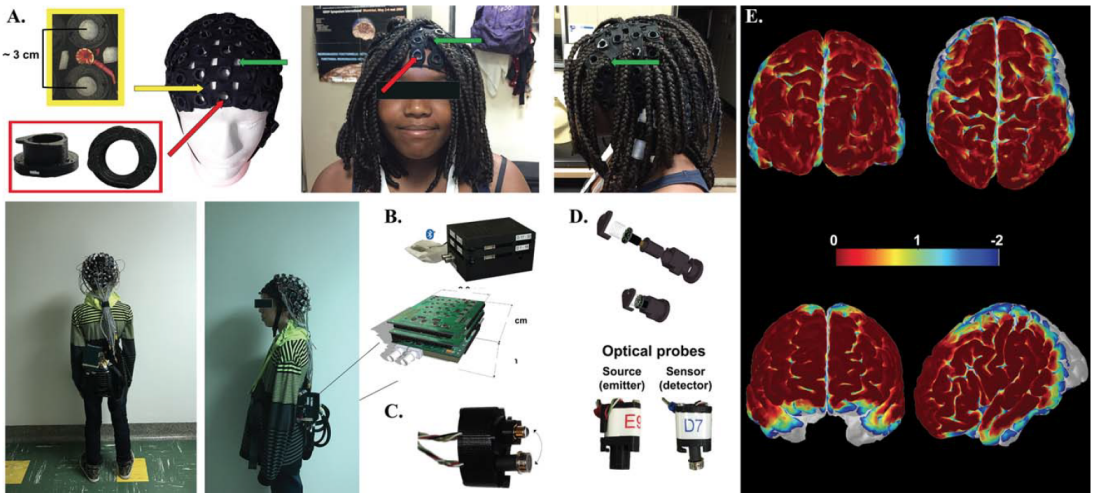

Figure 1.2: The NIRS-EEG prototype comprises various parts such as fNIRS-EEG caps (A), a control module (B), optodes for gathering signals from superficial layers (C), and a specific optode design (D). The spatial sensitivity profile, generated using AtlasViewer software, is provided for each measurement channel for both visual (top) and language (bottom) tasks (E). The prototype design includes the integration of EEG electrodes between NIRS sockets (red arrows) and openings in the cap (green arrows) to facilitate better removal of dense long hair, reprinted from [39].

A major key benefits of fNIRS is that it is non-invasive method, which means that it doesn't involve any puncturing or breaking of the skin or mucous membranes, and

does not require any surgical procedures. Additionally, fNIRS allows for real-time monitoring of neural and hemodynamic activity in the brain, providing insights into brain function in naturalistic settings. Portable fNIRS systems can be worn by the subject, making it easy to take measurements in naturalistic environments and allowing for more flexibility in study design. Furthermore, it is relatively cost-effective compared to other neuroimaging techniques.

However, fNIRS also has some limitations, such as its limited penetration depth, sensitivity to motion artifacts, low spatial resolution, and lack of information about the chemical composition of brain tissue. It also has a relatively low temporal resolution compared to other neuroimaging techniques, making it difficult to study fast dynamics in the brain. Despite these limitations, fNIRS is still a powerful tool for understanding brain function in various populations and different settings.

Compared to Raman spectroscopy, fNIRS provides a deeper understanding of changes in neural and hemodynamic activity, but it doesn't allow for the identification of specific chemical compounds. Additionally, it doesn't allow for the detection of small changes in molecular vibrations like Raman spectroscopy does. Furthermore, fNIRS is typically more sensitive to changes in the concentration of oxygenated and deoxygenated haemoglobin, while Raman spectroscopy is more susceptible to changes in the chemical composition of the tissue. In terms of frequency used, fNIRS uses NIR light with a wavelength range of 700-1100 nm, while Raman spectroscopy uses laser light in the visible, near-infrared, or infrared range. Additionally, fNIRS uses detectors such as photodiodes, while Raman spectroscopy uses detectors such as CCD or CMOS cameras. In terms of size, fNIRS systems are typically designed to be worn by the subject, while Raman systems can vary in size from portable handheld devices to laboratory-based systems.

In summary, while fNIRS and Raman spectroscopy are both non-invasive approaches that can be operated to study the brain, they have different strengths and weaknesses. fNIRS is better suited for monitoring changes in neural and hemodynamic activity, while Raman spectroscopy is better suited for identifying specific chemical compounds and small changes in molecular vibrations in the tissue. Both techniques have their own unique applications and can complement each other in various fields such as in medical diagnostics, neuroscience and biochemistry.[36]

1.2.2 Near infrared spectroscopy (NIRs)

In recent years, there has been a growing interest in near-infrared (NIR) spectroscopy due to advancements in instrumentation and data analysis, as well as the introduction of optical fibers that allow for the delivery and transfer of NIR energy

and information [41].

Near-infrared spectroscopy (NIRs) is a non-invasive method that employs the theories of spectroscopy to detect the absorption of near-infrared light by the body. The concept behind NIRs is that various molecules absorb different wavelengths of light, and by detecting the quantity of light absorbed at various wavelengths, it is possible to calculate the concentration of individual components in a mixture [42].

The Lambert-Beer law, which says that the absorbance of a material is exactly proportional to the concentration and the path length by which the light travels, drives NIRs. The Beer-Lambert Law is frequently employed to analyze NIRS data and calculate the concentrations of various compounds in a sample [42].

A further key fundamental in NIRs is the idea of light scattering. Whenever light is transmitted through a substrate, it may be dispersed by molecules in the substrate, which can change the intensity of the light hitting the detector. This scattering may be categorized as either elastic or inelastic, based on whether the dispersed light carries the same or different energy as the incoming light, respectively. In NIRS, inelastic scattering is often induced by vibrations of the chemical bonds in the molecules in question [43].

To summarize, the NIRS physics fundamentals are founded on the Beer-Lambert Law, which is applied to understand light absorption by various compounds, and the idea of light scattering, which may change the light's intensity arriving at the sensor. These concepts, when combined, allow for the non-invasive detection of particular molecule concentrations in a substance using NIRS.

There are several works in the literature highlighting how powerful this methodology is in the wearable biosensing field, most of all non-invasive continuous glucose detection [35][44].

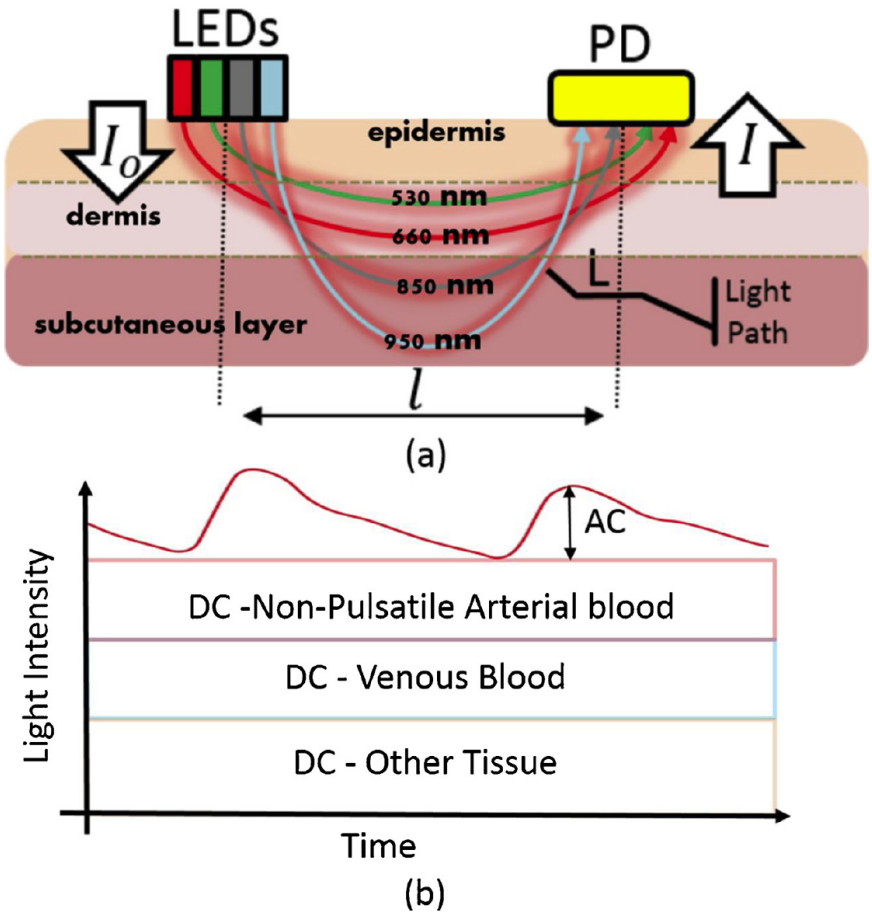

Figure 1.3: (a) This figure illustrates the process of measuring the reflected light (I) from an arterial blood vessel, known as photo-plethysmography (PPG) signal. The measurement is taken at multiple optical wavelengths to obtain the PPG signal. (b)The figure also shows the decomposition of PPG signal into its different components for further examination, reprinted from [35].

One of the primary benefits of NIRs systems is that they are non-invasive [44]. They can detect biological signals without puncturing, making them less uncomfortable and less dangerous for the consumer. Furthermore, NIRs systems have a high sensitivity, allowing for the early diagnosis of illnesses or the monitoring of health issues [45]. Because of their inexpensive cost, NIRs systems are accessible to a broad variety of consumers [46]. Moreover, NIR systems are portable and may be worn or carried by the user, making them suitable for daily usage [35].

However, there are several drawbacks to adopting NIRs devices for biosensing. One restriction is that NIRs devices can only detect signals from the top layers of the

skin due to their restricted penetration depth [47]. As a result, they are less helpful for perceiving impulses deeper inside the body. Furthermore, NIRs devices may be impacted by external variables such as environmental light and temperature, making precise readings challenging [48]. Data analysis is very complicated, and non-experts may struggle to comprehend the data [49]. Finally, the implementations of NIRs systems are presently restricted to measuring blood oxygenation and blood glucose levels, but they may be used in other fields in the future.

1.2.3 Diffuse optical tomography (DOT)

DOT, or Diffuse Optical Tomography, is a method of non-invasive imaging that uses near-infrared light to acquire information about the physiology of thick biological tissues [50]. It works by using NIR light in the wavelength range of 600-1000 nm measuring the absorption and scattering characteristics of the tissue, which are then used to create images of the internal structures and physiology of the tissue.

NIR light is able to penetrate through tissue because it has a longer wavelength than visible light and is less absorbed by the tissue. When NIR light enters the tissue, it interacts with chromophores, such as haemoglobin and water, and also gets scattered by the tissue. The interaction of light with the tissue is dependent on the concentrations of chromophores and the microstructure of the tissue.[34]

DOT uses this information to create images of the tissue by measuring the intensity of the light that is transmitted through the tissue. These images are not structural like those created by X-rays or MRI, but rather, they provide information about the physiology of the tissue [50]. DOT has been used to image a wide variety of biological tissues including brain, breast and skin and has been used to study a variety of physiological processes such as blood flow, oxygenation and metabolism. [33]

A wearable DOT system is a wearable device, such as a wristband or clothing item, that integrates DOT technology. These systems aim to provide real-time monitoring of the physiology of biological tissues by continuously measuring the tissue's absorption and scattering properties. This information can then be used to create images or provide physiological information about the tissue. Wearable DOT systems have the potential to revolutionize medical care by providing continuous, non-invasive monitoring of tissue physiology, early detection of disease, and promoting personalized medicine [51].

One of the major advantages of DOT is its non-invasive nature [33]. Unlike X-ray, MRI, or CT, DOT does not require ionizing radiation or a contrast agent, making it safer for patients and allowing for more frequent use without negative side effects. This is particularly beneficial for sensitive populations such as children or pregnant

women. Another advantage of DOT is its high temporal resolution [52]. DOT can measure physiological processes in real-time, which allows for the monitoring of dynamic changes in psychiatry. This feature is particularly useful in monitoring conditions that change rapidly, such as brain activity or blood flow. DOT systems are also relatively small and portable, making it possible to use them in a variety of settings, including hospitals, clinics, and even in the field [53]. This makes DOT accessible to a wider range of patients and healthcare providers, particularly in remote or resource-poor areas where other imaging modalities are not available. In addition, DOT is cost-effective compared to other imaging methodologies such as MRI or CT. This can make a significant difference in healthcare systems where costs are a major concern. Another advantage of DOT is its multi-modality feature. DOT can be combined with other imaging modalities, such as MRI or CT, to provide complementary information [54]. This can help to provide a more complete sight of the physiology of the tissue being imaged, which can improve diagnostic accuracy and treatment planning.

However, there are also some limitations to DOT. One major limitation is its low spatial resolution. The images created by DOT are not as detailed as those created by X-ray, CT, or MRI, which can make it difficult to visualize small structures or lesions [55]. Another limitation of DOT is the complexity of data analysis. The images created by DOT are not straightforward to interpret and require sophisticated data analysis techniques. This can make it challenging to obtain accurate results, especially in the hands of untrained operators [56]. DOT is also limited in its depth penetration. It is limited to imaging shallow tissue structures and is not able to image deep structures such as bone [57]. Additionally, DOT is limited by the optic properties of the tissue being imaged and is not able to image certain types of tissue such as bone or metal.

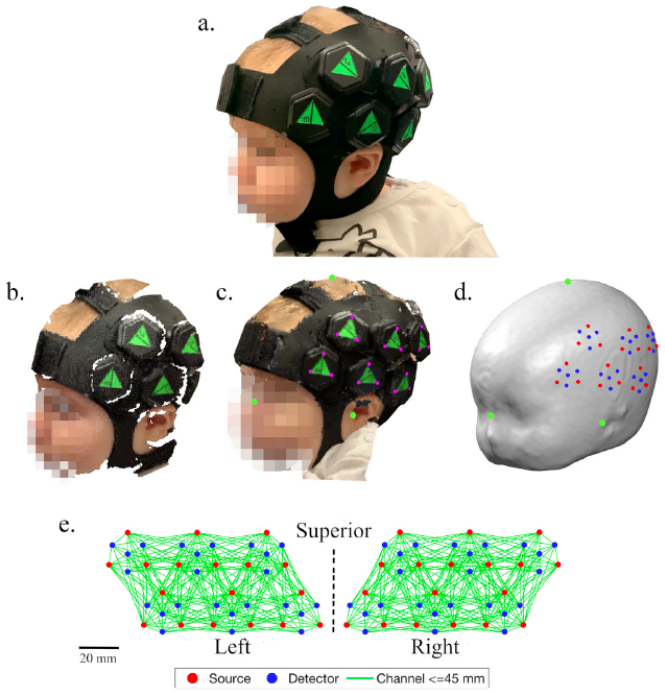

Figure 1.4: (a) A photograph from the side of a baby wearing a cap with small tiles over the left side of the head. The photograph shows the Velcro straps that connect the cap to the infant's head, running over the middle of the head. (b) A single image of a cloud of points, taken at the same time as the photograph in (a), of the same infant. (c) A complete 3D model of the infant, created from numerous point cloud images, including milestones on the skull (green points) and areas of the light sources (magenta points). (d) The positions of the light sources (red points) and detectors (blue points) are shown on a six-month-old anatomical atlas model that has been registered to the subject. (e) A 2D representation of the full array of 12 tiles, showing channels with source-detector separation of approximately 45 mm or less, reprinted from [51].

1.2.4 Optical coherence tomography (OCT)

OCT is a procedure of creating detailed, cross-sectional images of the retina using light waves, without the need for invasive procedures. It is based on the principle of low-coherence interferometry, which makes it possible to measure the scattering of light within biological tissue at different depths.

The OCT system typically uses a light source, typically a superluminescent diode (SLD) or a swept-source laser, a beam splitter, a sample arm, and a detection arm. The source emits a low-coherence light, which is divided by the beam splitter into

two beams: the sample beam and the reference beam. The light in the sample arm interacts with the tissue and scatters, while the light in the reference arm is directed onto a mirror placed at a fixed distance. The backscattered light from both arms is then combined and directed to a detector.

The detector records the interference pattern between the sample and reference beams, which is caused by the difference in the distance that the light travels in each arm. This difference is determined by the depth of scattering within the tissue. The interference pattern can then be analyzed to determine the scattering properties of the tissue at different depths by studying the phase and amplitude of the pattern.

Wearable OCT technology is the utilization of OCT imaging systems that can be worn or affixed directly to the body, enabling continuous or recurrent imaging of the eye or other body parts without the need for the patient to stay in a stationary position.

There are several different designs for wearable OCT devices, for example, contact lens design involves the integration of OCT imaging technology into a contact lens, allowing for continuous imaging of the eye without the need for the patient to remain in a fixed position [58]. Additionally, there is a head-mounted device design, where a head-mounted device, such as a pair of goggles, that contains the OCT imaging technology is used, allowing for continuous imaging of the eye without the need for the patient to remain in a fixed position [59]. There is also a handheld device design, where a handheld device that contains the OCT imaging technology is used, allowing for more portability and ease of use, but the patient has to be still to get the image[59]. Another design that has been developed is a compact, wearable diagnostic imaging modality employing optical coherence tomography for in situ plant leaf quality assessments. This system is capable of diagnosing infected leaves at the initial disease stages. The design concept involves a versatile backpack-type imaging modality with a compact spectrometer, miniature computer, rechargeable power source, and handheld inspection probe [60]. And finally, a smartphone-based device design, where a smartphone-based device that contains OCT imaging technology is used, allows for more portability and ease of use, but the patient has to be still to get the image [61].

Traditional OCT technology is well-established and widely used in clinical settings. It provides high-resolution, cross-sectional images of the retina and other ocular structures, and it has revolutionized the field of ophthalmology [33][56]. One of the main advantages is its capability to provide continuous monitoring of the eye's health, which can provide more information about the progression of the disease and the effectiveness of treatment. Additionally, wearable OCT can also be used for imaging other parts of the body, such as skin, blood vessels, and organs, making

it a versatile technology [51, 53]. Another advantage of wearable OCT is that it is non-invasive and can be used in a convenient manner, as it does not require patients to remain in a fixed position, it also can be used for remote monitoring which can be beneficial for patients living in remote areas or for those who are unable to travel.

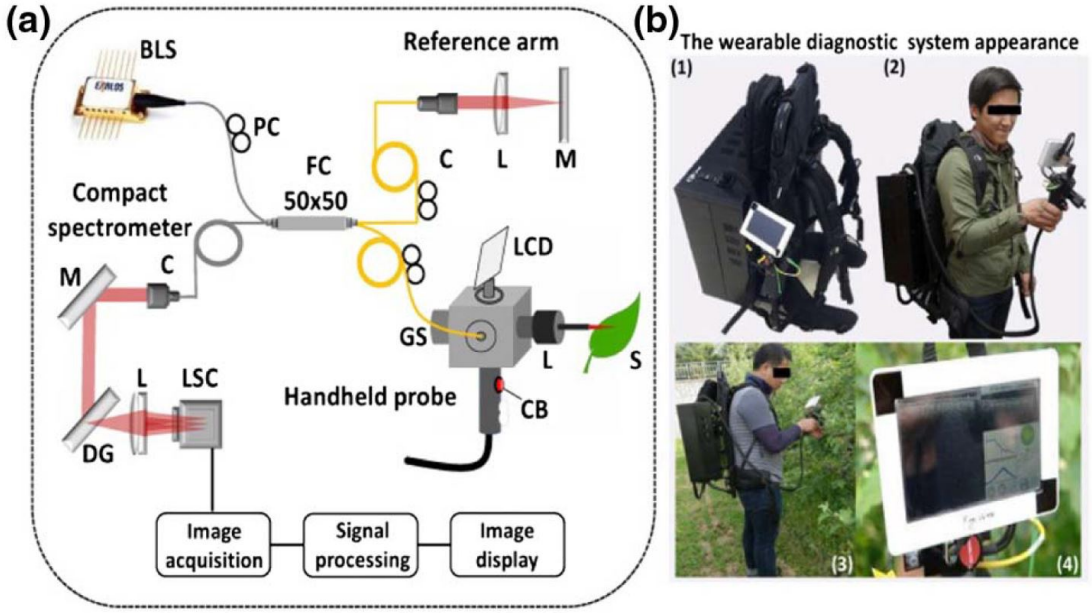

Figure 1.5: A compact and wearable diagnostic imaging device that utilizes OCT technology. (a) The device includes a broadband laser source, a collimator, a capture button, a diffraction grating, a fiber coupler, a galvano scanner, a lens, a liquid crystal display, a line scanning camera, a mirror, a polarization controller, and a sample. (b) Example of the wearable OCT system working. r, reprinted from [60].

However, there are also some disadvantages to wearable OCT technology, such as lower spatial resolution compared to traditional OCT systems, image quality may be affected by motion artifacts [38], as the patient is not fixed during the imaging process, size of the technology, as it is still in the process of miniaturization, the devices might be bulky, and the power consumption could be an issue, which can limit the duration of imaging and make it difficult for patients to wear for extended periods of time [51]. Additionally, the accuracy and precision of wearable OCT technology may be affected by factors such as alignment and focus, which can be more challenging to control in a wearable device compared to traditional OCT systems. Furthermore, there are challenges to overcome such as power consumption [62], the need to improve the signal-to-noise ratio [63], and more onerous optical

design and data storage [64]. Additionally, the cost and size of the technology are also significant challenges that need to be overcome before wearable OCT can be widely adopted [65].

1.2.5 Time-of-flight mass/Terahertz Time-Domain spectrometry (TOF/THz-TDS)

Time-of-flight mass spectrometry (TOF) spectroscopy works by producing a burst of particles or light and measuring the time it requires for the particles (or light) to go and come back from a detector. Using the known distance and the recorded time-of-flight, the velocity, energy, or mass may then be computed. Ions generated by a brief ionization event are accelerated by an electric field, gaining the same kinetic energy, and then move along a drift route to the detector. The lighter ions arrive first, and the mass spectrum is recorded. Measuring the flight period of each ion enables us to calculate their mass to charge ratios [66].

TOF spectroscopy is used to research the structure and composition of substances in domains such as chemistry [67], biology [68], and geology [69]. The method is also employed in quality control and material testing to measure coating thickness and uniformity [70].

Time-of-flight (TOF) spectroscopy has potential uses in in vivo biosensing, where it may be used to analyze biological material rapidly and non-invasively [71]. TOF spectroscopy may be employed in this way for real-time monitoring of medication kinetics, to optimize drug administration and improve treatment outcomes illness diagnostics, and biological imaging, to monitor changes in the molecular composition of biological samples over time, providing valuable information about the progression of disease [72]. TOF spectroscopy's excellent precision and sensitivity [73] make it ideally suited for in vivo biosensing applications requiring accurate measurements of biochemical markers, measuring, for instance, the concentration of biomarkers in biological fluids, such as blood or urine, to diagnose a range of conditions, including cancer and cardiovascular disease [74, 75]. Furthermore, the technique's non-invasive nature makes it suitable for in vivo application and decreases the potential of tissue injury.

However, there are significant disadvantages to using TOF spectroscopy in biosensing. One significant restriction is that the process requires a somewhat sophisticated setup, which includes specialized equipment and software [76]. Some academics and practitioners may find it challenging to utilize successfully as a result of this. Furthermore, the technique's capacity to probe deep into biological tissues is restricted, making it less helpful for some kinds of studies [77]. Finally, the procedure is susceptible to environmental factors such as temperature, pressure, and humidity,

which might alter the precision of the findings [78].

Another technique that uses time-domain measurement for the analysis Terahertz Time-Domain Spectroscopy (THz-TDS). This is a measuring method that probes the characteristics of materials using ultrafast pulses of terahertz radiation. THz radiation is a kind of electromagnetic radiation that has a frequency between microwaves and infrared light. THz-TDS works by producing brief pulses of THz radiation and directing them towards a sample. The transmitted or reflected THz radiation is then measured, and the latency between the transmitted and detected waves is utilized to calculate the sample's spectral features [79].

THz-TDS is a newly biosensing technique. It is a sophisticated imaging and spectroscopic technology used to investigate biological and chemical materials in the infrared spectrum's lower frequency range. THz-TDS is used in biosensing to investigate the molecular structure and function of biological materials such as proteins [80], DNA [81], and cells [82]. It has the ability to reveal information on the molecular structure and function of materials while inflicting no harm, making it a significant tool for drug development, illness diagnostics, and tissue engineering. THz-TDS may be used to identify changes in the molecular structure of a sample caused by illness [83], as well as to evaluate therapy efficiency [84].

THz-TDS provides a number of benefits in biosensing, including non-invasiveness, great sensitivity to molecule vibrations [85], and compatibility with a variety of sample types. THz-TDS may also offer information on the chemical composition and structure of biological materials, which is important for many biosensing applications [80, 81].

THz-TDS, on the other hand, has certain restrictions. One of the key disadvantages is the lack of THz sources and detectors, which might make THz-TDS impractical in certain situations [86]. Furthermore, THz-TDS is partially slow in comparison to other imaging methods, which limits its application in certain scenarios [87]. Despite these limitations, THz-TDS is an essential biosensing technology that has the potential to deliver new insights into the molecular structure and behavior of biological systems.

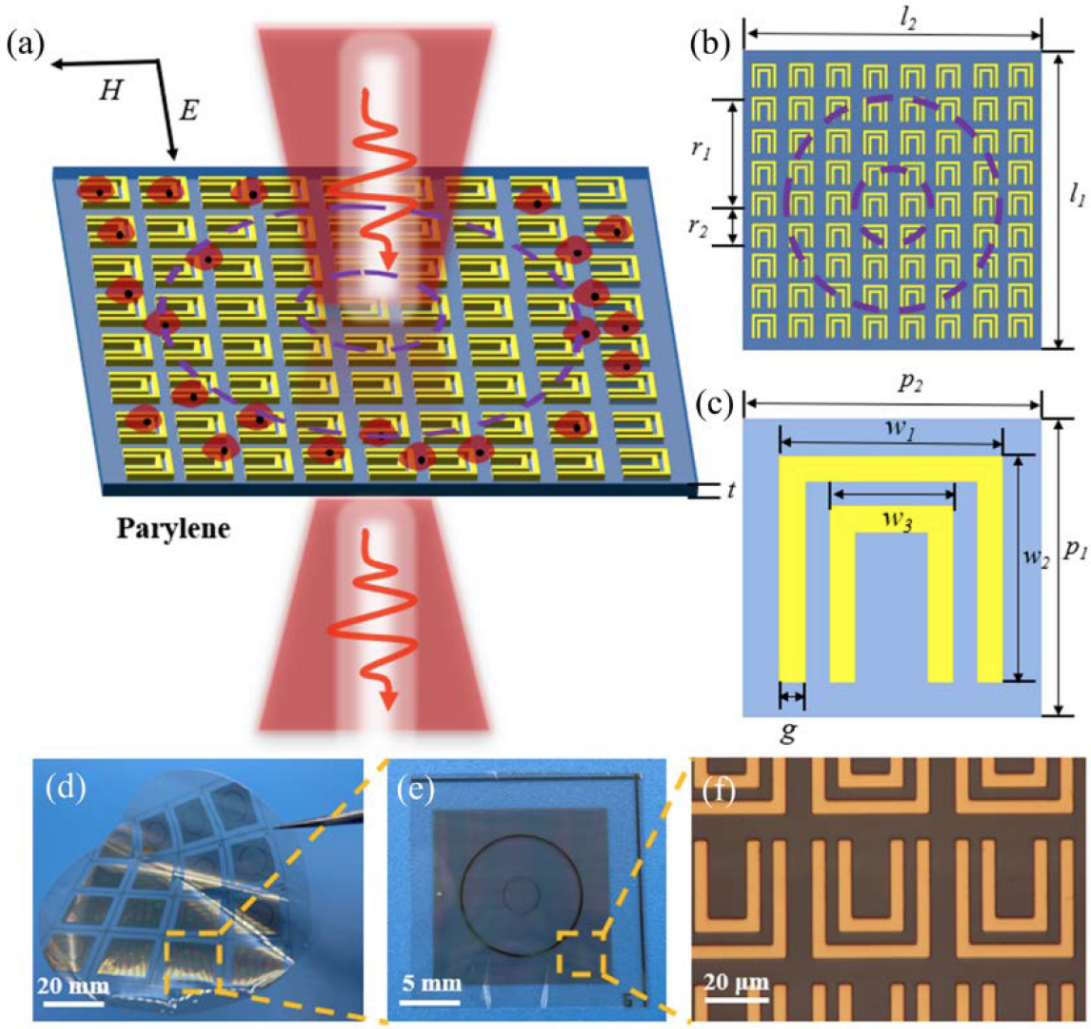

Figure 1.6: (a) Metamaterial biosensor schematic illustration: THz beams routinely incident via the biosensor on which the MDA MB 231 cell was cultivated; (b) the metamaterial biosensor construction. The geometrical parameters are as follows: l1 = l2 = 20 mm, r1 = 5 mm, r2 = 1.5 mm, and t = 15 m; (c) a double U-shaped metamaterial structure. The geometrical parameters are as follows: p1 = p2 = 44 m, w1 = w2 = 36 m, w3 = 2 = 0 m, and g = 4 m; (d) physical picture of 4-inch biosensor; (e) physical photograph of 20 20 mm biosensor; and (f) micrograph of the metamaterial, reprinted from [88].

1.3 State of art in compact Raman systems

Compact Raman systems are downsized versions of classic Raman spectroscopy systems that formerly needed large size and sophisticated instrumentation. The development of compact, portable, and low-cost Raman spectroscopy instruments that use cutting-edge technologies, such as micro-electromechanical systems (MEMS) and miniaturized lasers, to achieve improved performance and efficiency in Raman analysis is the state-of-the-art in compact Raman systems. These technologies have diversified the possible uses of Raman spectroscopy, making it available to a broader variety of users. Here are presented many different designs of compact Raman systems.

1.3.1 Smartphone/Handheld Raman System

A Raman smartphone or handheld system is a device that utilizes Raman spectroscopy technology to analyze and identify materials. It is a real smartphone with a user-friendly user interface on which a removable module for Raman signal acquisition is integrated. This technology works by shining a laser on a sample and measuring the scattered light to determine the chemical composition of the sample. These handheld systems are typically small and portable. For instance, the size of a commercial handheld system is 27 x 15.6 x 6.2 cm^3, with a weight that ranges between 420g to 1500g [89].

As shown in tab.1.1, several works in the literature up to now report the implementation of the Raman smartphone system in the area of *Point-Of-Care Testing (POCT)* [90][91], identification of chemical compounds [92], trace detection of pesticide residues [93], mixture analysis [94] and also recently a pathological diagnosis of liver carcinoma [95].

Weighing about 420 g, these portable handheld Raman spectrometer devices offer good portability and are supplied with a 785 nm laser source. The optical power ranges between 200-450 mW [90] and they adopt large numerical aperture lenses to achieve an appropriate spatial resolution of about 10 cm^{-1} [91]. Despite the miniaturization of the smartphone Raman system, it is known that the sensitivity of the Raman signal decreases. To overcome this issue, high-performing Surface Enhanced Raman Scattering (SERS) substrates can be implemented for signal enhancement of targeted solutes, which offer a feasible solution for SERS-based point-of-care testing (POCT) applications [91]. Typically SERS substrates are obtained using silver nanoparticles (AgNPs) on a filter paper substrate [91] or gold nanoparticles (AuNPs) on a silicon wafer substrate [93]. The average measurement time ranges between a few seconds [94] to 15 s [91], depending on the application. A linear array CCD is typically used as the detector in all configurations, resulting in a

system with high performance and excellent portability, with an overall device cost of around $10,000 [92][93]. Liping Huang [95] reports the characteristics of a typical objective for this application, which is 50X of magnification with NA=0.50 and WD = 8.2 mm. These systems may propose the use of a cloud-based architecture that leverages a wireless standard for data communication, and with the advancement of deep learning techniques, it is now possible to use these techniques on the cloud to interpret the data acquired by the system [92][94].

Drawbacks

One of the major drawbacks of smartphone/handheld Raman systems is their sensitivity. Due to the miniaturization of these devices, the sensitivity of the Raman signal is often reduced, making it more difficult to detect low concentrations of target analytes. This can be mitigated through the use of high-performing SERS substrates, such as those made from silver or gold nanoparticles, but this also increases the cost and complexity of the system. The use of silver nanoparticles (AgNPs) in SERS substrate generates oxidation problems, which could result in a reduction in biosensing efficiency. However, gold nanoparticles (AuNPs) are not used because of their high cost, while copper has still oxidation and stability problems.

Another drawback is the cost of these systems. Many smartphone/handheld Raman systems are still relatively expensive, with an overall device cost of around $10,000. This can make them less accessible for certain applications or users. In addition, the cost of the SERS substrates and the ongoing maintenance and replacement of these substrates can also add to the overall cost of the system.

Furthermore, no article on the subject justifies the use of an additional CCD detector other than the one already mounted on the smartphone for the camera.

The accuracy of these systems can also be a concern. Factors such as the stability of the laser source, the quality of the optics and the detector, and the expertise of the user can all affect the accuracy of the measurements.

In addition, the use of deep learning algorithms for data interpretation can also introduce errors if the algorithms are not properly trained or validated. It is also interesting to point out how the output data are interpreted. Indeed, the use of Deep Learning techniques makes it possible to process features extracted from Raman spectra and perform qualitative/quantitative analysis using Convolutional Neural Networks (CNNs). Since the measure of concentration is not directly evaluated from the amplitude and shift of the peaks, the spectra do not necessarily have to reflect a realistic shape, but simply match the shape of those used to train

the network. In fact, the spectra that are obtained are usually far different from those

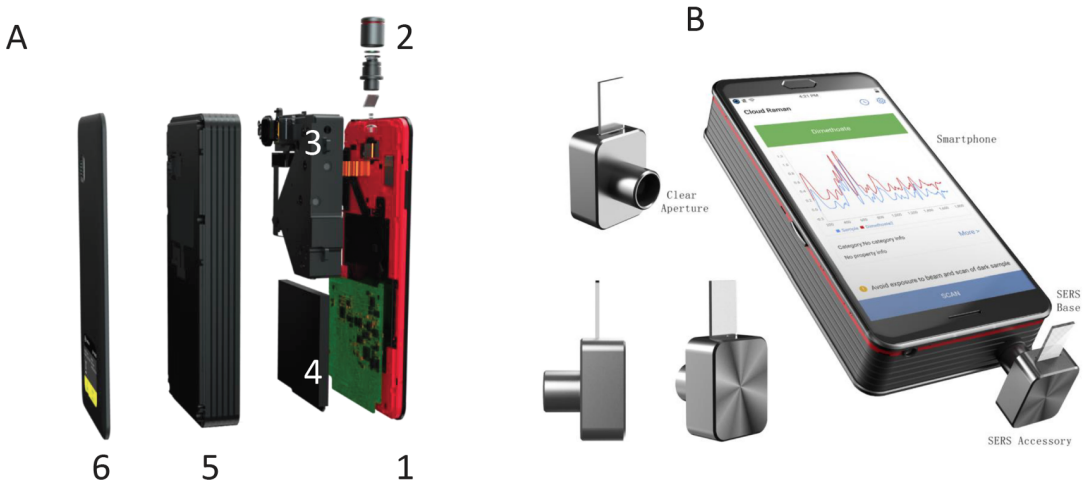

Figure 1.7: (A) detailed illustration of XITM showing the components of the A1 smartphone by CloudMinds, including the laser output, Raman optical module, electronic control board, and casing. Additionally, (B) a diagram is provided to demonstrate how SERS measurement is performed using the clever SERS terminal, adapter, and SERS chips., after ref. [94, 93].

Perspective

The use of smartphone/handheld Raman systems for SERS-based applications presents a surplus of opportunities for advancements in various fields. The compact and user-friendly design of these systems makes them highly suitable for portable and on-site analysis in a variety of settings, such as monitoring environmental pollutants, detecting contaminants in food and water, and performing biochemical sensing for medical diagnostics.

One area in which smartphone/handheld Raman systems have shown great potential is in the field of point-of-care testing (POCT). These systems can provide rapid, accurate results with minimal sample preparation, making them ideal for use in remote or resource-limited settings. Additionally, the use of cloud-based architectures and deep learning techniques can further enhance the capabilities of these systems, allowing for real-time data analysis and interpretation.

Another area of potential growth for smartphone/handheld Raman systems is in the field of biosensing. These systems can be used to detect a wide range of biomolecules with high sensitivity and specificity. The use of SERS substrates made from gold or silver nanoparticles can further enhance the sensitivity of these

systems, making them suitable for detecting low concentrations of target analytes.

In addition, there is a growing interest in using smartphone/handheld Raman systems for the real-time monitoring of environmental pollutants and contaminants in food and water. These systems can provide rapid and accurate results, allowing for immediate action to be taken in the event of contamination.

Despite these opportunities, there are still some limitations that need to be addressed before these systems can be widely adopted. These include increasing the sensitivity and specificity of the systems, reducing the cost and complexity of the devices, and improving the accuracy of the measurements. Despite these challenges, the compact footprint, ease of use and the potential applications make these systems a promising technology for the future. Future efforts would be directed towards the creation of functional SERS devices capable of individualising actual solutes with better sensitivity and selectivity.

1.3.2 Portable Raman System

A Portable Raman System is a device that uses the Raman effect to analyze the chemical composition of a sample. It typically consists of a laser, a spectrograph, and a detector, and is designed to be portable and easy to use. The main feature that distinguishes a portable device from a handheld one is the absence of a battery self-contained in the device, and so the necessity to be plug powered. This category is characterized by a limited weight and size.

Of all the miniaturized Raman spectroscopy devices on the market, portable devices are certainly among the most popular [96]. Applications range from forensic and homeland security investigation [97], examination historic powders [98], pharmaceutical and medical diagnostic [99], glucose detection [100], explosive detection [101] and minerals on outcrops detection [102], as summarized in tab.1.1.

Specifically, the most typical Raman portable configuration comprises a narrow band laser, a spectrometer containing a CCD linear image sensor, and an electronic control unit that communicates with the subject via keyboard and display, manages the measurement procedure, and runs the classification algorithm. The signal is transmitted to and from the sample via fibre optic connections.

The majority of portable devices currently on the market have a small display that is mainly used to choose testing settings, give results obtained, and make a preliminary identification [15].

A technical comparison of different portable Raman systems can provide valuable insights into the performance, features and limitations of these devices. The limit of detection (LoD) is an important parameter to consider when evaluating the sensitivity of a Raman system, as it represents the minimum concentration of a

chemical species that can be detected. For example, Jeon Woong Kang et al. [11] reported a LoD of 75 mg/dl based on standard deviation and 29-78 mg/dl based on the correlation coefficient. The wavelength (nm) and resolution (cm^{-1}) of the system are other important parameters, as they affect the accuracy and precision of the measurement. Typical values are between 532 - 830 nm and 12-28 cm^{-1} [103] [104] [32].

The laser power (mW) and detector used in the system also play a crucial role in its performance. Laser power, typically between 70 mW [103] and 250 mW [11] determines the intensity of the light used to thrill the target, which affects the signal-to-noise ratio and the measurement sensitivity, while the detector, usually a CCD, is responsible for capturing the Raman scattered light and converting it into an electrical signal.

The illumination collection geometry is another factor that can affect the performance of a Raman system, as it determines the direction of the light used to excite the sample and can affect the performance and accuracy of the measurement. There are several different illumination collection geometries that have been used in portable Raman systems, including oblique angle (off-axis 60°) non-contact vertical illumination collection geometry, which is useful for measuring Raman peaks in vivo without contact with the sample [11]. Backscattering configuration is useful for analyzing thin films and surfaces [105]. SORS, Resolve's zero offset collection and Epi-illuminated RMX are useful for measuring Raman spectra of samples with high fluorescence background or samples with low Raman scattering [32]. Each approach has benefits and drawbacks, and the optimal method to utilize will be determined by the application and material being evaluated.

When comparing different portable Raman systems, it is also important to consider the dimension of the system, as it can affect its accessibility and ease of use in certain environments. Portable Raman systems can come in a multiplicity of sizes, due to the specific instrument and its intended use case. A typical portable Raman system can range in size from a small handheld device to a larger benchtop instrument.

Drawbacks

Portable Raman systems are a helpful tool for chemical analysis in a variety of fields, but they also have some limitations and drawbacks. One of the main restrictions of portable Raman systems is their sensitivity, which is generally lower than benchtop Raman systems. This can make it more difficult to detect and analyze low-concentration samples, especially in noisy environments.

Another limitation of portable Raman systems is their resolution, which is often lower than that of benchtop systems. This can make it more difficult to distinguish

closely spaced peaks and to accurately identify the chemical compounds present in a sample.

Portable Raman systems can also be affected by vibrations and movement, which can cause problems with data quality and accuracy. This can be especially challenging in field settings, where the system may be subject to a wide range of environmental circumstances.

The size and weight of portable Raman systems can also be a drawback, as they may not be as easily transported and used in some environments as larger, benchtop systems. Furthermore, the cost of portable Raman systems can be a limiting factor for some applications.

Finally, Portable Raman systems are also dependent on the illumination collection geometry and laser wavelength, which can affect the performance and accuracy of the measurement. Therefore, it's important to choose the right illumination collection geometry and laser wavelength that fits the sample and the application.

The two primary difficulties that limit an extensive use of portable Raman spectroscopy systems are the expensive cost of such instruments and the absence of accurate automated detection capabilities of analytes of interest. Other significant issues with the design of Raman portable spectrometers stem from the weak usable Raman signal and the presence of effective optical interference covering the signal of interest, such as environmental lightning and fluorescence caused by the laser source.

Perspective

The field of portable Raman spectroscopy is continually progressing, with new advancements and developments being made in both the hardware and software of these systems. Efforts to decrease the size and cost of portable Raman devices are ongoing, making them more accessible and affordable for a wider range of applications.

Research is also being conducted to improve the sensitivity and resolution of these systems. Additionally, new detection technologies such as superconducting nanowire detectors are emerging which can provide high-performance detection capabilities for portable Raman systems.

The use of advanced data analysis techniques and machine learning algorithms are also being explored to improve the accuracy and precision of portable Raman systems. Additionally, the increasing demand for real-time, in-situ and on-site analysis are driving the expansion of portable Raman systems for various applications such as food safety, environmental monitoring, and industrial quality contr

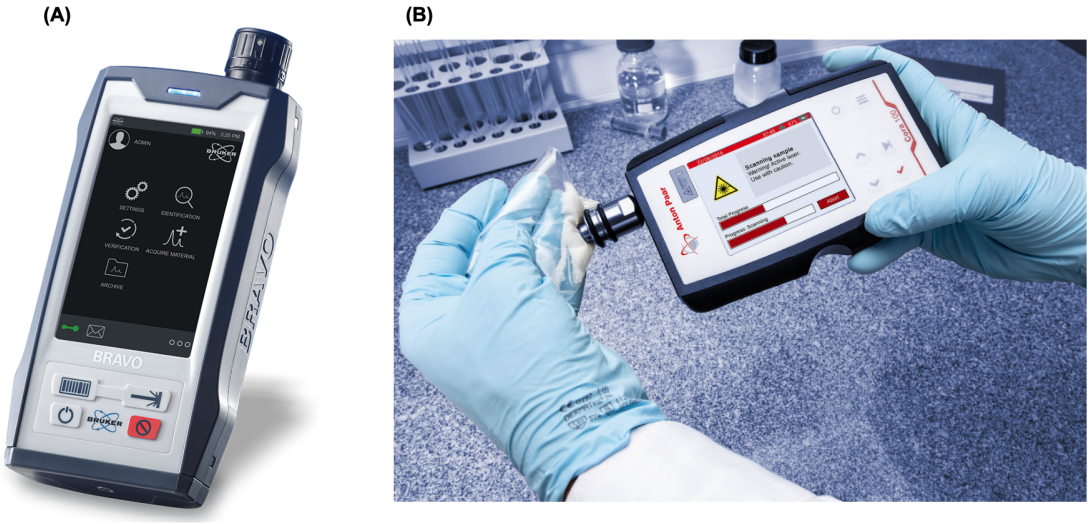

Figure 1.8: Example of portable Raman system (A) BRAVO system [89] and (B) portable Raman-Spectrometer Cora 100 [106].

The use of advanced data analysis techniques and machine learning algorithms are also being explored to improve the accuracy and precision of portable Raman systems. Additionally, the increasing demand for real-time, in-situ and on-site analysis are driving the expansion of portable Raman systems for various applications such as food safety, environmental monitoring, and industrial quality control.

The performance of portable Raman spectrometers currently on sale has to be improved, particularly the accuracy of automated analytes identification. A second laser and spectrometer could be added, the information processing hardware could be improved, and novel techniques for data collecting and interpretation could be used. Because increasing the resolution would necessitate not only replacing the CCD detector with one with more pixels but also increasing the size and weight of the spectrometer, another goal should be to find a good compromise between data processing algorithm requirements and weight and size constraints.

Overall, the field of portable Raman spectroscopy is a rapidly advancing one, with ongoing efforts to improve the performance, accessibility, and affordability of these systems.

1.3.3 Wearable Raman System

A wearable Raman system is a state-of-the-art device that merges the capabilities of Raman spectroscopy and the ease of use of a wearable and mobile system. The system typically consists of two main components: a SERS (Surface-enhanced

Raman spectroscopy) substrate and an external portable spectrometer. The SERS substrate, which can be either rigid or flexible, is designed to be attached to the skin, typically on a patch shape, or even mounted on a glove, and it is used to collect sweat, blood or other bodily fluids. The external portable spectrometer is connected to the SERS substrate through an optical fibre, and it is used to analyze the chemical composition of the obtained sample. This technology enables real-time and non-intrusive tracking of various chemical compounds present in the body, such as glucose, lactate, and other markers, as well as the identification of specific chemicals or contaminants in the surrounding environment.

Recently, many wearable Raman devices have been developed with a focus on drug detection [107], non-invasive glucose detection[108, 109, 110], pH sensing [111], pesticide residues detection in fruits [109, 112]. All this information are gathered in tab.1.1.

The description in literature of these devices usually focuses more on the wide variety of techniques and materials used to produce the substrate. However, the technical specifications of the portable spectrometer are not always the primary focus of these descriptions. The wavelength of light used in these devices generally falls between 633 nm and 785 nm, and the power ranges from a few milliwatts to 100 milliwatts, depending on the intended application. SERS substrates often utilize gold or silver nanoparticles, which can be produced in various shapes such as spheres, rods, and nanowires, and through different techniques such as paper membranes and electrospinning. Some devices incorporate flexible support materials like silk fibroin and thermoplastic polyurethane, while others use microfluidic systems to enhance selectivity and sensitivity. A 50X magnification objective is commonly used.

Drawbacks

It is clear that wearable Raman systems have the ability to advance the field of chemical analysis by providing real-time and non-intrusive monitoring of various chemical compounds. However, despite the potential benefits, there are also several drawbacks to this technology.

One major drawback is the cost and complexity of the equipment required for the analysis. The external portable spectrometer and SERS substrate can be expensive and require specialized training to operate, making it difficult for some institutions and organizations to afford and implement [113]. Additionally, the sensitivity and accuracy of the analysis may be limited by the quality of the SERS substrate and the sample collection process may not be entirely non-invasive.

Another drawback is that Raman spectroscopy is an inherently weak signal, which makes it challenging to detect very low concentrations of certain compounds, also

it may generate interference with other sources of light, such as sunlight, indoor light and other sources of Raman active light [114]. Furthermore, the integration of the system with smartphones and cloud networks may raise privacy and security concerns, as the data needs to be transmitted and stored.

Another significant drawback is the wearability of the device. The sensor is the only part that is worn, while the spectrometer is external and entails all the limitations of a non-wearable technology. Furthermore, when working with flexible substrates, some problems may arise from a mechanical point of view, such as suitability and conformity, as the majority of flexible substrates cannot simultaneously be ultra-thin and light-transmitting. Therefore, it is important to take into account all the potential.

Some other problems may arise from a mechanical point of view when working with flexible substrates in terms of suitability and conformity: the majority of flexible substrates cannot simultaneously be ultra-thin and light-transmitting.

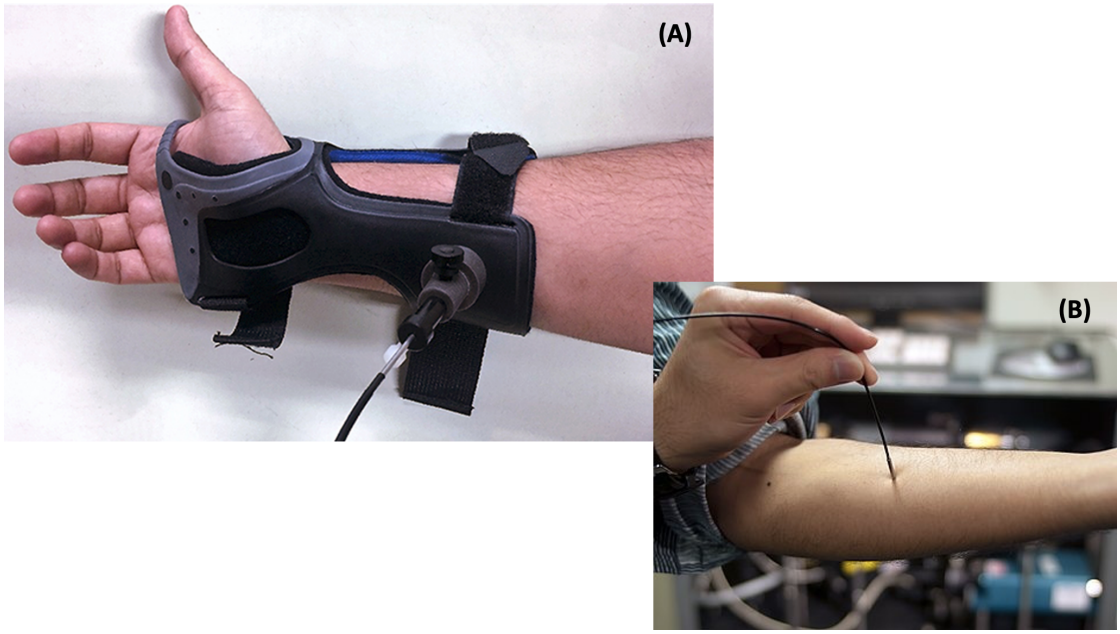

Figure 1.9: Two example of wearable Raman system from (A) the University of Missouri [115], and (B) from MIT research group [116].

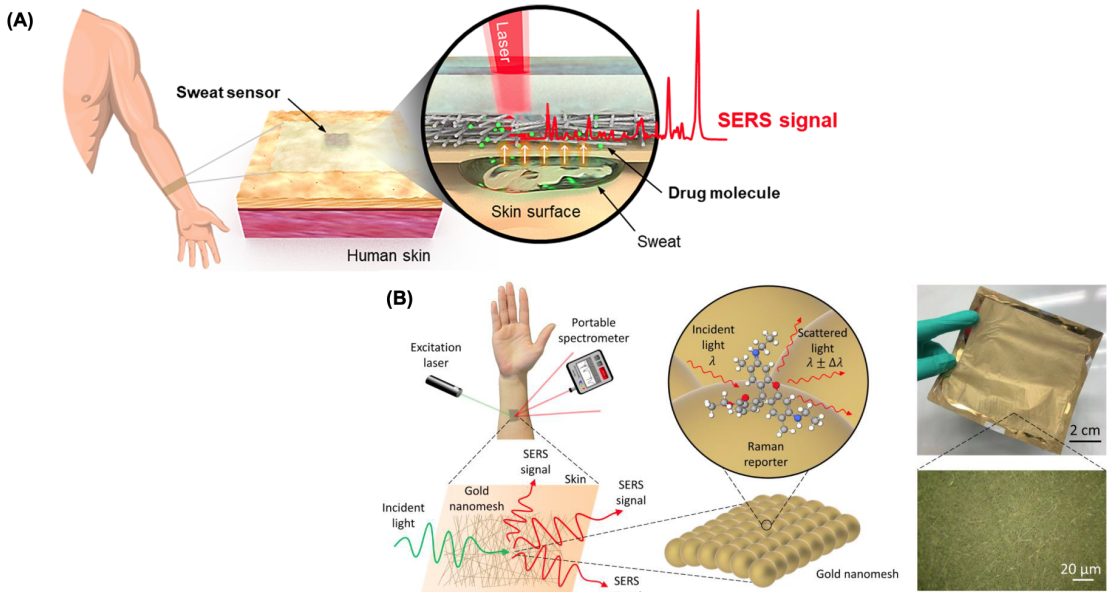

Figure 1.10: (A) A diagram is provided to show the design of a wearable SERS patch sensor that is capable of label-free detecting drug molecules in sweat. [107], and (B) illustration of using this highly scalable and wearable technology for surface-enhanced Raman spectroscopy. [117].

Perspective

Wearable Raman systems have the potential to revolutionize the field of chemical analysis by providing real-time and non-invasive monitoring of various chemical compounds. This technology has the potential to revolutionize healthcare by enabling continuous monitoring of biomarkers such as blood glucose levels and environmental monitoring by detecting pollutants and other chemicals. Additionally, the integration of smartphones and cloud networks with wearable Raman systems allows for convenient data collection and analysis, making it more accessible to a wide range of users.

However, the technology is still in its early stages of development, and ongoing research and development are required to address limitations such as high costs, limitations in sensitivity and accuracy of analysis, and privacy concerns. With advancements in materials and miniaturization, it is likely that the cost of equipment will decrease and the technology will become more portable and user-friendly, making it more accessible for a wider range of applications.

In particular, the area of personalized medicine poses challenges for wearable Raman sensors in terms of reducing interference and increasing selectivity when working with complex body fluids such as sweat. One potential solution is to

combine the SERS substrate with a microfluidic chip, directing various solutes to various functional regions for synchronous isolation and multi-component detection. Another option is to include a filtering system in the sensor through a semi-permeable porous membrane, which would increase selectivity and sensitivity by dividing components according to size, addressing one of the current limitations of the technology.

1.3.4 Home-made Raman system

A Raman system that is constructed and assembled within a laboratory or facility, as opposed to being purchased from a commercial source, is referred to as an in-house or "insourcing" system. These systems are created using internal resources and personnel to address needs that cannot be met by commercially available options. They may include components such as a laser source, spectrometer, sample stage, and various optics and filters, and can be constructed using techniques like custom-built mechanical parts and 3D printing. These systems offer the advantage of being able to be customized to specific needs and modified as necessary but may require more time and resources to build and maintain. Recently, the use of in-house built Raman systems has been increasing due to the availability of open-source software, hardware, and 3D printing technology, which makes it easier for researchers to create their own optimized systems. Furthermore, many researchers prefer in-house built systems as they can be tailored for specific applications, which is not possible with commercially available options.

References on in-house built Raman devices can be found in the literature on testing finished pharmaceutical products [118], quantification of melamine in infant formula [119] and graduate education/research [103, 120].

It's essential to bear in mind that the technical features of a Raman system may differ based on its intended use. For example, the laser wavelength used can range from 532 nm to 852 nm, and the power can vary from 70 mW for analyzing chemical mixtures [103] to 300 mW for drug testing [118]. Furthermore, the system's spectral resolution power is influenced by the technical characteristics of the optical components employed and can range from 6-8 cm^{-1} to 20-28 cm^{-1}. The usual measurement time for these systems ranges between 6 s [119] to 30 s [118], and it is most common to use a CCD sensor such as the Sony ILX511 linear silicon CCD detector [103]. For more detailed information, look at tab.1.1.

The expense of these devices is primarily impacted by the necessary training for employees and the equipment available within the company. The minimum cost for these systems is $3800.

three It's worth noting that none of the applications outlined has mentioned using

Surface Enhanced Raman Spectroscopy (SERS) to enhance the signal. SERS is a technique used to enhance the sensitivity and specificity of Raman spectroscopy by utilizing a substrate with a high surface area and a high degree of surface roughness, which can significantly amplify the Raman signal. It's worth considering as an option as it can provide a significant enhancement in the signal-to-noise ratio, which can be useful in certain applications.

Drawbacks

The decision to make a device with only available resources often prevents the development of effectively tradable devices by limiting their use to research or educational levels. In-house built Raman systems offer many advantages such as

the capability to tailor the system to specific needs and the ability to modify it as needed. However, there are also certain drawbacks to take into account.

One of the main drawbacks is that building and maintaining an in-house built Raman system can be a time-consuming and resource-intensive process, as some sources emphasize [103][119]. Additionally, in-house built systems may not be as reliable or accurate as commercially available systems, which have been extensively tested and validated, resulting in a lack of precision and accuracy.

The lack of expertise in building and maintaining an in-house built Raman system, as well as the cost of the system, which can vary widely, can also be a challenge. Furthermore, in-house built Raman systems may not be as portable as commercially available systems, limiting their use in certain applications.

It's important to keep in mind that when a device is created using only the resources that are currently available, it often prevents it from being developed into a device that can be effectively traded and its usage is limited to research or educational purposes.

When testing pharmaceutical products, attention must be paid to active pharmaceutical ingredients (API) that could lead to a high number of false positives, in the case of an overwhelming Raman signal, and false negatives, when a non-usable Raman signal is produced. And further problems may arise in the analysis of APIs that generate a very intense Raman signal that may mask the signal of weaker APIs.

Perspective

Assembling a Raman spectroscopy system in-house has gained popularity in recent years as a cost-efficient alternative to commercially available options. These systems can be tailored to specific needs and provide greater control and customization over the instrumentation. By building their own systems, researchers have the

opportunity to gain a deeper understanding of the principles of Raman spectroscopy and the design and construction of the instrumentation. This can serve as an educational tool for students and researchers.

Furthermore, it has been demonstrated that in-house built Raman spectroscopy systems can be effectively used in various applications such as medicine, food industry and counterfeit detection. With the advancements in technology and access to low-cost components, building one's own Raman spectroscopy system has become more feasible.

It is interesting to analyze the next steps in in-house-built Raman device research will be. In academia, the aim will be to fully understand the potential of Raman spectroscopy, For this, an appropriate high-pass filter could be chosen, and the laser source could be changed to assess any reduction in fluorescence. The aim would also be to reduce the noise caused by different components in the device by adding a notch filter.

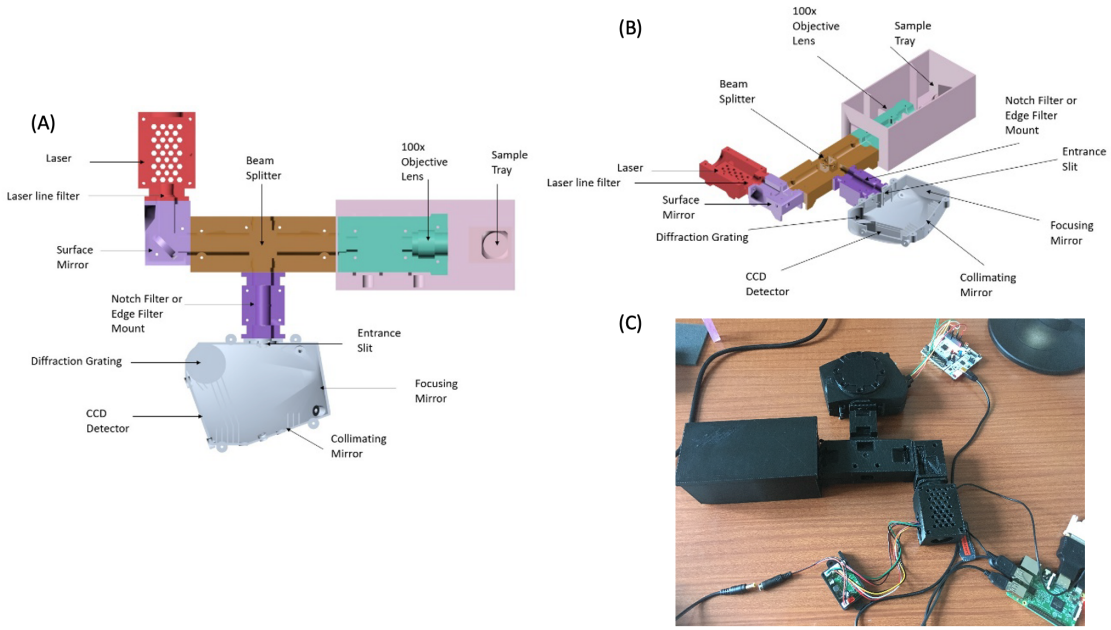

Figure 1.11: (A) An illustration of the top view of the in-house built Raman spectrometer system, (B) a labeled and assembled version of the system, and (C) a fully assembled 3D printed Raman spectrometer., reprinted from [120].

SMARTPHONE/HANDHELD SYSTEM													
Number	**Author**	**Devices**	**Weight (g)**	**Wavelength (nm)**	**Laser power (mW)**	**Spectral resolution (cm^{-1})**	**SERS (Surface enhanced Raman scattering)**	**Averaged measurement time (s)**	**Detector**	**Objective**	**Sample**	**Goal**	**Notes**
1	*Fanyu Zeng et al. (2019)*	Smartphone portable Raman spectrometer	420	785	450	8-11	Filter paper + Silver nanoparticles (AgNPs)	15	Linear array CCD (Hamamatsu S11510)	VPH gratings (Bulk phase holographic) + Large numerical aperture lenses FWZ.0 [F#/(fD)] + Direct spatial coupling tecnology	Rhodamine 6G (RDM 6G) Crystal violet	POCT (point-on-care test device)	***Negative:*** They didn't used phone's CCD Cost ($10.000) Should'nt they use gold at 785 nm? (Silver 390 nm) ***Positive:*** Cloud based data platform CNN system for automatic detection New optic design Improved SNR Improved portability
2	*Lynn Chandler et al. (2019)*						NO	<1			Paracetamol TiO2 powder Acetone	Mixture analysis	
3	*Taotao Mu et al. (2018)*				200		Silicon wafer + Gold nanoparticles (AuNPs)	10			Pesticides	Detection of pesticide residues	
4	*Taotao Mu et al. (2018)*				300	9-11	NO	<2			Ethanol Acetone Acetone (62%) + Ethanol (38%)	Material identification	
5	*Fanyu Zeng et al. (2018)*						Filter paper + Silver nanoparticles (AgNPs)				Rhodamine 6G (RDM 6G) Crystal violet	POCT (point-on-care test device)	
PORTABLE SYSTEM													
6	*Emad L. Izake et al. (2010)*	Portable Raman spectrometer	-	-	-	-	-	-	-	-	-	Forensic and homeland security investigation	**NO DEVICE** Good theoretical description about Portable Raman Spectroscopy and different Raman tecniques
7	*Silvia Innocenti et al. (2022)*	Portable Sequentially Shifted Excitation Raman Spectroscopy (BRAVO)	-	785 - 852	40-100	10-12	NO	<1	Termoelectrically cooled 400-1060 nm	50x long-working-distance	Pigments mainly enclosed in glass vials	Examine Historic Powders Enclosed in Glass Vials	***Negative:*** No description of Raman System ***Positive:*** Lenses & CCD description
8	*Keith Carron et al. (2010)*	Perspective on Portable Raman Spectroscopy	-	785	-	8-12	NO	-	-	-	-	Pharmaceutical and medical diagnostic	***NO DEVICE***
9	*Yi Zheng et al. (2017)*	Wearable Raman spectroscopy system	-	785 *(B&Wtek, BRM-OEM-785-0.3-100-0.22-FC)*	300	6	NO	20	Back-illuminated linear array CCD *(Hamamatsu Photonics, S11156-2048-01)*	Thallium-doped grin lens	Glucose solution (4.4-11.1 mmol/L)	Noninvasive blood glucose detection	***Negative:*** - ***Positive:*** Thallium-doped lens and a specially designed optical probes for better stability In *vitro* and in vivo experiments Low cost Good wearability
10	*David S. Moore (2008)*	Portable Raman system (REVIEW)	-	532 (YAG laser) 785 830	300	3.250 (785 nm) 2.5 (830 nm)	NO	10-20	CCD camera (Andor DU420)	-	Trinitrotoluene (TNT) Octahydro-1,3,5,7-tetranitro-1,3,5,7-tetrazocine (HMX)	Explosive detection	Good explanation of Raman physics
11	*J. Jehlicka (2009)*	Portable Raman for geological application	1800 1900 -	785 785 785	300 120 -	7-10 6-9 3-8	NO	10	Peltier-cooled CCD		Several minerals	Minerals on outcrops detection	-

12	*M. Gnyba (2011)*	Portable Raman spectrometer design	-	785	Few hundreds milliwatts	6	NO	-	CCD with resolution 1024 pixels	-	-	-	Design of a typical portable Raman spectrometer Ottimo per sviluppi future/modifiche
WEARABLE RAMAN DEVICES													
13	*Eun Hye Koh et al. (2021)*	Wearable SERS sensor	-	633	6	-	YES	0.5	-	-	2-fluoro-Methamphetamine (2-FMA)	Drug detection	
14	*Dan Wang (2022)*	Wearable 3D particle-in-cavity SF-AAO-Au SERS sensor	-	633	1.5	-	Flexible SF-AAO-Au	1	-	50x	Fructose, galattose, sucrose, and glucose 10 μL of thiram solution	Noninvasive glucose detection Lab-on-glove practical application for pesticide residues detection in fruits	Flexible SERS sensor for good adeherence Silk fibroin (SF) as flexible support
15	*Eun Hye Koh (2021)*	Wearable SERS sensor for Label-free molecular detection	-	-	-	-	SF-AgNWs layer	-	-	-	Methylene blue (MB) 2-fluoro-methamphetamine (2-FMA)	Drug detection tests	Silk fibroin (SF) as flexible support
16	*Michael Chung (2021)*	Wearable flexible sweat pH Sensor Based on SERS	-	-	-	-	Electrospun thermopiastic polyurethane (TPU) NFs, coated with Au	-	-	-	Sweat	pH sensing	Electrospinning for SERS
17	*Xue-Jian LI (2022)*	Wearable screen-printed SERS array fiber gloves	-	785	10	5	AgNPs	5	-	-	3 μL of 10-5 M Rhodamine 6G solution Polycyclic aromatic hydrocarbons	On-site environmental emergency monitoring	No wearable
18	*Hilal Torul (2015)*	Paper based microfluidic SERS platform	-	785	140	-	Au nanorods	20	-	-	Glucose solution (0,5 – 10 mM)	Glucose measurement	Microfluidic system for blood spitting Stability + sensitivity + selectivity
IN-HOUSE BUILD RAMAN DEVICES													
19	*Mustapha Hajlou (2013)*	Handheld in-house build Raman devices	-	785	300	6-8	NO	30	-	-	Commonly used analgesic, antimalarial, and antidiarrheal medicines.	Testing finished pharmaceutical products	-
20	*Anel Beganovic et al. (2020)*	Bruker BRAVO handheld Raman spectrometer	-	785 - 852	100	10-12	NO	6	CCD	-	First infant milk powder intentionally adulterated with various amount of solid melamine	Quantification of melamine in infant formula	
21	*Neethu Emmanuel (2021)*	Integrated portable Raman spectrometer	-	532	70	20-28	NO	-	Sony ILX511 linear silicon CCD detector	NO	Chemical mixture analysis	Graduate education/ Research	**GOOD PAPER FOR OPTIC DETAIL AND WRITING THESIS**
OTHERS													
Number	**Author**	**Subject**	**Raman peak (cm^{-1})**	**Best average linear fitting R**	**Limit of Detection (LoD)**	**Wavelength (nm)**	**Resolution (cm^{-1})**	**Laser power (mW)**	**Detector**	**Illumination collection geometry**	**Instrument**	**Goal**	**Notes**
22	*Jeon Woong Kang et al. (2020)*	Pigs	911 1060 1125	0.94	Based on standard deviation ~75 mg/dl Based on correlation coefficient 29-78 mg/dl	830	-	250	-	Oblique angle (off-axis 60°) Non-contact vertical	Portable Raman spectrometer	Demonstrate that Raman peaks can be measured in vivo	-

23	*Rishikesh Pandey et al. (2022)*	Uman	-	-	-	830	-	-	CCD	Backscattering configuration	Portable Raman spectrometer	Discuss the recent activity in terms of instrumentation development and innovative framework algorithmic frameworks	-
24	*Phillip Wilcox et al. (2018)*	Chemical samples: *Thiodiglycol* (TDG) and dimethyl *methylphosphonate* (DMMP) et al.	1065 1130 1297 1440	-	-	785 830	-	-	CCD	SORS Resolve's zero offset collection Epi-Illuminated RMX	Two Portable Raman spectrometer	Compare spectral resolution between two different configurations of commercial instrument	-
25	*Neethu Emmanuel (2021)*	-	540-645	-	-	532	20-28	70	-	--	-	-	**GOOD PAPER FOR OPTIC DETAIL AND WRITING THESIS**
26	*Edgar Guevara et al. (2022)*	Humans	1575 - 1220	-	-	785	12	90	CCD	-	Portable Raman system (PeakSeeker, Agiltron Inc.)	Investigated feasibility of using Raman spectroscopy to noninvasively screen for prediabetes and diabetes in vivo	Exposure time 15s
27	*Ivan A.Bratchenko et al. (2022)*	-	-	-	-	-	-	-	-	-	-	-	Comments the previous paper (nr. 26)
28	*Edgar Guevara et al. (2022)*	-	-	-	-	-	-	-	-	-	-	-	Comments the previous paper (nr. 27)
29	*Ramon A. Alvarez-Puebla (2022)*	Different substrates	-	-		Several						Summarizing the experimental complexities related to the interaction of light with the sample in SERS	Good information about SERS Relationship between N.A. and resolution

Table 1.1: This table provides a comprehensive overview of the key information gathered during our literature review on wearable Raman systems. It allows for easy comparison of the different strategies developed by various research groups across a range of applications, providing a valuable resource for understanding the current state of the field and identifying potential areas for further exploration.

Chapter 2

Design and characterization of Raman laser driver

Nowadays, the proportional-integral-derivative (PID) control system is usually regarded as the most extensively employed control strategy. Approximately 90% of control systems use PID control, with the derivative term often set to zero (PI control) [121]. A PID control system's objective in Raman laser driver is to automatically modify the laser temperature in real-time to maintain a consistent temperature regardless of changes in the operating conditions [122].

The PID control algorithm compares the intended temperature setpoint with the observed temperature in real-time and then uses the error signal to change the laser's heating element. A PID controller's three components meet the conventional criteria for most control issues.

The integral term removes steady-state error while monitoring a constant setpoint and aids in rejecting constant disturbances, but it responds slowly to current error [123].

The proportional term, on the other hand, reacts fast to the present mistake, but it needs a large gain to attain setpoint precision [123].

The derivative term forecasts future mistakes and aids in the reduction of transitory errors, but it also amplifies high-frequency sensor noise [123].

These three components work together to provide a quick and reliable control loop capable of properly maintaining the laser temperature at the correct setpoint.

PID control has seen a substantial amount of study and development, with particular emphasis on tuning rules, identification methods, and adaption strategies. These systems use three parameters to determine the output of the control loop: proportional gain, integral time constant, and derivative time constant. These

parameters can be adjusted to improve the performance of the control loop, making it more stable and responsive. The process of finding the optimal values for these parameters is called tuning, which is typically done through an iterative process of adjusting the parameters and observing the results until the desired stability and reactivity are achieved. This is usually done through trial and error method [124].

A PID control system is a type of feedback controller that is commonly employed also in Raman spectroscopy systems to manage the heat dissipation of the laser source [125]. The laser is needed to excite the sample, and the temperature control system is an indispensable component, as it ensures the stability, reliability, environmental sensitivity, and optimal performance of the laser system.

The stability of the laser is a critical factor in achieving accurate and consistent Raman scattering measurements. If the laser temperature is not stable, it could result in fluctuations in the laser's output power, and frequency, which would ultimately impact the quality of the Raman spectra [126, 127].

To prevent such inconsistencies, a temperature control system helps maintain the stability of the laser temperature by compensating for any changes in the ambient temperature or humidity. This ensures that the laser operates at a constant and stable temperature, which, in turn, results in consistent and reproducible Raman spectroscopy measurements.

Raman spectroscopy systems are often used in a variety of operating environments, including laboratory, industrial, and field settings. These environments could experience changes in temperature and humidity, which could impact the laser's temperature.

In the study, we optimized a commercial temperature control system for our specific setup using the established Nichols–Zeigler optimization methods [128]. The goal of the optimization process was to comprehensively assess the relationship between temperature and various laser sources in terms of changes in peak frequency and output optical power, with the objective of enhancing the performance and repeatability of the measurements. The optimized temperature control system was tested on three different laser sources with power outputs of 10 mW, 40 mW, and 100 mW. This allowed us to thoroughly examine the effects of temperature on laser performance across a range of power outputs.

2.1 Temperature effects on laser performance

Maintaining the laser temperature at a setpoint that is optimal for the Raman spectroscopy measurement helps ensure the best possible performance from the system. This helps achieve the highest possible sensitivity, accuracy, and precision

in the Raman spectroscopy, making the temperature control system an essential component in Raman laser driver. In the literature, there are many studies talking about the correlation between temperature and diode laser characteristics such as output optical power, threshold current and voltage, slope efficiency, conversion efficiency, emission spectra, and peak wavelength [126, 127, 129].

Regarding the output optical power, this drops when the temperature rises. This effect is shown in fig. 2.1.B. The output optical power of a Diode-Pumped Solid-State (DPSS) laser decreases when the temperature rises due to several factors. When the temperature of the laser crystal increases, thermal expansion occurs causing the refractive index to change, leading to thermal lensing. This creates a lensing effect that can alter the beam quality and reduce the output power [130]. Increased temperature can also cause the laser crystal to absorb more pump light, leading to thermal loading which reduces the efficiency of the laser and decreases the output power [131].

The threshold voltage increases with increasing temperature. This is because an increase in temperature causes the distribution of electrons and holes to spread out into higher energies, resulting in a greater fraction of injected charge crossing the active region and increasing the leakage current. Thus, a higher threshold voltage is needed to meet the oscillation condition and achieve sufficient gain within the cavity.

The series resistance, an important electrical parameter in diode lasers, can be defined as the ratio of the change in current to the change in the voltage. This parameter decreases non-linearly as the temperature increases.

The slope efficiency or differential quantum efficiency of a diode laser is calculated by combining the internal quantum efficiency, the internal loss, and the loss coefficient. The front facet reflectance and the cavity length influence the loss coefficient. The slope efficiency decreases gradually at low temperatures and rapidly at high temperatures. This is because high temperatures result in an increase in nonradiative recombination and carrier overflow, leading to greater free carrier loss within the cavity and higher internal losses. This results in a reduced differential quantum efficiency [126].

The conversion efficiency of diode lasers is an important parameter that represents the relationship between the output optical power and the input electrical power. The conversion efficiency decreases as the temperature increases. This decrease is due to the increase in temperature leading to a decrease in the optical output power of the diode laser, ultimately reducing the conversion efficiency.

The increase in temperature causes a shift in the peak wavelength, resulting in an increase in a wavelength shift of approximately 0.26 $nm/°C$, as illustrated in

fig.2.1.A. [126, 127, 129]

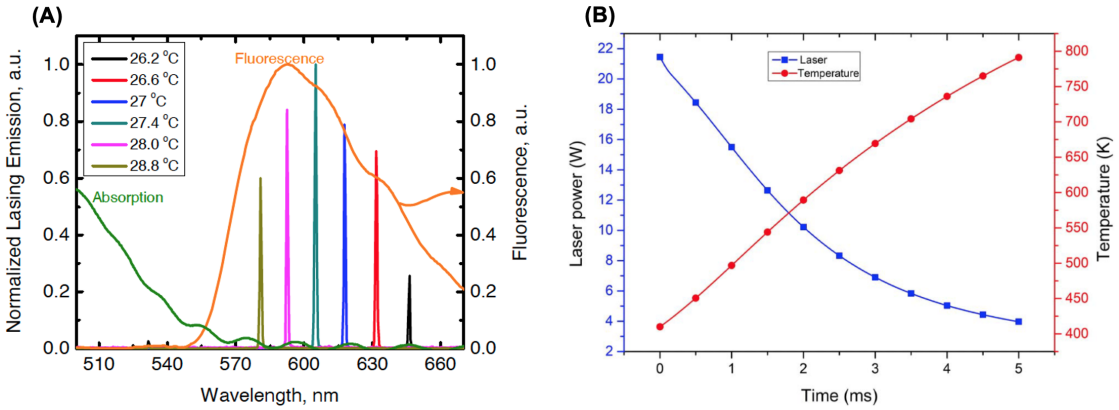

Figure 2.1: Experimental evidence in the literature of the impact of temperature on (A) Wavelength and (B) Laser power, reprinted from [132, 133]

In this study, we explored the impact of temperature on the peak shift and power output of three 532 nm Diode-Pumped Solid State (DPSS) lasers. Two of the lasers were sourced from Thorlabs with power ratings of 10 mW and 40 mW, while the third laser was a butterfly commercial laser (FRLD-532-100-FS-VBG-BTF-1) sourced from Frankfurt laser company. To gather the necessary data, we employed a portable spectrometer and a portable power meter, which allowed us to conduct the experiments in a flexible and convenient manner.

Our findings show that both the 10 mW and 40 mW laser sources displayed stability in terms of peak shift at 532.24 nm for a period of over 15 minutes. However, regarding output power, the 10 mW source showed no impact from temperature changes over time, while the 40 mW source demonstrated instability in response to temperature increases. This highlights the importance of implementing a temperature control system in order to mitigate the effect of temperature on the laser performance and ultimately improve the accuracy of the final measurements for our wearable application. These results are presented in fig.2.2 and demonstrate the stability of the laser sources over time.
In fig.2.2 is represented the experimental results of the stability experiment for both the laser sources.

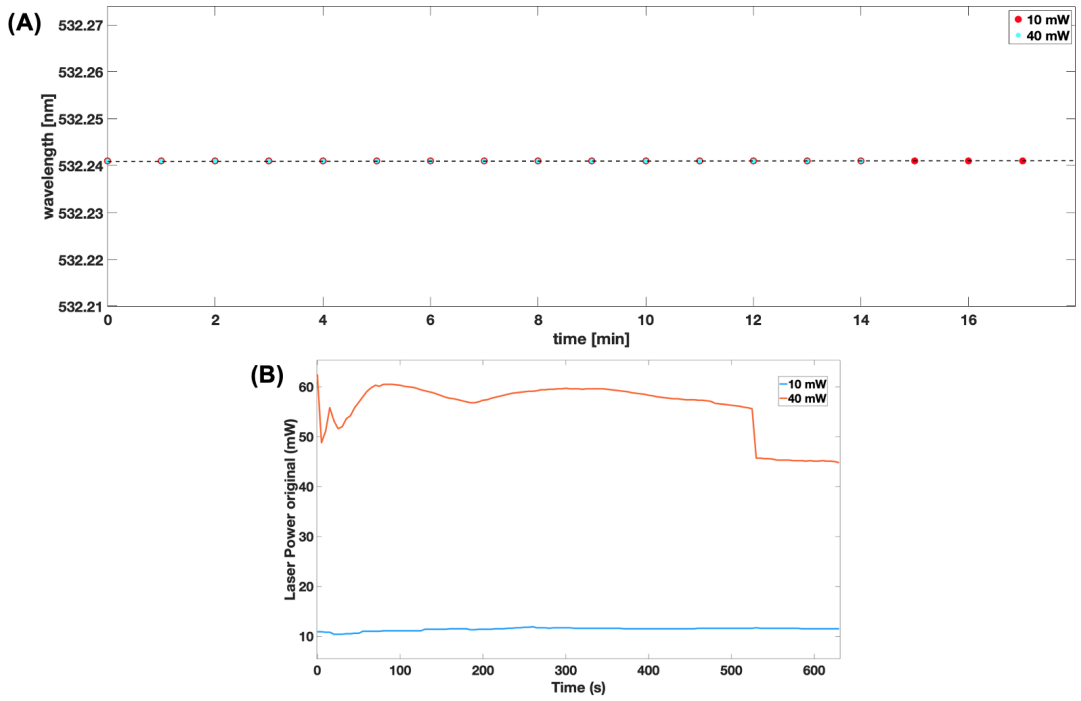

Figure 2.2: Experimental evidence of the impact of temperature on (A) Wavelength and (B) Laser power.

2.2 Thermoelectric cooler (TEC) systems

Thermoelectric Cooler (TEC) systems are solid-state energy converters that are composed of multiple thermocouples connected both electrically in series and thermally in parallel. A thermocouple is made of two different semiconducting thermoelements that create a thermoelectric cooling effect (PeltiereSeebeck effect) when a voltage is applied in the correct direction through the connected junction. To improve heat transfer and system performance, a Thermoelectric module typically has two heat sinks attached to its hot and cold sides [134].

TECs have gained popularity in various applications where precise temperature control is needed, including temperature control in laser systems, cooling of electronics, temperature stabilization in spectroscopy and more [135]. Their compact size is a key advantage, making them suitable for tight spaces and portable applications. They also have high reliability [136] and fast response times [137], making them ideal for demanding applications. Furthermore, TECs can be cooled passively or actively, making them flexible for various cooling requirements [138].

In laser systems, TECs are utilized to cool down laser diodes, which can generate a lot of heat. Maintaining the stability and performance of the laser is crucial,

and TECs help achieve this by removing excess heat, preventing the laser diode from overheating and failing. This can cause a reduction in laser output power, wavelength shift, and stability if left unchecked.

TECs can also regulate the temperature of other components in laser systems, such as optical amplifiers and detectors, that may also be affected by temperature changes. In some instances, TECs can stabilize the temperature of the entire laser system, leading to improved stability and reliability of the laser output.

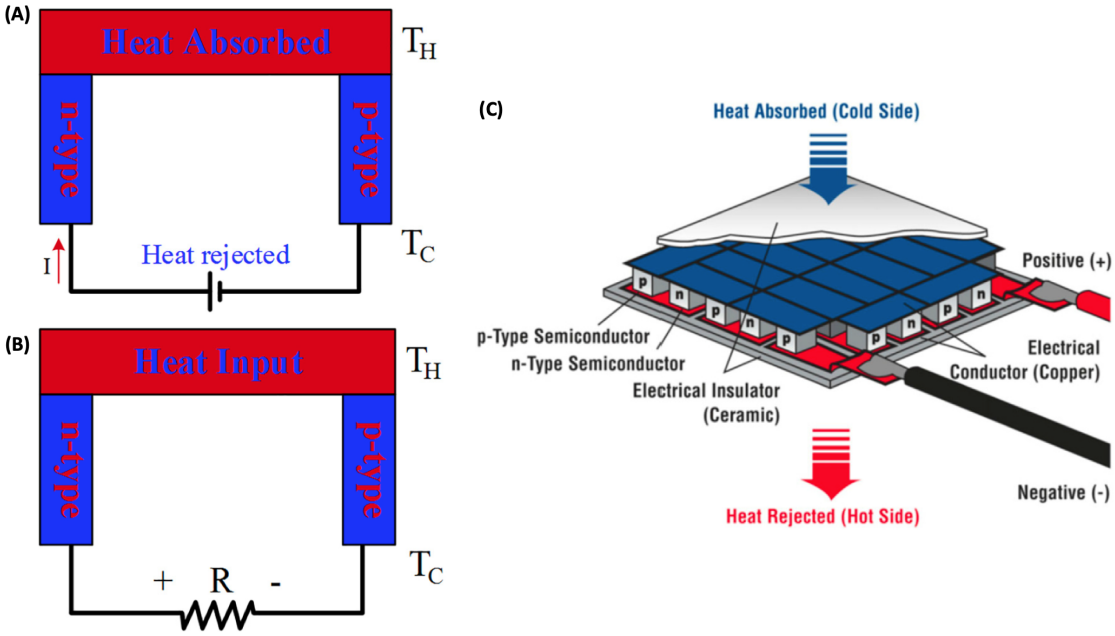

Figure 2.3: A schematic illustration of (A) a thermoelectric cooler (TEC), (B) a thermoelectric power generator (TEG) and (C) a thermoelectric module, reprinted from [139]

The fabrication of thermoelectrics (TEs) mainly uses semiconductors, ceramics, and polymers, with research suggesting that certain polymers such as ethylene-dioxythiophene and carbon fiber polymer-matrix composites possess desirable thermoelectric properties [140].

2.3 PID optimization

PID parameter optimization is the process of fine-tuning the PID algorithm's parameters to obtain the optimal control performance. The appropriate PID parameter values are determined by the features of the process being controlled as well as the intended performance requirements. The optimization procedure

entails determining the best values for the PID parameters in order for the control system to work optimally. PID parameter optimization may be accomplished using a variety of methodologies and techniques, including trial and error, Ziegler-Nichols, and evolutionary algorithms.

PID parameter optimization is crucial for getting the required control performance. A poorly tuned PID control system may cause overshooting, oscillations, and delayed reaction times. An effectively tuned PID control system, on the other hand, may result in precise control, better stability, and decreased variability in the process. As a result, PID parameter optimization is an important part of industrial control systems, and the process should be thoroughly thought out and conducted to guarantee optimum performance.

Our research aimed to assess the necessity of the temperature control system by conducting experiments with two lasers, 10 mW and 40 mW, without using the temperature control system. We then incorporated the temperature control system specifically for the 40 mW laser and optimized the system accordingly, applying the reliable Ziegler-Nichols method. Finally, the results were compared with those obtained from a high-end commercial butterfly laser, providing a thorough evaluation of the effectiveness of the temperature control system.

2.3.1 Nichols–Zeigler optimization method

One effective method for adjusting control parameters is to change them individually rather than all at once. For first-order-with-delay systems, like many thermal systems, the Nichols-Zeigler (N-Z) method is a dependable way to estimate system parameters. If the integral and derivative terms can be turned off, this method works well for trial-and-error adjustments. Although some analog controllers have fixed integral terms, it's possible to bypass the integral by connecting the integrating capacitor directly. To balance out changes in system gains, it's best to tune the control parameters around a temperature that's halfway between the ambient temperature and the desired setpoint.

The optimization process employed a WTC3243 temperature controller from Wavelength Electronics along with a WTC3243 evaluation board. A 10K ohm NTC thermistor from Thorlabs was utilized for temperature sensing, and a centre-hole TEC from TEC microsystem was employed for cooling. Data were acquired in real-time using a bench-top multimeter (HM8012 from HAMEG INSTRUMENTS) and plotted in real-time using an excel user interface. The experimental setup for the temperature control system optimization is illustrated in the accompanying fig.2.5.

The first step was to set the proportional gain in the middle of the range and then

increase it in steps. After each step, a small change to the setpoint was applied. When sufficient proportional gain is reached, the temperature should start to show damped oscillation. If the system begins to oscillate, the gain should be reduced until the damped response is achieved. The value of the proportional gain that starts the oscillation is known as the critical gain (kC), and the optimal gain should be about half of that value.

After determining the amplitude of the oscillations, the period of the oscillation was approximated. If the proportional gain is increased beyond a certain point, the system will start to oscillate continuously with a period known as the critical period (TC). The estimate of the critical period can be derived from the damped oscillations and should be close to within 10% of the critical period. Using the PID controller's independent control form, an initial estimate of the P gain (kP) was made at 0.5 kC, and the initial I term (kI) was set at kP/TC. In the dependent form, the initial proportional gain is kP, and the integral term is 1/TC.

The final values of the P-Gain and I-term were determined through a fine-tuning process, where each parameter was adjusted individually, and the results were compared. This systematic approach, as depicted in fig.2.4, allowed us to identify the optimal combination of P-Gain and I-term by thoroughly evaluating the behavior of the system. Comparing the results from each adjustment provided valuable insights into the system's performance and enabled us to make informed decisions on the optimal parameters.

The N-Z method has been developed through trial and error for many systems that have first-order-with-delay characteristics. However, for thermal systems, the time constant derived from the N-Z method is often too short to be optimal. Moreover, the thermistors and temperature sensors themselves have time constants of about one second. Consequently, it is not recommended to set the control time constant to less than the sensor time constant. If the sensor is located far away from the TEC or if there are several thermal boundaries, the controller time constant needs to be set longer, and the integral gain needs to be reduced [141]. The initial value of the D term can be estimated to be around kPTC/8. If the system exhibits inversion, it's better to avoid using derivative control as any fast changes in current due to noise response could destabilize the load.

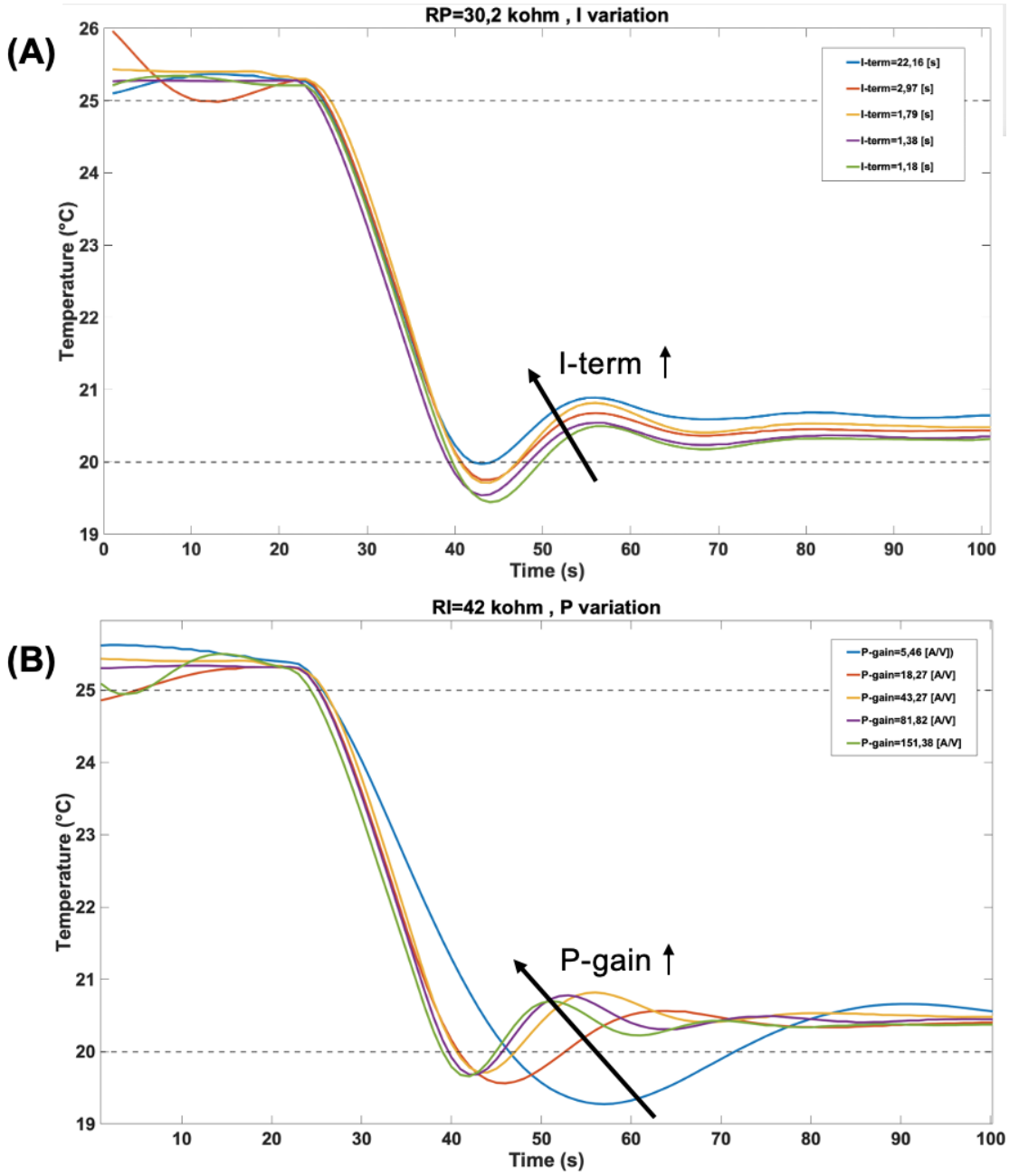

Figure 2.4: Figure A presents the control system response with the P-Gain held constant and the I-term adjusted, while figure B displays the control system response with the I-term held constant and the P-Gain adjusted

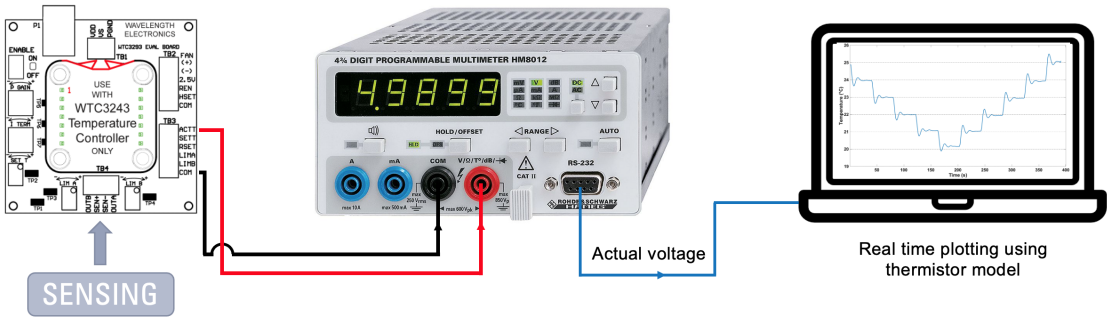

Figure 2.5: Experimental setup designed to enhance and optimize the temperature control system with real-time visualization of temperature changes, providing instant verification of the control system's response.

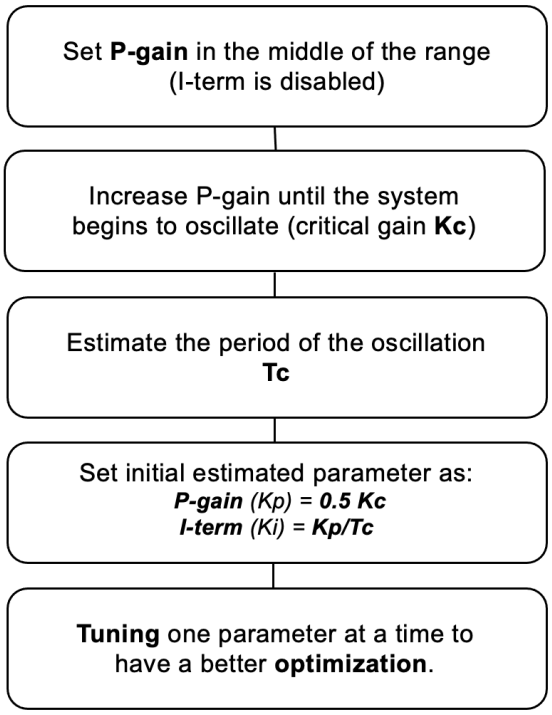

Figure 2.6: Flow diagram depicting the implementation process of the Nichols-Zeigle optimization method.

2.3.2 Optimization results

Prior to optimization, the system's response was characterized by high variability and overdamping, as depicted in fig. 2.7. This was determined through an

experiment where the temperature was forced to a set value using a TEC, and the system's response was evaluated in response to step temperature inputs.

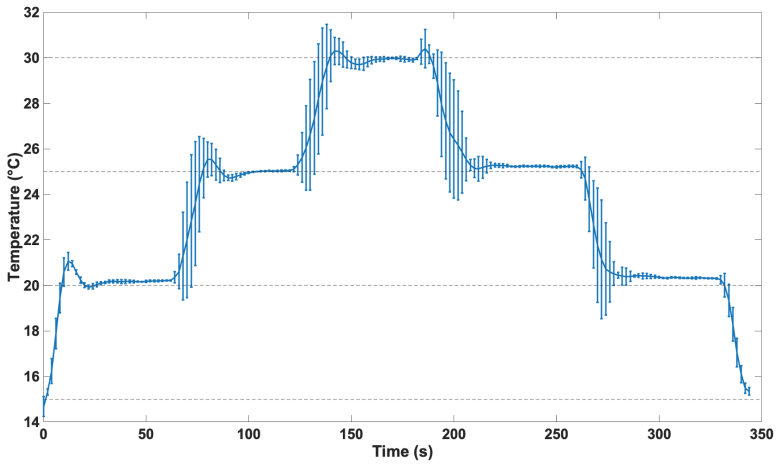

Figure 2.7: Figure illustrates the results of the experiment aimed at characterizing the system before PID optimization.

The optimization process, however, yielded significant improvements in the system's performance, as evidenced by the reduced time response and overshoot. These improvements demonstrate the effectiveness of the optimization method in addressing the initial challenges faced by the system. Specifically, the time response of the system was reduced by 44.18%, and 18.67% reduced the overshoot. These results are presented in fig. 2.8 and demonstrate the positive impact of the optimization process on the system's performance

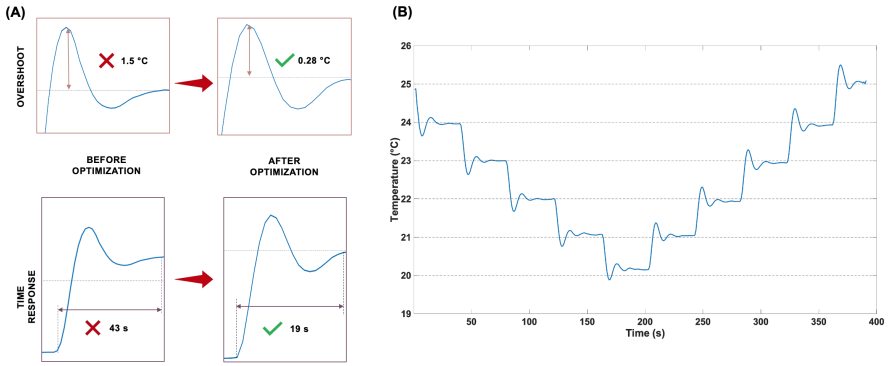

Figure 2.8: This figure illustrates the outcome of the optimized PID system performance. Figure A demonstrates the improvement in overshoot reduction and time response, while Figure B presents a characterization experiment showcasing the system's response to multiple-step temperature inputs.

2.4 Final system test

The efficient cooling of the laser source is a crucial aspect of its operation and is largely dependent on the heat dissipation solutions implemented in the system. The position of the laser source, the use of thermoelectric coolers (TECs), and the selection of appropriate heat sinks and metal mounts all play a significant role in the cooling process. To evaluate the impact of these factors, a comparison was made between the results obtained using a custom-built heat dissipation system for a 40 mW laser source and a commercially available butterfly laser with an optimized heat dissipation system. The output power and peak shift stability of both systems were measured using the same temperature control system.

It is noteworthy that the butterfly laser features an NTC sensor positioned directly next to the laser crystal and the TEC located directly beneath the laser. Contrarily, in the custom-built system, the NTC was placed on the side of the laser, and the TEC was positioned behind the laser source but not in direct contact with the crystal. This resulted in less effective heat transfer due to the thickness of the laser mount. To improve heat dissipation, two heat sinks and a metal mount were used. The described configuration is illustrated in fig. 2.9. It is important to emphasize the substantial cost difference between our system and commercially available systems. Our system has a total cost of approximately 200 CHF, while commercial alternatives typically cost around 2000 CHF. This highlights the potential for our system to provide a more cost-effective solution for Raman spectroscopy applications.

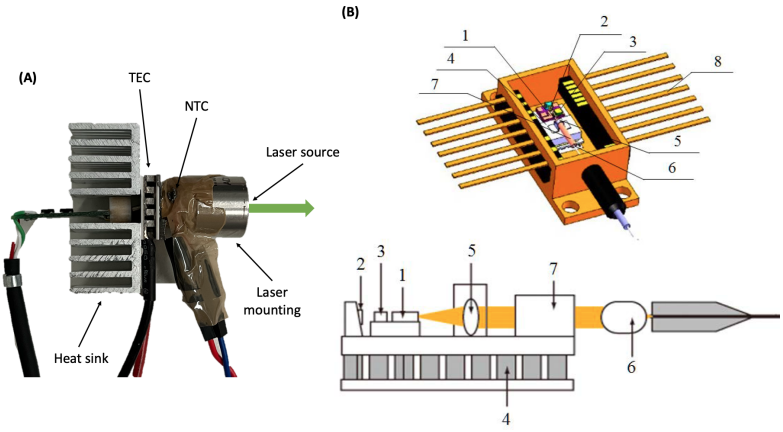

Figure 2.9: This figure illustrates the two different heat dissipations solution adopted. In figure A the in-house-build configuration while in figure B the butterfly laser module structure: 1 – laser crystal, 2 – monitor photodiode, 3 – thermistor, 4 – thermoelectric cooler, 5 – collimating lens, 6 – collecting lens, 7 – optical isolator, 8 – electrical leads.

However, it is also important to consider that our system has limitations in performance and functionality compared to commercial alternatives. Nevertheless, our system provides a proof-of-concept and a starting point for further optimization and development in the future, with the goal of achieving similar performance at a fraction of the cost of commercial systems.

2.4.1 40 mW custom-made configuration

The initial testing phase involved disabling the temperature control system and collecting data solely from the thermistor. This was a crucial step in our experiment, as it allowed us to evaluate the system's performance without the influence of temperature regulation. However, it is worth noting that the experiment had to be terminated after just three minutes due to the laser source reaching a dangerous temperature of 30°C. This posed a significant risk to the operational range of the laser source and thus, the experiment could not be continued. The results, as shown in fig. 2.10, exhibited high fluctuations in the optical output power and displayed a completely unpredictable pattern, highlighting the importance of an effective temperature control system in ensuring consistent and reliable performance.

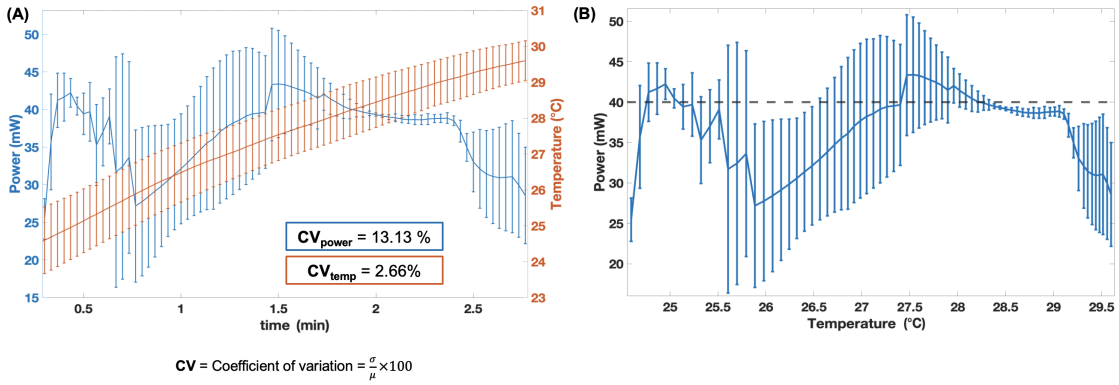

Figure 2.10: This figures presents the results of the experiment in which the 40 mW laser was tested without the use of a temperature control system. Figure A displays the dynamic relationship between Power and Temperature over the course of the experiment, presenting a clear illustration of the fluctuations in both variables over time. Meanwhile, Figure B explores the correlation between Power and Temperature, offering a deeper understanding of how changes in one variable impact the other.

The evaluation proceeded with a second experiment where the optimized temperature control system was utilized. The results of this experiment are displayed in fig. 2.11. The duration of the experiment was 30 minutes and the laser source

stabilized at approximately 28°C, providing a more comprehensive evaluation of the system. Despite limitations posed by the current heat dissipation solution, the results showed a marked improvement in laser stability in the first five minutes, with a smaller coefficient of variation compared to the results obtained without temperature control. This indicates the potential to optimize the system with improved heat dissipation solutions such as a larger heat sink or alternative materials for the mountings. Further efforts should be directed towards refining this optimized configuration, with the goal of developing a cost-effective heat dissipation setup for Raman spectroscopy.

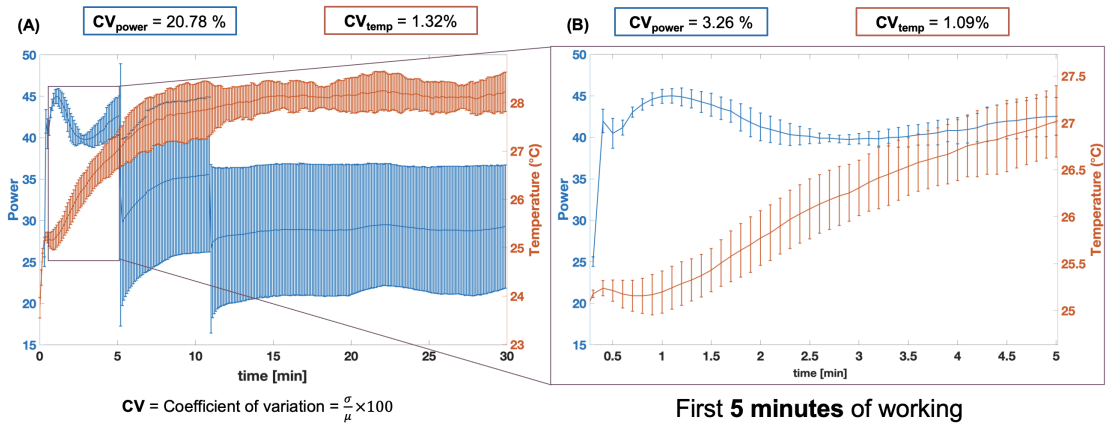

Figure 2.11: This figures presents the results of the experiment in which the 40mW laser was tested without the use of a temperature control system. Figure A displays the dynamic relationship between Power and Temperature over the course of the experiment, presenting a clear illustration of the fluctuations in both variables over time. Meanwhile, Figure B explores the correlation between Power and Temperature, offering a deeper understanding of how changes in one variable impact the other.

In addition to testing the power output, we also evaluated the stability of peak shifts in our experiments. Our results already showed that the laser peak shift was not significantly impacted by temperature, even without the use of a temperature control system. To provide a comprehensive understanding of our results, we have included a comparison of our findings with those of the commercially available butterfly laser in fig. 2.13. This comparison highlights the robustness of our system in maintaining peak shift stability and provides valuable information for those looking to optimize laser performance in applications where peak stability is critical.

2.4.2 Commercial butterfly laser

In this study, we evaluated the impact of temperature on the performance of a commercially available butterfly laser with a power output of 100 mW. The experiment was conducted using a portable spectrometer and a portable power meter to measure the peak shift and power output, respectively.

Given the high output power of the butterfly laser, testing without a temperature control system was not feasible. After only a few seconds of operation, the temperature rapidly reached a dangerous level for the laser source. However, the experiment was performed with the temperature control system optimized using a PID controller, ensuring the stability and safety of the laser.

The results showed that the optimized temperature control system had a significant impact on the stability of the laser's power output. Over the 30-minute experiment, the coefficient of variation of power was just 0.09%, with a maximum variation of 0.4 mW as illustrated in fig. 2.12. This level of stability is compatible with the requirements for Raman spectroscopy applications.

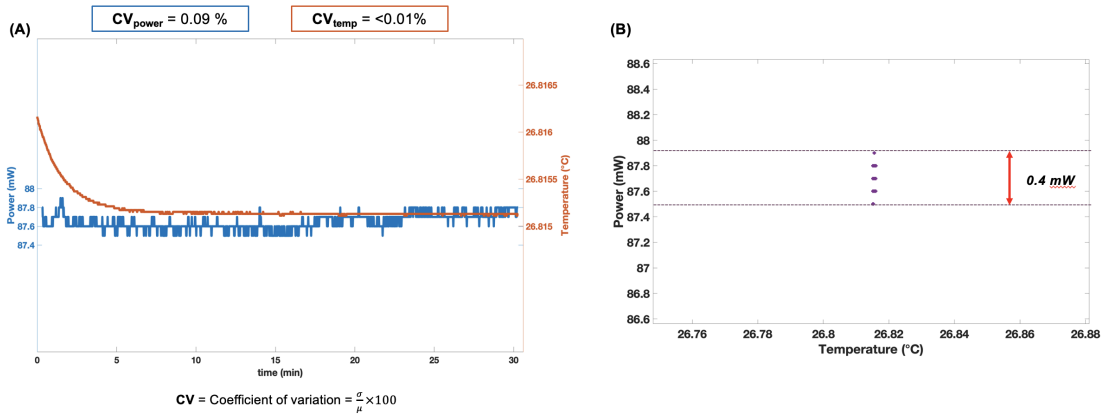

Figure 2.12: This figure presents the results of the experiment in which the butterfly laser was tested with the use of the optimized temperature control system. Figure A displays the dynamic relationship between Power and Temperature over the course of the experiment, presenting a clear illustration of the stability in both variables over time. Meanwhile, Figure B explores the correlation between Power and Temperature, offering a deeper understanding of how changes in one variable impact the other.

The findings of this study highlight the importance of optimizing the temperature control system for high-power laser sources and demonstrate the feasibility of utilizing a low-cost solution for these applications. The results of this study provide valuable information for those looking to design and implement a cost-effective

laser heat dissipation setup for Raman spectroscopy and other high-power laser applications.

Furthermore, our study also evaluated the stability of the peak shift, which is a critical parameter in Raman spectroscopy and other laser applications. The results, presented in fig. 2.13, confirm the stability of the peak shifts over the course of the 30-minute experiment. The constant value of the peak shift throughout the entire experiment suggests that the temperature control system effectively maintained the stability of the laser, even under changing temperature conditions.

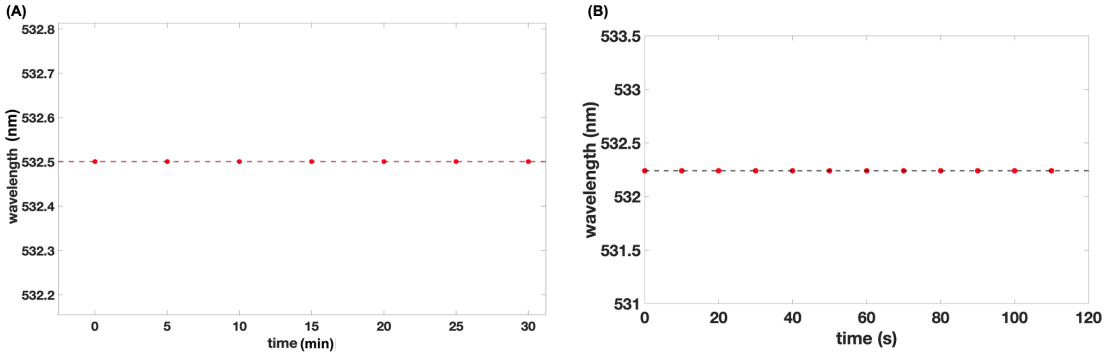

Figure 2.13: In this figure is possible to evaluate an eventual peak shift aviation during the time for (A) butterfly laser and (B) 40mW DPSS laser.

Chapter 3

3D Printed Wearable Raman Prototype

3D printing technology has greatly impacted the field of product design and manufacturing by providing new opportunities for creating intricate designs with speed and accuracy [142]. 3D printing for wearable devices, particularly in health and fitness monitoring, has been gaining prominence in recent years [143]. 3D printing enables fast prototyping and customization of wearable devices, offering new possibilities for personalized health monitoring. Using 3D printing materials that are skin-friendly and flexible enough to move with the wearer has made the production of wearable devices more feasible, and cost-effective [144].

The use of 3D printing technology to create wearable biosensors is regarded as a revolutionary advancement for healthcare applications. This technology has revolutionized the process of constructing free-form objects and personalizing them according to the user's needs. The remarkable features of 3D-printed biosensors include their flexibility, cost-effectiveness, thin and lightweight design. Scientists and industry specialists are continuously striving to develop smaller, quicker, and more effective wearable devices through the utilization of 3D printing technology [145].

The use of 3D printing technology in the development of wearable devices has the potential to improve their quality and functionality and make the development and production process more efficient, and cost-effective [146]. This technology has allowed for the creation of customized wearable devices that are tailored to the unique needs and requirements of individual users.

In this thesis, we delve into the potential of 3D printing technology to transform the field of wearable devices. We focus on exploring various 3D printing techniques used in developing Raman wearable devices. Our work showcases the innovative

solutions developed to constrain all the components in a wearable platform and highlights the impact of 3D printing technology on the quality, functionality, and efficiency of wearable devices.

We provide a comprehensive analysis of different optics mounting solutions, describing the advantages and disadvantages of each configuration. A detailed description of the optical design used to integrate all the components in a wearable case is also presented. Furthermore, we present the design of the first prototype and the final version of the device, showcasing the advancements made in the realm of 3D-printed wearable devices.

3.1 Introduction to Different 3D Printing Techniques

In this section, we will focus on the various 3D printing techniques that were utilized in the realization of our wearable Raman system. Our aim is to provide a comprehensive overview of the advantages and drawbacks of each 3D printing technique, highlighting the key factors that led us to choose the most suitable material and technique for our wearable device. The two main 3D printing techniques that we will be discussing are fused deposition modeling (FDM), multiJet modeling (MJM), as well as digital light processing (DLP).

3.1.1 Fused Deposition Modeling (FDM)

FDM, or fused deposition dodeling, is a commonly utilized 3D printing technique in various industries, including the creation of wearable devices. In the FDM process, layers of materials are printed using a continuous filament of a thermoplastic polymer, as shown in fig. 3.1. Before being extruded on the platform or on top of previously printed layers, the filament is heated at the nozzle to a semi-liquid condition. Because of the thermoplasticity of the polymer filament, it may fuse together during printing and solidify at room temperature once finished. Layer thickness, filament width, orientation, and the existence of air gaps within or between layers are critical processing characteristics that influence the mechanical qualities of printed items [147].

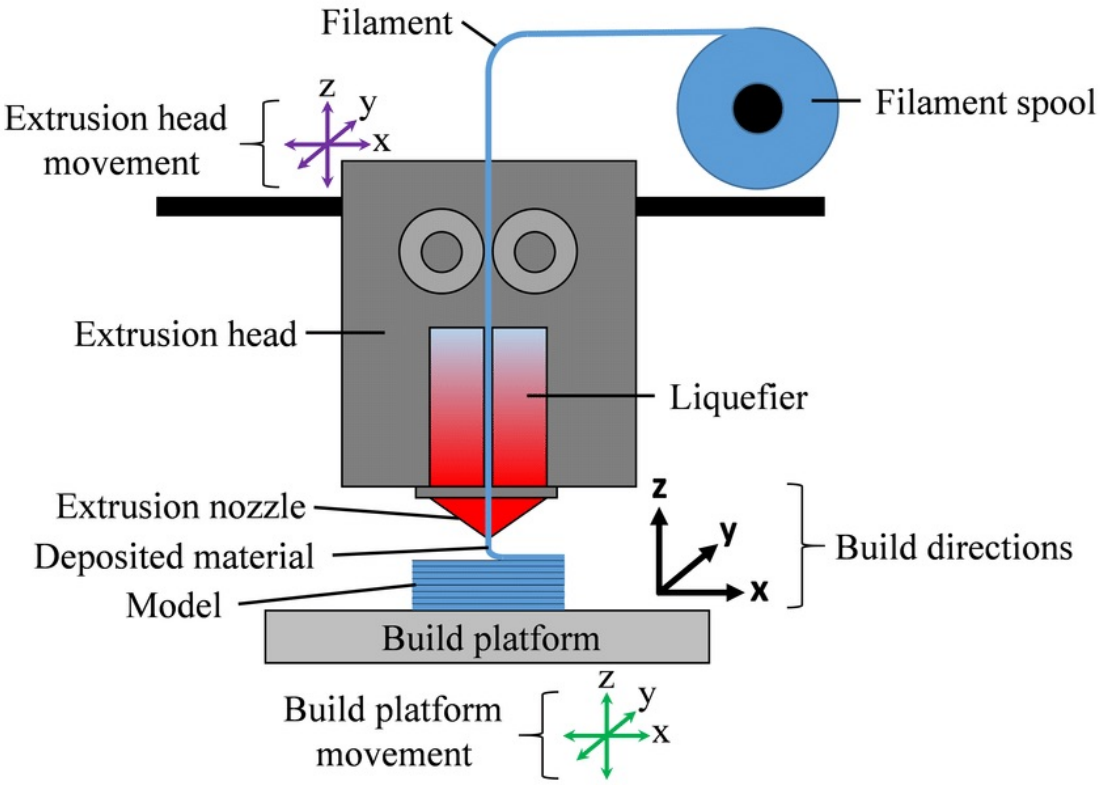

Figure 3.1: Primary elements of an FDM printer are depicted in the figure. The movement in the x, y, and z directions can be accomplished through the motion of the extrusion head (represented by purple arrows) or the build platform (represented by green arrows), or a combination of both. For example, movement in the x and y directions is carried out by the extrusion head while the build platform accomplishes movement in the z-direction. Reprinted from [148]

Advantages

One of the key benefits of using FDM technology is its low cost. The low cost of the process makes it ideal for producing low-volume parts, small prototypes, and even small-scale production runs. Another advantage of FDM is its high speed, which enables fast prototyping of wearable devices and other products.

The simplicity of the FDM process is another major advantage. It involves melting a thermoplastic filament and depositing it layer-by-layer to create the desired 3D object. This makes it a user-friendly and accessible process for designers and engineers, especially those looking to produce prototypes quickly and inexpensively.

FDM is also capable of producing centimeter-sized prototypes, making it a great choice for those looking to produce wearable devices such as Raman systems. Furthermore, the use of inexpensive bio-compatible polymers is another advantage, especially for wearable devices that need to come in contact with the skin.
[148, 149]

Drawbacks

Despite its advantages, there are some drawbacks to FDM. One of the main limitations of the process is the weak mechanical properties of the resulting parts, which can be an issue for certain applications. Additionally, the choice of materials is limited to only thermoplastics, which may not be suitable for certain applications that require a different set of properties.

The layer-by-layer finish of FDM-printed parts can also be a drawback, as it can result in visible layer lines and a less smooth surface finish compared to other 3D printing techniques. Another drawback of FDM is the potential for leakage due to filament bonding, which can be a problem for wearable devices that must be waterproof.

Finally, the difficulty of removing support structures for complex internal features can be a challenge for those using FDM for wearable devices, as the support structures are required to hold the part in place during printing. Inter-layer distortion can also be an issue with FDM, as the layers of material can warp and deform during the cooling process, leading to inaccurate parts.
[148, 149]

3.1.2 MultiJet Modeling (MJM)

MultiJet modeling (MJM) is a photopolymerization process that creates solid 3D objects by curing liquid photopolymer resins layer by layer with a UV light source. The liquid photopolymer resin is fed into the MJM printer and spread in thin layers on a build platform. The resin is hardened by the UV light emitted by the light source, and subsequently, another layer of resin is added on top by lowering the build platform. This sequence is repeated until the desired object is created [150, 151].

Advantages

One of the key benefits of MJM is the high accuracy and surface finish it can provide. The photopolymerization process allows for precise detail and high accuracy, making

MJM a suitable choice for the production of complex and intricate wearable devices. Additionally, MJM enables the combination of different material properties, allowing for the production of flexible, rubber-like, multicolored, and stable components [150].

Another advantage of MJM is its speed. MJM printers can produce objects much faster than traditional 3D printing technologies, making them a suitable choice for high-volume production runs. The technology also enables the production of objects with complex internal features, such as those requirements of wearable devices [152].

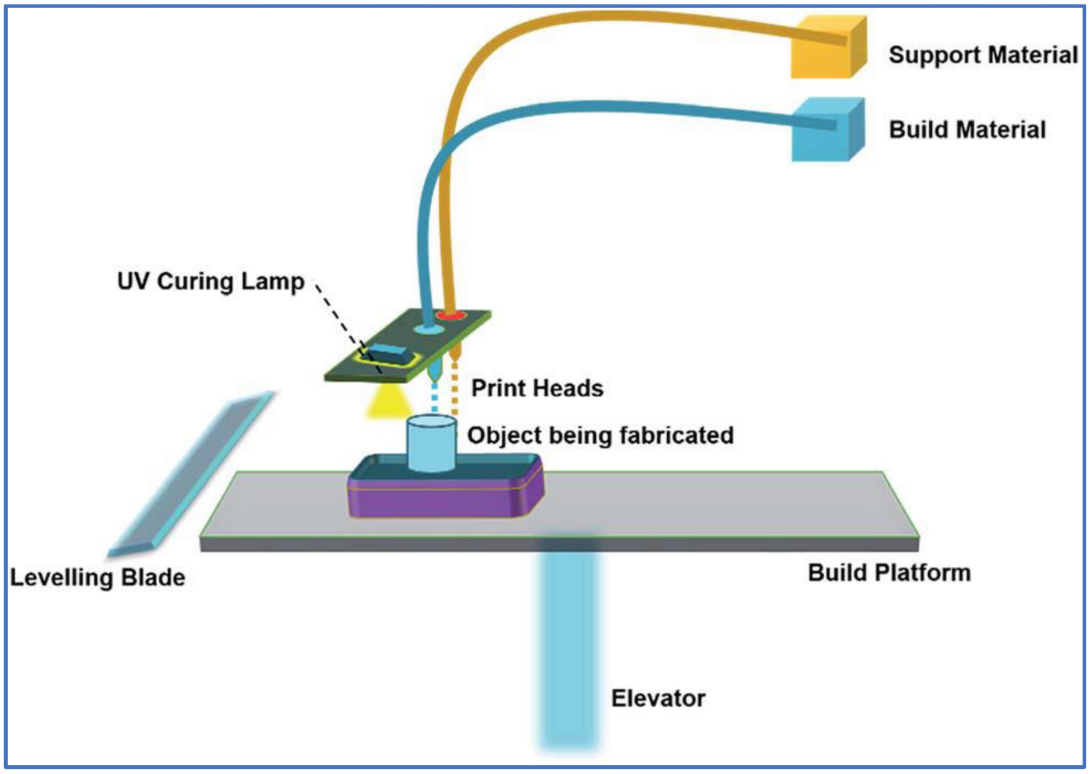

Figure 3.2: Schematic illustration of a MJM 3D printer. Reprinted from [153]

Drawbacks

However, there are also some disadvantages to using MJM technology. One of the main drawbacks is the cost, as photopolymer resins are typically more expensive than the filaments used in other 3D printing technologies like Fused Deposition Modeling (FDM). Another disadvantage is that the build platform used in MJM is

limited in size, making it challenging to produce large wearable devices [152].

Regarding material properties, the heat resistance of components produced by MJM can be limited for some materials. This can be a drawback for applications where heat resistance is required [150].

3.1.3 Digital Light Processing (DLP)

DLP (Digital Light Processing) is a 3D printing technology that uses light to harden photopolymer resins into a 3-dimensional shape. It operates by projecting the cross-section of the object being printed onto a platform covered with photopolymer resin, which is then solidified by being exposed to intense light from a digital light projector or LED array [154].

Typically, the platform is in a container filled with liquid photopolymer resin, and the light source projects an image of the cross-section onto the resin's surface. The light activates the photo-initiators in the resin, causing it to harden into a solid layer. This process is repeated until the whole object has been printed, with the platform raising after each layer to reveal a new layer of resin [154, 149].

Stereolithography (SLA) and digital light processing (DLP) are both forms of 3D printing technology that use light to cure or solidify photopolymer resins into three-dimensional objects. However, there are some differences between the two technologies that make each of them better suited for different applications.

SLA involves using a laser to cure the resin, layer-by-layer, into the desired object. The laser traces the shape of each layer onto the surface of the resin and solidifies it. SLA offers high accuracy and fine surface detail, resulting in objects with smooth surfaces and crisp lines. However, SLA is generally slower than DLP, as the laser needs to trace each layer one at a time [155].

DLP, on the other hand, projects an image of the cross-section of the object onto the resin, which is then cured by a high-intensity light source such as a digital light projector or LED array. This allows for fast print speeds, as the entire layer can be cured at once. DLP also offers high levels of accuracy and fine surface detail, but not as much as SLA [156].

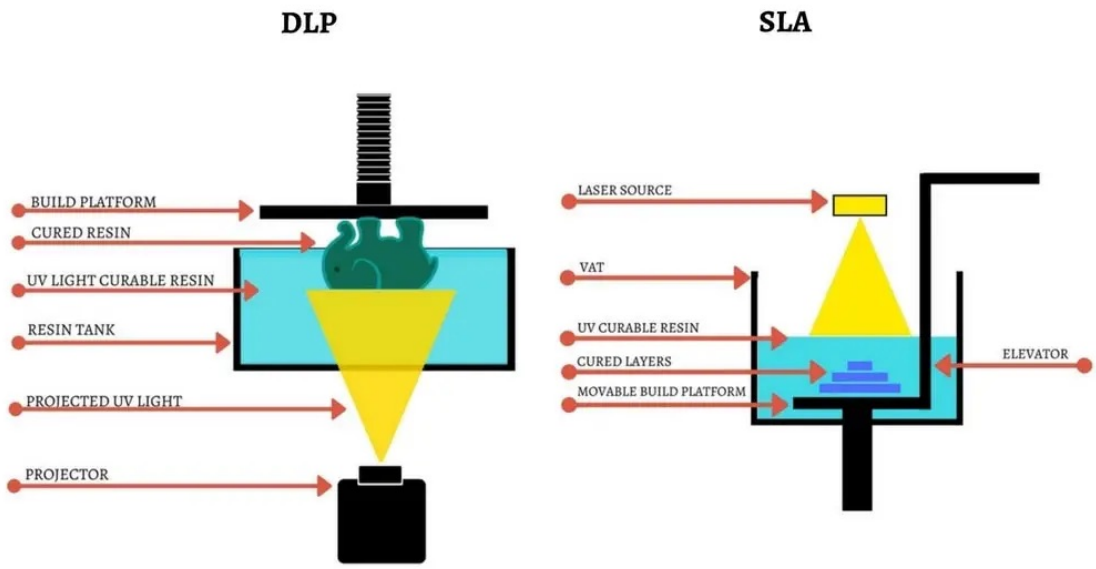

Figure 3.3: Schematic illustration of a stereolithography (SLA) and digital light processing (DLP) 3D printer. Reprinted from [157]

Advantages

DLP 3D printing offers high accuracy and fine surface detail, as the light source projects an entire cross-section of the object in one go. This results in objects with smooth surfaces, crisp lines, and highly detailed features. DLP 3D printing also allows for fast print speeds, as the entire layer can be cured at once. SLA and DLP resin 3D printers are renowned for producing the most polished surface finish compared to other 3D printing methods. Typically, the discrepancies between the two are only discernible on miniature parts or intricate designs[156].

One of the key benefits of DLP 3D printing is that it allows for the production of highly accurate and detailed objects in a relatively short amount of time [158]. This makes it ideal for producing objects with intricate designs, such as jewelry [159] or dental implants [160].

Drawbacks

One major drawback of DLP 3D printing is the cost of the materials. Photopolymer resin, used as the build material in DLP 3D printing, can be quite expensive in mass production compared to other materials used in 3D printing. This can make it less accessible for individuals or businesses just starting out with 3D printing

[161].

Another drawback of DLP 3D printing is the limited build size. The size of the objects that can be printed is typically limited by the size of the build platform, which is often small. This can make it difficult to print larger or multiple objects at once [162].

In addition, DLP 3D printing requires a high level of maintenance. The photopolymer resin used in DLP 3D printing can become contaminated over time, which can affect the quality of the printed objects. The build platform and the light source must be regularly cleaned and maintained to ensure optimal performance[156].

3.2 Optomechanics Design

In this study, we utilized the Inventor software from Autodesk to design the 3D models. The primary objective of our work was to design a custom-made modular organization of the system that would allow for easy fixation of all optics parts. Additionally, we wanted to create a design that would enable effortless removal and installation of replacement parts with simple shapes, thus ensuring maintenance and repair procedures would be less complicated.

To achieve these objectives, we began by studying various shapes and constraint mechanisms to evaluate their advantages and disadvantages, with the aim of selecting the best one for the optics mounting. After careful consideration, we obtained three solutions for the optics mounting, all fabricated using FDM 3D printing technology in acrylonitrile butadiene styrene (ABS) and thermoplastic polyurethane (TPU). The solutions are presented in detail in fig. 3.4.

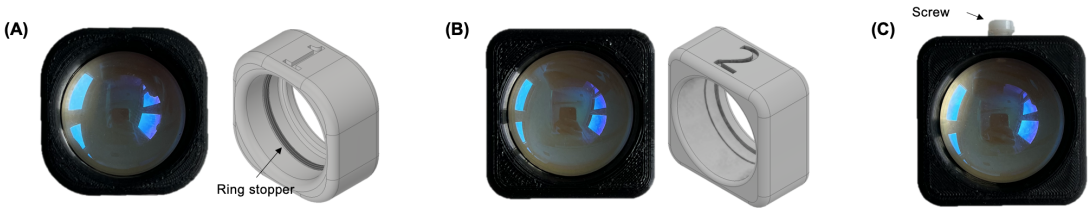

Figure 3.4: This figure provides a visual comparison of three different optics mounting solutions, with each solution utilizing a different method for holding the lens in place. (a) a ring stopper is used to fix the lens in position. (b) utilizes a flexible material to hold the lens in position. (c) employs a more traditional screw stopper to hold the lens in place.

The first mounter produced had its own set of advantages and disadvantages.

On the positive side, it featured a ring joint that securely held the lens, preventing unwanted movements or shifts during operation. This minimized any potential damage or distortion that could occur due to vibration or other external factors. Additionally, the mounter was designed to be tough and durable, capable of withstanding harsh environmental conditions and extended use.

However, there were also some drawbacks associated with this mounter design. One of the main concerns was the difficulty in removing the lens from the mounter. This could pose a significant challenge in situations where lens replacement or maintenance is required. Furthermore, the mounter was not adjustable or adaptable to different lenses and required specific modifications for each lens type, which could be time-consuming and costly.

The second mounter design that we produced had a number of significant advantages. One of the key features of this mounter was the use of a rubber-like material to hold the lens in place. This material provided a secure and snug fit, preventing any movements or vibrations that could affect the performance of the lens. Additionally, this material was easy to work with and could be adapted to fit different lens shapes, making it a versatile and practical solution for a wide range of applications. This means that the second mounter design was also highly adaptable to different types of optic parts: the same mounting solution could be used for a range of different lenses without needing specific modifications or adjustments. This increased flexibility and versatility saved time and resources and made it a more cost-effective and practical option overall.

Another advantage of the second mount is its simple and intuitive design. Unlike the first mount, this design did not require any screws or rings to hold the lens in place, making it easier to use and maintain. The mounting process was straightforward and hassle-free, allowing for faster and more efficient operations.

The third mount design that we produced employed a fairly reliable mechanism with a screw to hold the lens in place. This approach provided a strong and secure hold, ensuring that the lens remained in the correct position and did not move or vibrate during operation. This made it a suitable solution for applications where precision and stability were critical.

Like the second mount design, this mount was adaptable to different optic parts. This meant that the same mounting solution could be used for a range of different lenses without requiring any specific modifications or adjustments. This increased flexibility and saved time and resources.

However, this mounting solution also had some notable drawbacks. The added complexity can cause greater time and resources to manufacture, which could

increase costs and lead to longer lead times.

Additionally, the assembly process for this mounting solution could be uncomfortable and challenging. Using screws to hold the lens in place required a high level of precision and attention to detail during the assembly process. This could make it more time-consuming and require greater skill to install and maintain properly.

After thoroughly evaluating the three different optics mounting solutions presented, we have decided to move forward with the second prototype. This mounting solution, which utilized a rubber-like material to hold the lens, offered several advantages over the other two options.

After the initial evaluation of the first prototype, we recognized the need to further develop our mounting solution. As a result, we decided to produce a second prototype using TPU, which incorporated several key design changes to improve its functionality and adaptability.

One major change was the addition of a protrusion on the base of the mounter, which would provide a more secure and stable hold for the lens. Additionally, we created a proof-of-concept platform to test the constraint and ensure that the mounting solution would work correctly. This platform was designed with a hole insertion point for the mounted lens, which allowed us to control the optics path using the platform design.

Using this platform, we could achieve a modular system organization where all the optics could be easily fixed and removed with a simple configuration. The platform design also allowed us to change the optical path easily, simply by swapping out the board. This provided a more versatile and adaptable solution, which could be customized for a range of different applications and use cases. This solution is shown in fig.3.5.

In order to improve upon the first two prototypes, a third design was necessary due to the stringing effect and low surface detail that resulted from using FDM 3D printing methodology. To address these issues, we searched for a more suitable material and printing technology that would allow us to produce high-quality parts with the required flexibility and resilience. Our research led us to the use of stereolithography and E-gum material for the production of the new mounter parts.

E-gum was chosen for its unique properties, which make it ideal for the purpose of holding the lenses securely in place without causing any damage or distortion. This rubber-like material is known for its high flexibility and durability, and it can stretch and bend without breaking, making it well-suited for a range of applications where resilience is critical. By using stereolithography, we were able to produce high-quality parts with a smooth surface finish and intricate details.

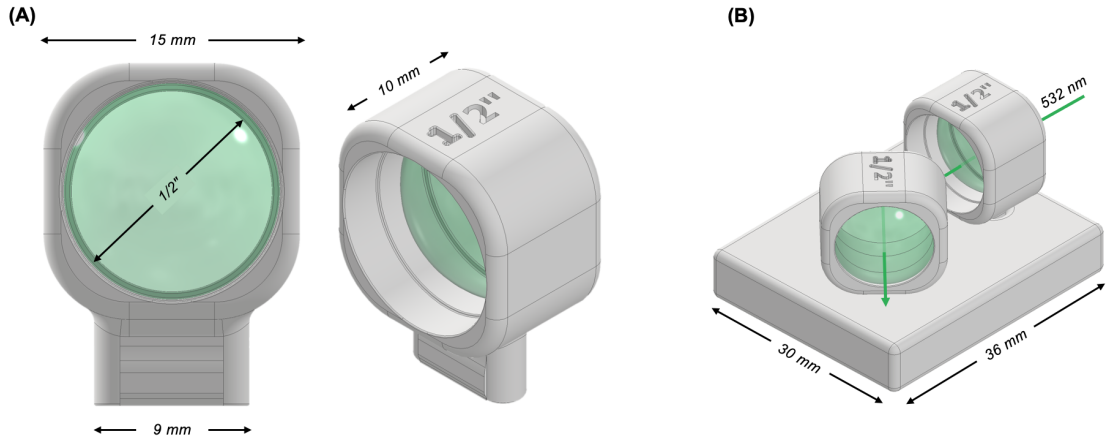

Figure 3.5: (a) presents the 3D model of the second prototype for the lens mounter. This model was developed using TPU, with a protrusion on the base of the mounter to hold the lens securely in place. (b) shows the proof-of-concept constraint mechanism developed to test the functionality of the mounting solution. This mechanism was designed with a hole insertion point for the mounted lens, which allowed us to control the optics path using the platform design.

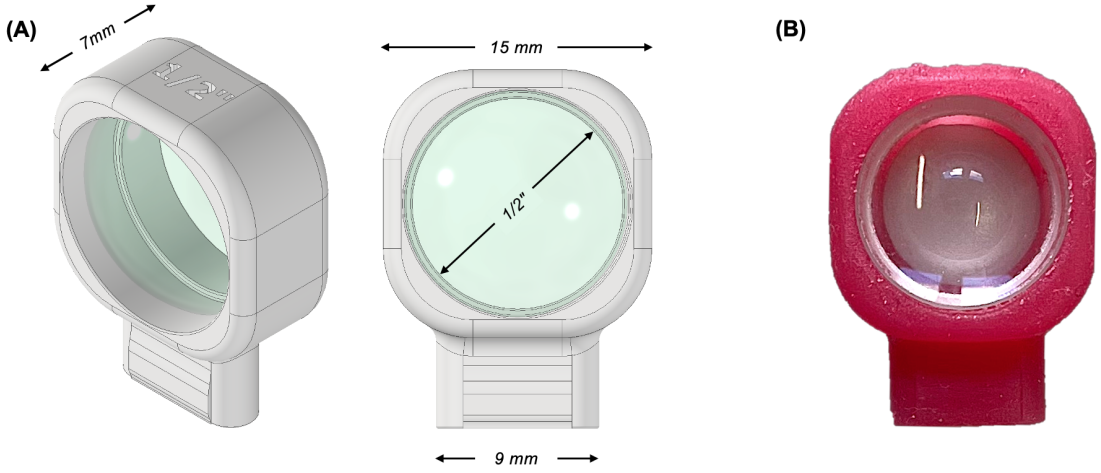

Figure 3.6: (a) presents the 3D model of the third prototype for the lens mounter. (b) shows the actual model was developed using E-gum, with a protrusion on the base of the mounter to hold the lens securely in place.

3.3 Optics

In this study, we aimed to design two Raman systems that meet the specific requirements for our application. The first step of the design process involved a comprehensive study of different Raman architectures and their potential use in our system. We analyzed the functions of each optical component to determine which ones were necessary for our system and evaluated different solutions from top companies in the field, such as Thorlabs and Edmund Optics.

After an extensive evaluation of various optical components, we compiled a list of necessary components and evaluated the overall cost of the device presented in the tab. 3.1. By fabricating the optomechanical components on our own, we were able to significantly reduce the final product's cost. It is important to note that

List	Brand	Cost
Laser Line Filter	Edmund optics	€ 340,00
Notch Filter	Edmund optics	€ 479,00
Bandpass Filter	Edmund optics	€ 160,00
Dichroic Mirror	Edmund optics	€ 190,00
Thermistor	Thorlabs	€ 4,43
Focus Lens	Edmund optics	€ 143,00
Objective	Edmund optics	€ 4.002,00
Lens converter mount	Thorlabs	€ 16,20
Total		€ 5.334,63

Table 3.1: Here are presented the costs of all the optics components

the cost and size of the device are limited by the objective, particularly its high size. However, the miniaturization of objectives is now a routine process, and this aspect can be improved in the future.

3.4 Wearable Device Design

In our work, we aimed to design a wearable Raman system that can contain all the necessary components in a single device without needing any external spectrometer or power supply. The first Raman system we designed utilized an in-house-built laser system consisting of a diode-pumped solid-state (DPSS) laser and various beam shaping and steering optics to generate the desired wavelength and power output. Our primary goal was to provide an economical solution for our application's specific needs.

For the second Raman system design, we chose a commercial butterfly laser instead of an in-house-built laser system. This laser offered better stability and reliability, leading to higher-quality data collection. We designed the system to integrate the butterfly laser in a compact design while also optimizing the optical path to minimize losses and improve performance.

Throughout the design process, we carefully selected materials for different optical components, such as lenses, mirrors, and filters, based on their required optical characteristics. By utilizing our expertise in designing optical systems, we were able to create two Raman systems that met our specific needs and budget constraints while also providing reliable and high-quality data.

3.4.1 First prototype

The objective is one of the critical components of the system. It needs to be perpendicular to the skin to obtain a signal in Raman spectroscopy. Our goal was to reduce the height of the device as much as possible to make it more wearable. To achieve this, we folded the system, keeping the objective perpendicular to the skin while flipping the other part parallel to the skin.

The laser source we used was a 532 nm 40mW laser source DPSS. We chose this specific laser as it provides the ideal wavelength for exciting Raman scattering in biological molecules, as well as being suitable for measuring sweat components such as glucose, lactate, and urea. The beam expander was necessary to fulfill the pupil dimension of the objective.

To reduce the energy of the beam and obtain a narrow band, we used a neutral density filter and line filter. These filters attenuate the high-intensity laser beam, which can cause sample damage and saturate the detector.

The dichroic mirror played a vital role in guiding the laser beam toward the objective. This mirror reflects light at a specific angle while transmitting it at another angle. It helps to focus the laser beam accurately and efficiently on the

sample while also reflecting the signal obtained from it.

After passing through the objective, a microfluidic chip for sweat collection was placed to collect the sample. The signal obtained from the sample comes back through the dichroic mirror toward the CMOS sensor after passing through a bandpass and notch filter. These filters allow only the desired wavelength of light to pass through to the sensor while blocking other unwanted wavelengths that could cause interference or background noise.

These components work together to form a powerful Raman spectroscopy device that is both compact and wearable, allowing for non-invasive sweat-based diagnostics. By using these components, we can obtain high-quality signals from sweat samples with minimal interference, paving the way for future research and development in the field of sweat-based diagnostics.

The first prototype of the wearable Raman sweat sensor represents a significant landmark in this research, as it demonstrates the feasibility of the optomechanical design. However, the prototype also highlighted several challenges that must be addressed in the next version of the device. The most significant issue was the instability of the laser source, which requires an improved heat dissipation system to ensure stability and consistent power output. The inconsistent power output can significantly hinder the generation of a Raman signal, which is crucial for accurate detection and analysis. Furthermore, the preliminary tests revealed misalignment problems that must be addressed in the second prototype to ensure precise and accurate measurement. Despite these challenges, the first prototype serves as a proof-of-concept for the optomechanical design.

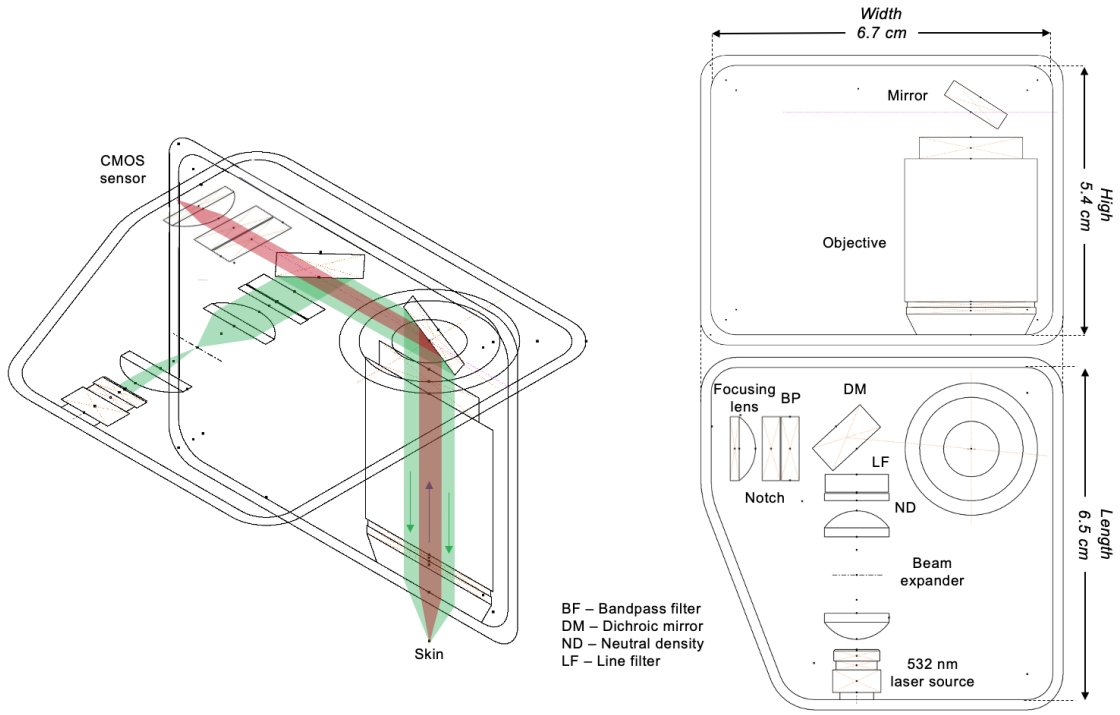

Figure 3.7: Schematic of the first wearable prototype optics.

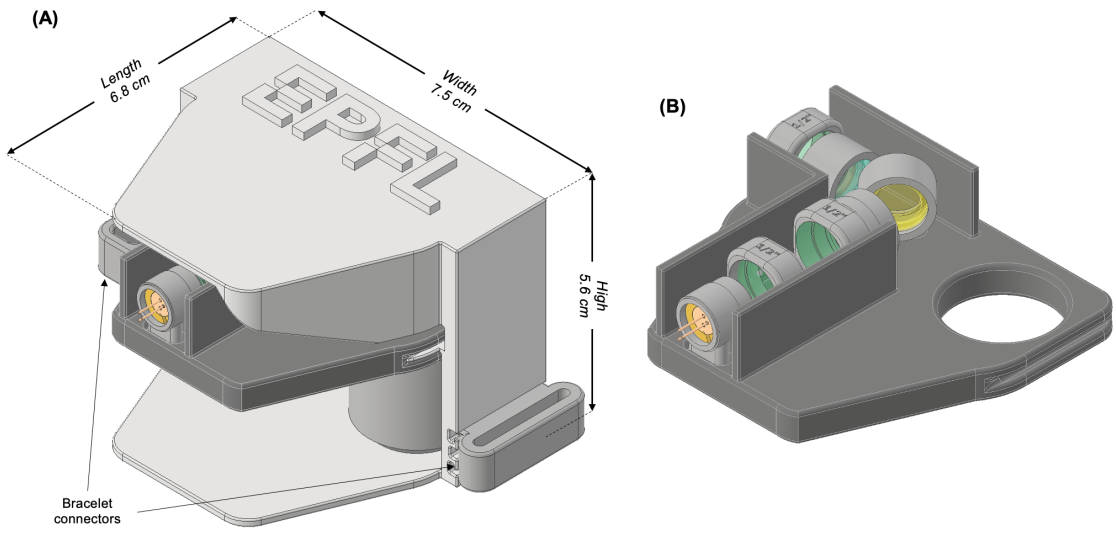

Figure 3.8: 3D model of (A) the first wearable Raman system prototype and (B) optic platform.

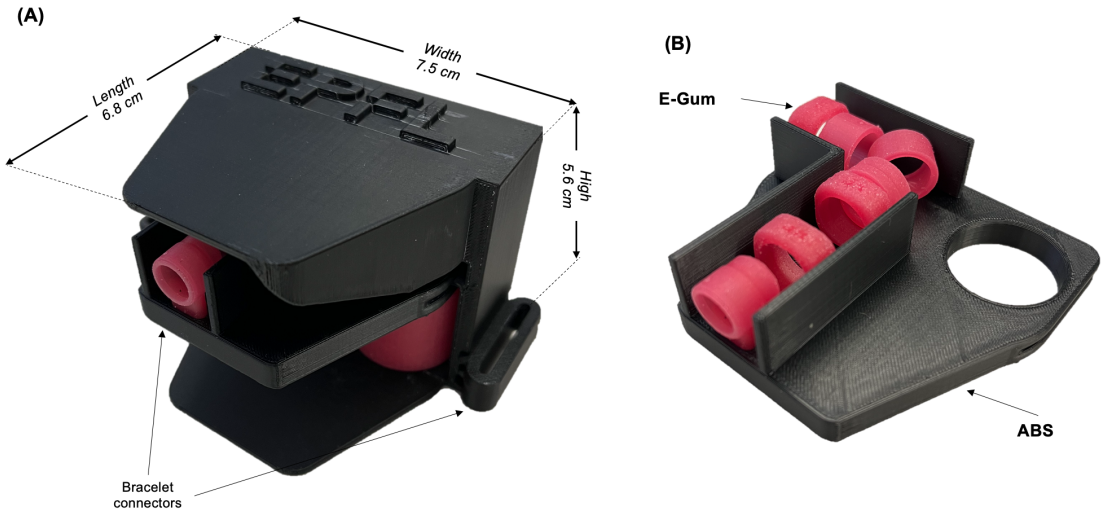

Figure 3.9: Actual prototype of (A) the first wearable Raman system prototype and (B) optic platform.

3.4.2 Final prototype

The schematic representation of the optical design is shown in fig 3.10. The new prototype consists of an improved design that resolves the issues faced in the first prototype, providing a proof-of-concept for the feasibility of the wearable Raman sweat sensor.

The second prototype of the wearable Raman sweat sensor overcomes the challenges faced in the first prototype by using the butterfly commercial laser, which is a more stable and reliable source. The use of the butterfly laser required modifications to the shape and optimization of the spaces, resulting in a design that allows for the proper holding and heat dissipation of the laser. We tried to optimize the space to shrink the size of the device as much as possible, and the final size of the device is 8.8 x 9.5 x 6.5 cm^3 as shown in fig. 3.11. In addition, the CMOS sensor was located at the exact Effective Focal Length (EFL) of 14 mm from the focusing lens, ensuring accurate and precise measurements. The design also features two band connectors on the side of the device, allowing for easy and convenient use by wearing the device on a band.

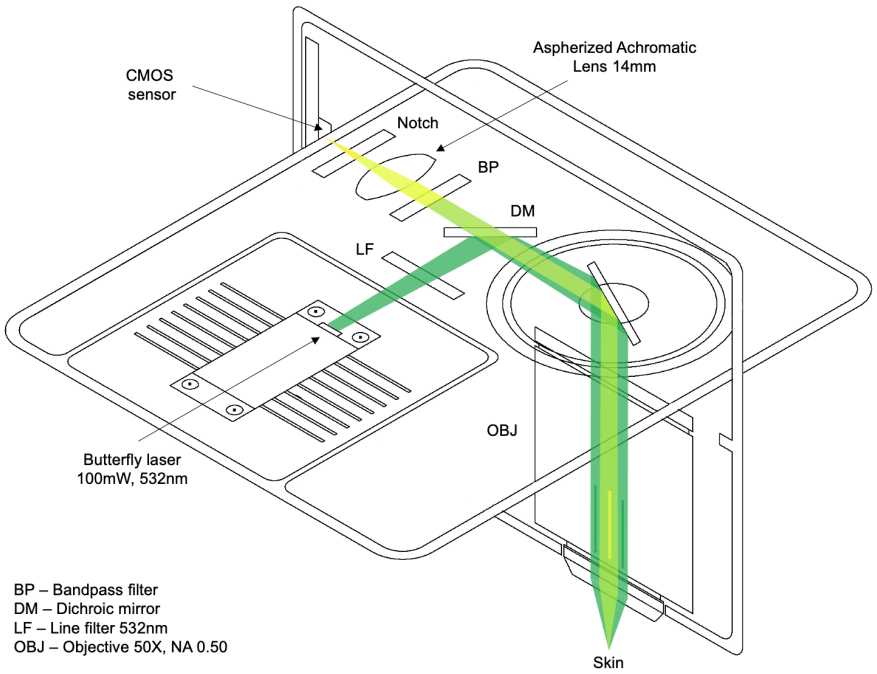

Figure 3.10: Schematic of the final wearable prototype optics.

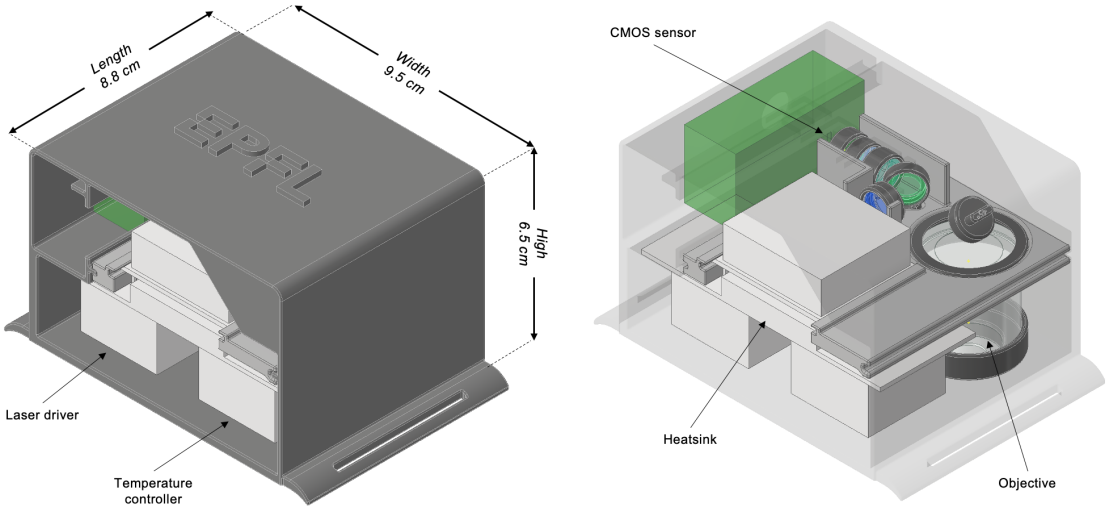

Figure 3.11: The 3D model shown in this figure represents the second version of the wearable Raman system, which showcases the integration of the butterfly commercial laser, the CMOS sensor, and the band connectors, the focusing lens, dichroic mirror, and filters.

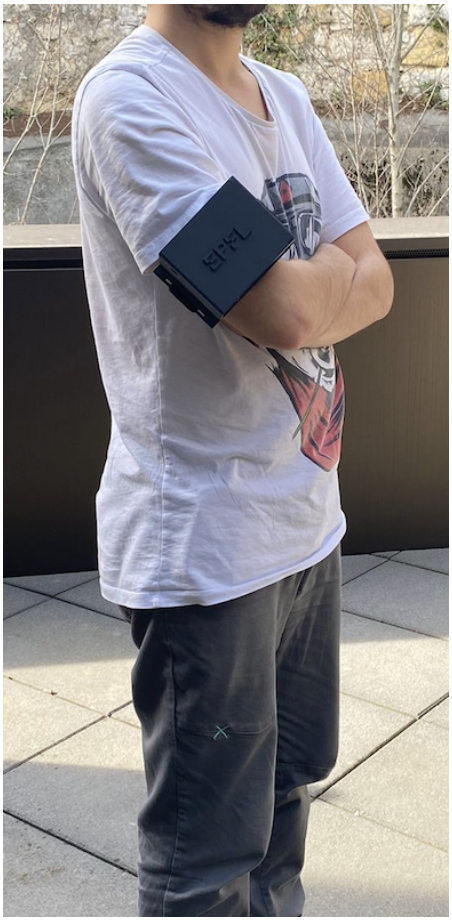

Figure 3.12: The actual all-in-one wearable device worn by a subject using an elastic band.

Chapter 4

Results

To better understand the performance of our wearable Raman system, we designed and conducted an in vitro experiment to explore its behaviour. The experiment setup is shown in 4.1.

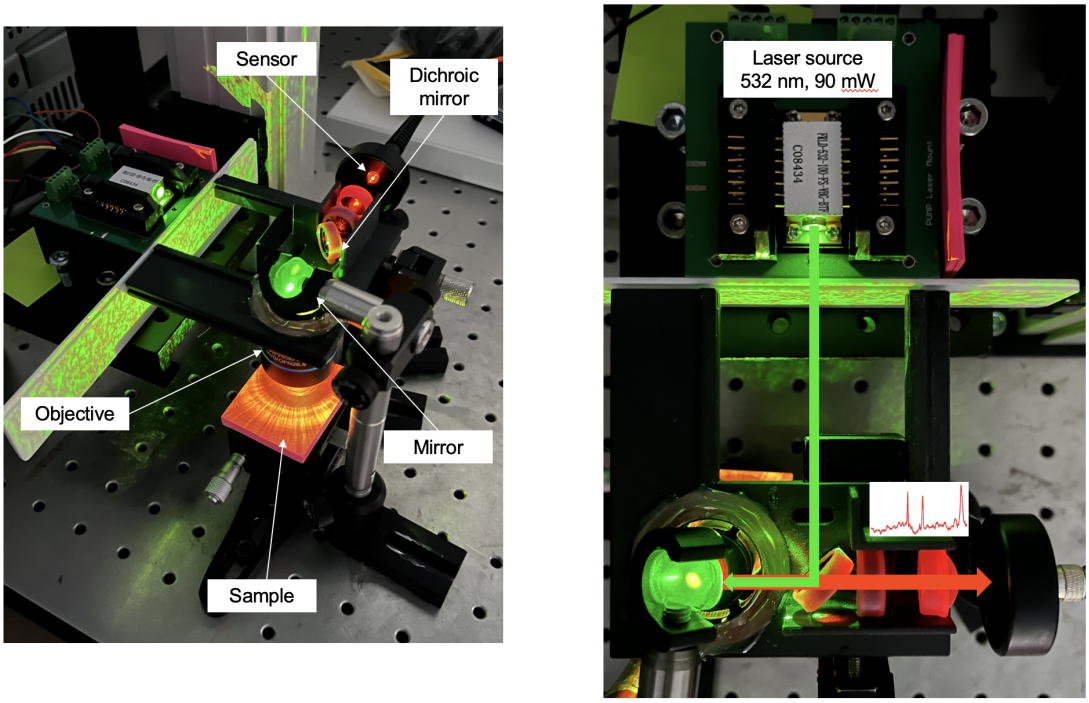

Figure 4.1: In this figure is shown the experimental setup we designed and constructed to explore its behaviour.

To ensure the proper alignment of all the optics components and to accurately

position the spectrometer, fluorescence paper was used to test the system. The HR4000CG-UV-NIR portable spectrometer system, sourced from Oscean Optics company, was utilized to test the system's performance. Several chemical compounds, including lactate, urea, glucose, tyrosine, phenylalanine, ascorbic acid, creatinine, and cholesterol, were tested using this setup to evaluate the performance of our wearable Raman spectrometer. Results are shown in fig. 4.2.

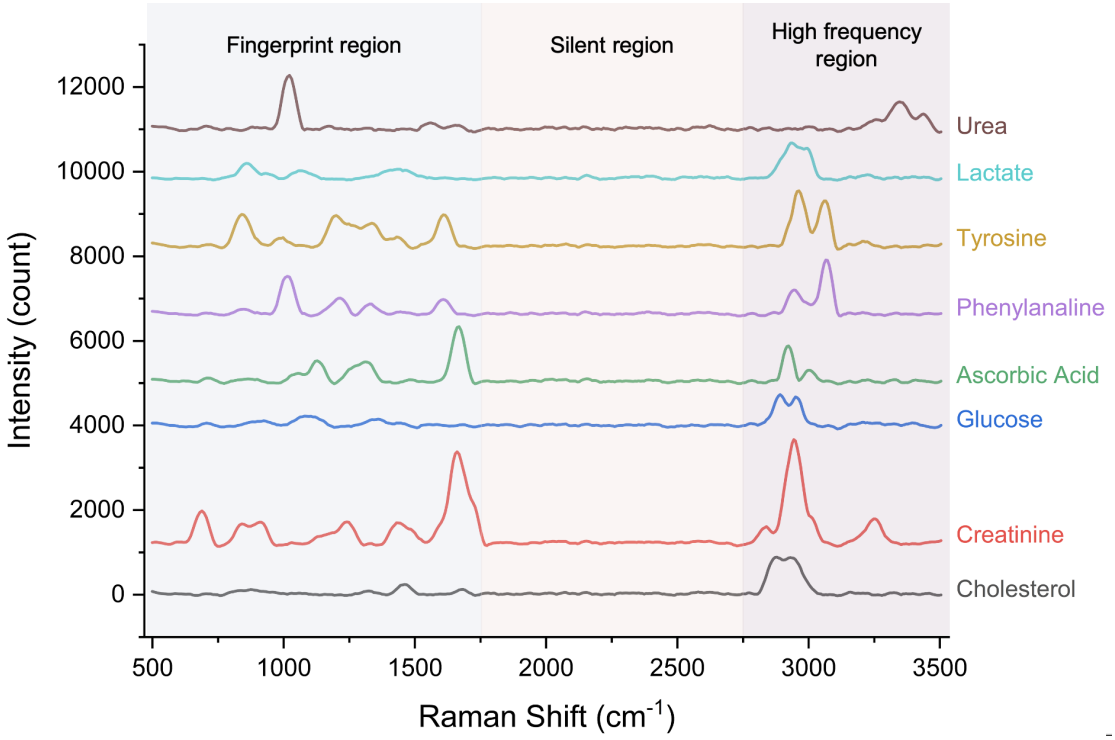

Figure 4.2: The figure represents the Raman spectrum of several chemical compounds that are involved in many biochemical reactions.

The Raman spectra obtained for each compound are displayed in the figure, clearly showing distinctive peaks for each one [163]. These peaks correspond to the vibrational modes of the different molecular bonds present in the sample, and their positions and intensities provide information about the identity and concentration of the compound. The Raman bands and related information for each compound analyzed in our work are presented in Table 4.1. The table includes the peak wavenumber in units of cm^{-1}, as well as the corresponding peak assignment and any relevant information about the chemical structure or behaviour of the compound associated with each peak. For example, lactate has a strong peak at around 860 cm^{-1} [164], while urea has a prominent peak at around 1000 cm^{-1} [165]. Glucose has multiple peaks in the spectrum, including a strong peak at around 1125 cm^{-1},

which is due to the C-O-C stretching mode [164]. Tyrosine and Phenylalanine have similar spectra, with strong peaks at around 1600 cm^{-1} [166] and 1000 cm^{-1} [167], which are due to the C=N and C-C stretching modes, respectively. Ascorbic acid has a prominent peak at around 1600 cm^{-1} [168], as well as creatinine that shows other several peaks around 700-800 cm^{-1} (C-N stretch), 1170-1190 cm^{-1} (C-C stretch), 1300-1330 cm^{-1} (C-N-H deformation), and 1640-1660 cm^{-1} (C=O stretch) [169]. Cholesterol has multiple peaks in the spectrum, including a strong peak at around 1450 cm^{-1}, which is due to the CH_2—CH_3 bending mode [16]. The obtained results demonstrated a high degree of accuracy and precision, confirming the validity and reliability of our system. Furthermore, the observed trends and patterns in the data align with the expected behaviour of the compounds under investigation, which further supports the credibility of our findings.

Raman Band [cm^{-1}]	Peak assignment
Urea	
1000 cm^{-1}	N-C-N stretching mode
1155 cm^{-1}	NH_2 vibration mode
1592 cm^{-1}	NH_2 bending mode
3340 cm^{-1}	N-H stretching vibration
Lactate	
862 cm^{-1}	Ring deformation of the lactate molecule
1062 cm^{-1}	C-C stretching vibration
1438 cm^{-1}	Symmetric CH3 bending mode
2900 cm^{-1}	CH stretching vibration
Tyrosine	
830 cm^{-1}	Out-of-plane bending vibration of C-H
935 cm^{-1}	Stretching vibration of C-C (aromatic ring)
1005 cm^{-1}	Stretching vibration of C-C (aliphatic group)
1065 cm^{-1}	Stretching vibration of C-O
1170 cm^{-1}	Stretching vibration of C-N
1290 cm^{-1}	Stretching vibration of C-C (aromatic ring)
2900 cm^{-1}	CH stretching vibration
3050 cm^{-1}	C-H bending vibrations

Phenylanaline	
1036 cm^{-1}	C-C stretching mode
1208 cm^{-1}	C-H bending mode
1580 cm^{-1}	Aromatic ring stretching mode
1658 cm^{-1}	C=O stretching mode
2900 cm^{-1}	CH stretching vibration
3050 cm^{-1}	C-H bending vibrations
Ascorbic Acid	
750 cm^{-1}	Ring deformation mode
806 cm^{-1}	C-C stretching mode
1005 cm^{-1}	C-C-C bending mode
2890 cm^{-1}	-CH2- symmetric stretching vibration
Glucose	
853 cm^{-1}	C-H deformation vibrations
927 cm^{-1}	C-C stretching vibrations
1,110 cm^{-1}	C-O stretching vibrations
1,439 cm^{-1}	CH_2 bending vibrations
2930 cm^{-1}	C-H stretching mode
Creatinine	
618 cm^{-1}	Stretching vibration of C-C
833 cm^{-1}	Ring breathing mode
1,404 cm^{-1}	Ring breathing mode
1,655 cm^{-1}	Stretching vibration of C=O
2,900 cm^{-1}	CH stretching vibrations
3,300 cm^{-1}	NH stretching vibrations
Cholesterol	
704 cm^{-1}	Ring breathing mode
1,049 cm^{-1}	Ring stretching mode
1,450 cm^{-1}	Bending mode of CH2
2,853 cm^{-1}	Symmetric stretching mode of CH2
2,930 cm^{-1}	Asymmetric stretching mode of CH2

Table 4.1: This table provides an overview of the characteristic Raman bands observed for each compound analyzed in our work. Furthermore, the table includes a brief explanation of the peak assignment, providing an insight into the molecular vibrations responsible for the Raman scattering signal [164, 165, 166, 167, 168, 169, 16].

To further demonstrate the robustness of our wearable Raman system, we conducted experiments on Urea and Olive oil solutions. The results obtained from these experiments 4.3 confirm the efficacy of our system in analyzing and characterizing common solutions. Furthermore, the use of a Band-Pass Filter (BPF) in our system resulted in the removal of unwanted peaks, thus enabling a clear chemical description of the solution analyzed. These findings underscore the potential of our system to be utilized in a variety of practical applications, including those related to solution analysis and characterization

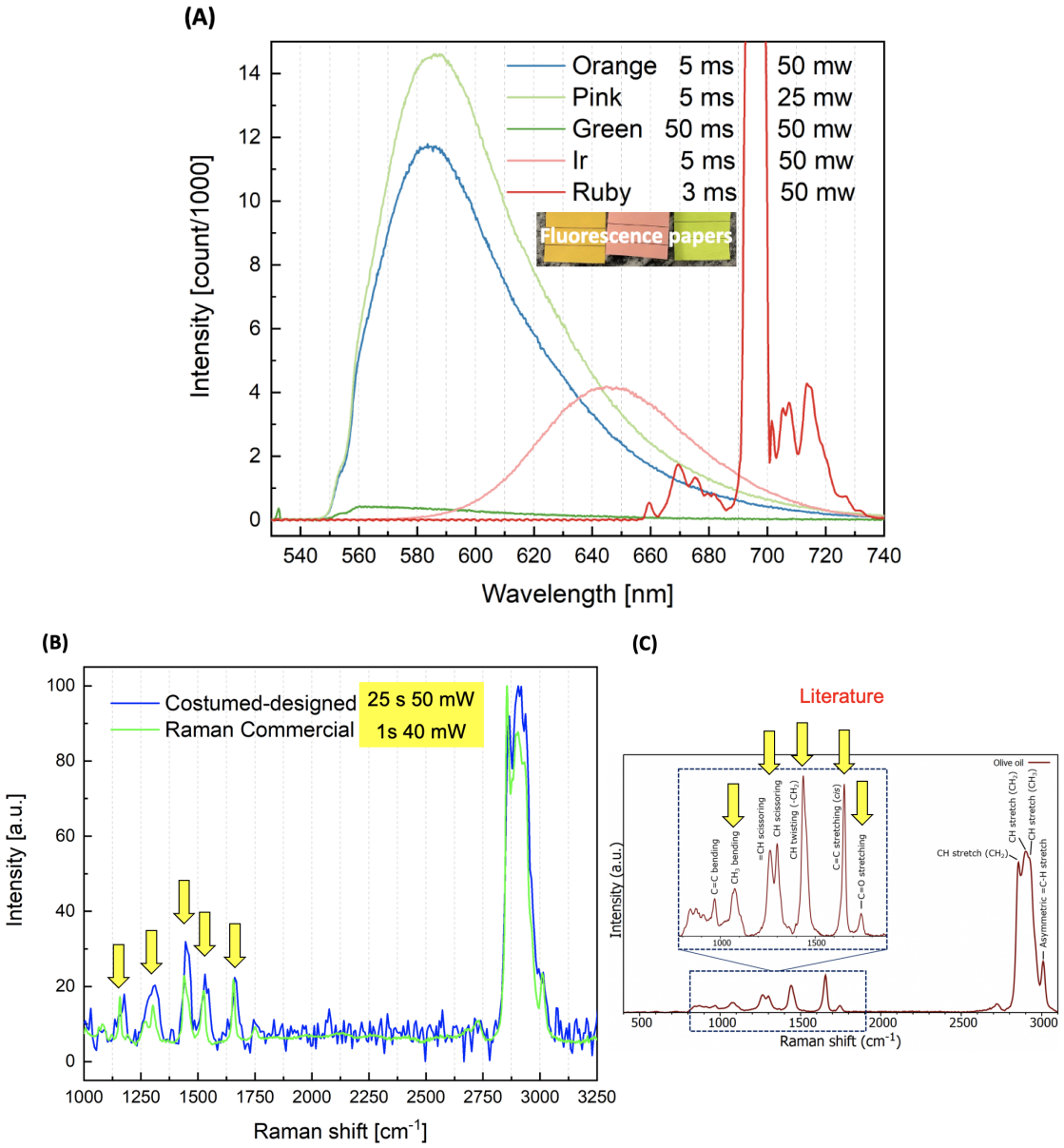

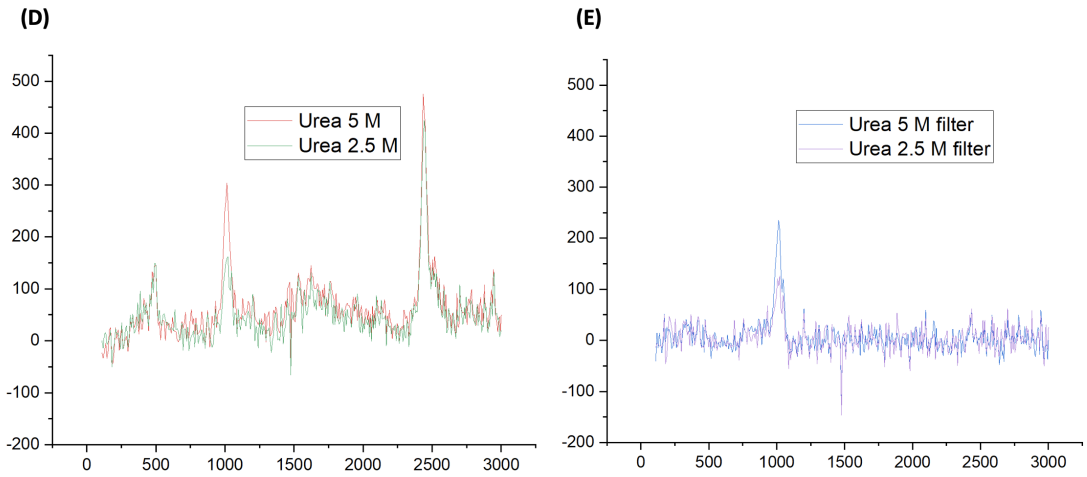

Figure 4.3: This figure presents a comprehensive overview of the results obtained from the solutions analyzed using our wearable Raman system. In fig. a, several spectra of fluorescence papers were obtained. In fig. b, the Raman spectrum of olive oil solution acquired with our wearable Raman system is compared with the spectrum obtained using a commercial Raman system and the spectrum sourced from literature (fig. c). The Raman spectra of Urea solutions at 5 M and 2.5 M both with (fig. d) and without (fig. e) a bandpass filter were also analyzed.

Chapter 5

Conclusions and Future Developments

The research conducted has resulted in the development of a novel wearable Raman scattering-based biosensing system. This system represents a significant advancement in the field of wearable technology by providing a fully integrated, modular, and flexible design for continuous monitoring of biomolecules in real-time.

One of the key achievements of this research was the successful development of an 8.8 x 9.5 x 6.7 cm^3 prototype using innovative 3D printing techniques. This approach allowed for a modular design that facilitated the easy placement of components and flexible mountings for optics. We produced two prototypes, which demonstrated the design's feasibility and effectiveness in integrating optical components. Additionally, we optimized the temperature control system for the laser source using the well-established Nichols-Zeigler method, ensuring the device's optimal efficiency and accuracy.

During the course of the study, our team tested different laser sources and ultimately selected the butterfly commercial laser for its superior performance in terms of optical power output and peak shift stability. However, the results of this study also suggest that there is potential for future research to explore the use of a cheaper, in-house built laser section, provided that proper optimization of the heat dissipation design is achieved.

The final test of the complete system proved that it was possible to obtain a reliable spectrum with this system. This demonstrates the feasibility and promise of the wearable Raman scattering-based biosensing system for real-world applications.

The development of this wearable Raman system has significant potential to improve the efficiency and cost-effectiveness of healthcare delivery while improving

patient outcomes, particularly for those with chronic conditions or those in remote or resource-limited settings. By providing accurate and real-time monitoring of biomolecules, the system can help to reduce the need for invasive and time-consuming sample collection and analysis. Moreover, this research provides a valuable contribution to the development of wearable technology for personalized health monitoring, which is a critical area of research and innovation with tremendous potential for improving human health and well-being.

In conclusion, this research represents an important step forward in the development of wearable technology for biosensing and lays the foundation for future advances in this field. The wearable Raman scattering-based biosensing system has the potential to revolutionize healthcare delivery and improve patient outcomes, and we are excited to see how this technology will evolve and impact the field of biosensing in the years to come.

5.1 Limitations and Future Developments

While our wearable Raman system has shown promising potential for biosensing applications, there are still several limitations that must be addressed to achieve optimal performance. One of the major limitations was the use of a spectrometer that was not low-noise enough for exploiting the full advantage of the device for analyzing solutions in Raman spectroscopy. In response to this, we decided to use a CMOS sensor for acquiring data and transmitting results via Bluetooth.

Based on the promising results obtained in this study, the next phase of our research will focus on optimizing the wearable Raman system for biosensing applications. This will involve expanding our testing to a wider range of biological fluids, such as sweat, and identifying the specific biomarkers present in these fluids. We will explore the potential of our system to accurately detect and quantify these biomarkers, which could have significant implications for healthcare monitoring.

To improve the performance of our system, we plan to include a bandpass filter in order to detect only one peak of interest, eliminating the need for a spectrometer capable of multi-peak detection. This will allow us to use a one-pixel CMOS sensor to detect a single-dimension signal corresponding to the peak of interest for a specific compound.

Appendix A

Additional Content

A.1 PID optimization

MATLAB code for visualizing and optimize PID temperature control system.

```
clc; close all; clear all;

%Thermistor paramethers
R25=10000;

% R range 3.599*10^3 to 681.6
a=3.3530481*10^-3;
b=2.5420230*10^-4;
c=1.1431163*10^-6;
d=-6.9383563*10^-8;

path='/Users/marcofranchini/Library/Group Containers/UBF8T346G9.
    OneDriveStandaloneSuite/OneDrive - Politecnico di Torino.
    noindex/OneDrive - Politecnico di Torino/Università/Svizzera/
    Tesi/TEC control/Gain_experiment/P-GAIN/';

Ibias=100*10^-6;

Rp = 30.2*10^3;
P=(100./((100000/Rp)-1));
%Pgain = 8.85/2;
%Rp_gain=100000/((100/Pgain)-1);

Ri = 62.6*10^3;
I=0.53.*((100000/Ri)+1);
%Tc=20;
%Iterm = Pgain/Tc;
%Ri_term=100000/((1.89*Iterm)-1);

```

```
%% PGAIN
% 1kohm
V1= readmatrix(strcat(path,'exp_7.txt'));
V1 = V1(:,4);
Rt1 = V1./Ibias;

% 6,2kohm
V2 = readmatrix('/Users/marcofranchini/Library/Group Containers/
    UBF8T346G9.OneDriveStandaloneSuite/OneDrive - Politecnico di
    Torino.noindex/OneDrive - Politecnico di Torino/Università/
    Svizzera/Tesi/TEC control/Gain_experiment/P-GAIN/exp_3.txt');
V2 = V2(:,4);
Rt2 = V2./Ibias;

...

% Thermistor model
T_K1= 1./(a + b.*log(Rt1/R25) + c.*log(Rt1/R25).^2 + d.*log(Rt1/
    R25).^3);
T_K2= 1./(a + b.*log(Rt2/R25) + c.*log(Rt2/R25).^2 + d.*log(Rt2/
    R25).^3);

...

T_C1= T_K1-273.15;
T_C2= T_K2-273.15;

...

%P1=(100/((100000/Rt1)-1)); % 1kohm
P2=(100/((100000/(6.2*10^3))-1)); % 6,2 kohm

...

figure;
%plot(T_C1);
%hold on;
plot(T_C2,'LineWidth',1.5);
hold on;
plot(T_C2,'LineWidth',1.5);
plot(T_C3,'LineWidth',1.5);
plot(T_C4,'LineWidth',1.5);
plot(T_C5,'LineWidth',1.5);
plot(T_C6,'LineWidth',1.5);
plot(T_C7,'LineWidth',1.5);
plot(T_C8,'LineWidth',1.5);
%plot(T_C9);
% '1kohm','61,7 kohm'
```

```
70 legend(num2str(P2),num2str(P3),num2str(P4),num2str(P5),num2str(P6)
       ,num2str(P7),num2str(P8));
71
72 yline(15,'--','LineWidth',1.5);
73 yline(20,'--','LineWidth',1.5);
74 yline(25,'--','LineWidth',1.5);
75 yline(30,'--','LineWidth',1.5);
76
77 xlabel("Time (s)");
78 ylabel("Temperature ( C )");
79 title(["P-gain experiment"] );
80
81 % save(strcat(path,'test p-gain','.mat'));
82
83 %% ITERM
84
85 path='/Users/marcofranchini/Library/Group Containers/UBF8T346G9.
       OneDriveStandaloneSuite/OneDrive - Politecnico di Torino.
       noindex/OneDrive - Politecnico di Torino/Università/Svizzera/
       Tesi/TEC control/Gain_experiment/I-TERM/';
86
87 % Ri=1kohm
88 V1= readmatrix(strcat(path,'exp_5.txt'));
89 V1 = V1(:,4);
90 Rt1 = V1./Ibias;
91
92 % Ri=11,9kohm
93 V2= readmatrix(strcat(path,'exp_4.txt'));
94 V2 = V2(:,4);
95 Rt2 = V2./Ibias;
96
97 % Ri=21,4kohm
98 V3= readmatrix(strcat(path,'exp_1.txt'));
99 V3 = V3(:,4);
100 Rt3 = V3./Ibias;
101
102 % Ri=31,2kohm
103 V4= readmatrix(strcat(path,'exp_2.txt'));
104 V4 = V4(:,4);
105 Rt4 = V4./Ibias;
106
107 % Ri=41,3kohm
108 V5= readmatrix(strcat(path,'exp_3.txt'));
109 V5 = V5(:,4);
110 Rt5 = V5./Ibias;
111
112 T_K1= 1./(a + b.*log(Rt1/R25) + c.*log(Rt1/R25).^2 + d.*log(Rt1/
       R25).^3);
```

```
T_K2= 1./(a + b.*log(Rt2/R25) + c.*log(Rt2/R25).^2 + d.*log(Rt2/
    R25).^3);
T_K3= 1./(a + b.*log(Rt3/R25) + c.*log(Rt3/R25).^2 + d.*log(Rt3/
    R25).^3);
T_K4= 1./(a + b.*log(Rt4/R25) + c.*log(Rt4/R25).^2 + d.*log(Rt4/
    R25).^3);
T_K5= 1./(a + b.*log(Rt5/R25) + c.*log(Rt5/R25).^2 + d.*log(Rt5/
    R25).^3);

T_C1= T_K1-273.15;
T_C2= T_K2-273.15;
T_C3= T_K3-273.15;
T_C4= T_K4-273.15;
T_C5= T_K5-273.15;

figure;
plot(T_C1);
hold on;
plot(T_C2);
plot(T_C3);
plot(T_C4);
plot(T_C5);

legend('1kohm','11,9kohm','21,4kohm','31,2kohm','41,3kohm');

yline(15,'--','LineWidth',1.5);
yline(20,'--','LineWidth',1.5);
yline(25,'--','LineWidth',1.5);
yline(30,'--','LineWidth',1.5);

xlabel("Time (s)");
ylabel("Temperature ( C )");
title(["I-term experiment"] );
```

Listing A.1: P-gain and I-term optimization code for processing data and plotting

```
clc; clear all; close all;

%Thermistor paramethers
R25=10000;

% R range 3.599*10^3 to 681.6
a=3.3530481*10^-3;
b=2.5420230*10^-4;
c=1.1431163*10^-6;
d=-6.9383563*10^-8;

Ibias=100*10^-6;

```

```
%tensione misurata dal pin ACT T --> fs=1Hz
V1 = readmatrix('exp1.txt');
V1 = V1(:,4);
Rt1 = V1./Ibias;

V2 = readmatrix('exp2.txt');
V2 = V2(:,4);
Rt2 = V2./Ibias;

V3 = readmatrix('exp3.txt');
V3 = V3(:,4);
Rt3 = V3./Ibias;

V4 = readmatrix('exp4.txt');
V4 = V4(:,4);
Rt4 = V4./Ibias;

%kelvin temperature
T_K1= 1./(a + b.*log(Rt1/R25) + c.*log(Rt1/R25).^2 + d.*log(Rt1/
    R25).^3);
T_K2= 1./(a + b.*log(Rt2/R25) + c.*log(Rt2/R25).^2 + d.*log(Rt2/
    R25).^3);
T_K3= 1./(a + b.*log(Rt3/R25) + c.*log(Rt3/R25).^2 + d.*log(Rt3/
    R25).^3);
T_K4= 1./(a + b.*log(Rt4/R25) + c.*log(Rt4/R25).^2 + d.*log(Rt4/
    R25).^3);

%Celsius temperature
T_C1= T_K1-273.15;
T_C2= T_K2-273.15;
T_C3= T_K3-273.15;
T_C4= T_K4-273.15;

%% all graph in one figure

T_C1=T_C1(8:412);
T_C2=T_C2(15:359);
T_C3=T_C3(12:394);
T_C4=T_C4(12:404);

T_C1=resample(T_C1,length(T_C2),length(T_C1));
T_C3=resample(T_C3,length(T_C2),length(T_C3));
T_C4=resample(T_C4,length(T_C2),length(T_C4));

figure;
plot(T_C1,'LineWidth',1.5);
hold on;
plot(T_C2,'LineWidth',1.5);
plot(T_C3,'LineWidth',1.5);
```

```
plot(T_C4,'LineWidth',1.5);
legend("T_C1","T_C2","T_C3","T_C4");
legend('Experiment 1', 'Experiment 2', 'Experiment 3', 'Experiment
    4');
xlabel("Time (s)");
ylabel("Temperature ( C )");
title(["Step experiment"] );

Mean_T = mean([T_C1(1:2:end)'; T_C2(1:2:end)'; T_C3(1:2:end)';
   T_C4(1:2:end)']);
Std_T = std([T_C1(1:2:end)'; T_C2(1:2:end)'; T_C3(1:2:end)'; T_C4
   (1:2:end)']);
t=[0:2:length(T_C1)];

figure;
errorbar(t,Mean_T,Std_T,'LineWidth',4);
yline(15,'--','LineWidth',1.5);
yline(20,'--','LineWidth',1.5);
yline(25,'--','LineWidth',1.5);
yline(30,'--','LineWidth',1.5);

xlabel("Time (s)");
ylabel("Temperature ( C )");
title(["Step experiment"] );
```

Listing A.2: PID system test in the range of work of the laser source

A.2 Laser test

MATLAB code for process signal from different laser sources and evaluate their behaviours.

```
%% 40 mW laser
Pa=[0.1 0.1 0.1 0.1 0.1 1.1 8.6 14.2 22.1 22 16.5 20 29 41]; %mW
Va=[0.00 0.00 0.02 0.07 0.12 0.17 0.19 0.21 0.23 0.25 0.27 0.29
   0.31 0.33]; %V
Ia= Va.*1.2;

figure;
plot(Ia*10^3,Pa,'LineWidth',1.5);
xlabel("Contant laser Current (mA)");
ylabel("Laser Power original (mW)");

%Threshold V = 0.9V for (10mW laser diode)


```

```
S1 = readmatrix("/Users/marcofranchini/Library/CloudStorage/
    OneDrive-PolitecnicodiTorino/Università/Svizzera/Tesi/
    LASER_SOURCE/Laser test/New_laser/40mW/Subt2_20-06-58-047.txt")
    ;
S2= readmatrix("/Users/marcofranchini/Library/CloudStorage/
    OneDrive-PolitecnicodiTorino/Università/Svizzera/Tesi/
    LASER_SOURCE/Laser test/New_laser/40mW/Subt2_20-06-00-758.txt")
    ;

...

Spec(:,1) = S1(:,1);
Spec= [S1(:,2) S2(:,2) S3(:,2) S4(:,2) S5(:,2) S6(:,2) S7(:,2) S9
    (:,2) S10(:,2) S11(:,2) S12(:,2) S13(:,2) S14(:,2) S15(:,2) S16
    (:,2) S17(:,2)];
lambda = S1(:,1);

fwhmx=ones(size(Spec,2),1);

figure;

for i=1:16
    vmax = max(Spec(:,i));
    vmin = min (Spec(:,i));
    %Find the half max value.
    halfMax = max(Spec(:,i)) / 2;
    % Find where the data first drops below half the max.
    index1 = find(Spec(:,i) >= halfMax, 1, 'first');
    % Find where the data last rises above half the max.
    index2 = find(Spec(:,i) >= halfMax, 1, 'last');
    fwhm = index2-index1 + 1; % FWHM in indexes
    % if you have an x vector
    fwhmx(i) = lambda(index2) - lambda(index1);
    plot(S1(:,1),Spec(:,i));
    hold on;
end

xline(532.241,"k--",'LineWidth',2);

[M index]=max(Spec);
peak_shift_40=lambda(index);

t10=0:1:19-1;
t40=0:1:16-1;
figure;
plot(t10,peak_shift_10, 'r.','LineWidth',5,'MarkerSize',20);
hold on;
plot(t40,peak_shift_40, 'c.','LineWidth',5,'MarkerSize',10);
xlabel("time [min]");
```

```
ylabel("wavelength [nm]");
yline(peak_shift_40(1),"k--",'LineWidth',2);
legend(["10 mW","40 mW"]);
```

Listing A.3: 40mW laser test in terms of Power output stability and spectrum (the code is the same for the 10 mW laser source)

```
clc; clear all; close all;

R25 =10000;
beta = 3450;
T0 = 25;

% R range 3.599*10^3 to 681.6
a=3.3530481*10^-3;
b=2.5420230*10^-4;
c=1.1431163*10^-6;
d=-6.9383563*10^-8;


Ibias=1.2;
%% characteristic curve for butterfly laser
Power = [0 0 0 0 0 0.4 3.38 23 67 76 91 96]; %mW
Voltage = [0 0 0.1 0.2 0.3 0.4 0.45 0.5 0.55 0.57 0.6 0.61]; %V
Current = (Voltage./1.2)*10^3; %mA
figure;
plot(Current,Power,"LineWidth",3);
xlabel("Current (mA)");
ylabel("Power(mW)");

%% POWER OUTPUT STABILITY FOR BUTTERFLY LASER

P1 = readmatrix('/Users/marcofranchini/Library/CloudStorage/
    OneDrive-PolitecnicodiTorino/Università/Svizzera/Tesi/
    LASER_SOURCE/Butterfly_laser/03_02_2023/1/Power.txt');
P1 = P1(:,2);

V1 = readmatrix('/Users/marcofranchini/Library/CloudStorage/
    OneDrive-PolitecnicodiTorino/Università/Svizzera/Tesi/
    LASER_SOURCE/Butterfly_laser/03_02_2023/1/Temp.txt');
V1= V1(:,4);
R1= V1./Ibias;
T1 = beta./(log(R1./(R25.*exp(-beta./T0))));
T1= T1([1:length(P1)],1);

...

figure;
plot(T1,P1*1000,"*","LineWidth",5)
```

```
39 title("Butterfly laser");
40 xlim([26.5 27]);
41 ylim([85 90]);
42 xlabel("Temperature ( C )","FontSize",50);
43 ylabel("Power (mW)","FontSize",50);
44
45 time1=[0:1:length(P1)-1]./60;
46 figure;
47 [hAx,hLine1,hLine2] = plotyy(time1,P1*1000,time1,T1);
48 xlabel("time (s)","FontSize",30);
49 ylabel(hAx(1),"Power (mW)","FontSize",30,"FontWeight","bold"); %
       left y-axis
50 ylabel(hAx(2),"Temperature ( C )","FontSize",30,"FontWeight","bold
       "); % right y-axis
51 hLine1.LineWidth=5;
52 hLine2.LineWidth=5;
53 ylim(hAx(1),[84.6 90.6]);
54 ylim(hAx(2),[26.812 26.818]);
55
56 %% whitout heatsink
57
58 figure;
59 plot(T2,P2*1000,"*","LineWidth",5)
60 title("Butterfly laser");
61 % xlim([26.5 27]);
62 % ylim([85 90]);
63 xlabel("Temperature ( C )","FontSize",50);
64 ylabel("Power (mW)","FontSize",50);
65
66 time1=[0:1:length(P2)-1]./60;
67 figure;
68 [hAx,hLine1,hLine2] = plotyy(time1,P2*1000,time1,T2);
69 xlabel("time (s)","FontSize",30);
70 ylabel(hAx(1),"Power (mW)","FontSize",30,"FontWeight","bold"); %
       left y-axis
71 ylabel(hAx(2),"Temperature ( C )","FontSize",30,"FontWeight","bold
       "); % right y-axis
72 hLine1.LineWidth=5;
73 hLine2.LineWidth=5;
74 % ylim(hAx(1),[84.6 90.6]);
75 % ylim(hAx(2),[26.812 26.818]);
76
77 cvP=(std(P1(20:end,1))/mean(P1(20:end,1)))*100;
78 cvT=(std(T1)/mean(T1))*100;
79
80
81 %% Spectrometry
```

```
S1 = readmatrix("/Users/marcofranchini/Library/CloudStorage/
    OneDrive-PolitecnicodiTorino/Università/Svizzera/Tesi/
    LASER_SOURCE/Butterfly_laser/03_02_2023/Spectrum/Subt2_16
    -03-37-061.txt");

...

Spec= [S1(:,2) S2(:,2) S3(:,2) S4(:,2) S5(:,2) S6(:,2) S7(:,2)];
lambda = S1(:,1);
fwhmx=ones(size(Spec,2),1);

for i=1:7
    vmax = max(Spec(:,i));
    vmin = min (Spec(:,i));
    %Find the half max value.
    halfMax = max(Spec(:,i)) / 2;
    % Find where the data first drops below half the max.
    index1 = find(Spec(:,i) >= halfMax, 1, 'first');
    % Find where the data last rises above half the max.
    index2 = find(Spec(:,i) >= halfMax, 1, 'last');
    fwhm = index2-index1 + 1; % FWHM in indexes
    % if you have an x vector
    fwhmx(i) = lambda(index2) - lambda(index1);
end
[M index]=max(Spec);
peak_shift=lambda(index);
plot(lambda,Spec, "LineWidth",3);
xline(532.5,'LineWidth',2,"LineStyle","--");

t=0:5:5*6;
figure;
plot(t,peak_shift, 'r.','LineWidth',10,'MarkerSize',40);
xlabel("time [min]");
ylabel("wavelength [nm]");
yline(peak_shift(1),"k--",'LineWidth',3);
```

Listing A.4: Butterfly laser test in terms of Power output stability and spectrum.

Bibliography

[1] Valdemaras Razumas, Julija Kanapienienė, Tommy Nylander, Sven Engström, and Kåre Larsson. «Electrochemical biosensors for glucose, lactate, urea, and creatinine based on enzymes entrapped in a cubic liquid crystalline phase». In: *Analytica chimica acta* 289.2 (1994), pp. 155–162 (cit. on p. 1).

[2] Petar Kassal, Jayoung Kim, Rajan Kumar, William R de Araujo, Ivana Murković Steinberg, Matthew D Steinberg, and Joseph Wang. «Smart bandage with wireless connectivity for uric acid biosensing as an indicator of wound status». In: *Electrochemistry Communications* 56 (2015), pp. 6–10 (cit. on p. 1).

[3] Martin Pumera. «Graphene in biosensing». In: *Materials today* 14.7-8 (2011), pp. 308–315 (cit. on p. 1).

[4] Kseniya V Serebrennikova, Anna N Berlina, Dmitriy V Sotnikov, Anatoly V Zherdev, and Boris B Dzantiev. «Raman scattering-based biosensing: new prospects and opportunities». In: *Biosensors* 11.12 (2021), p. 512 (cit. on p. 1).

[5] Katrin Kneipp, Harald Kneipp, Irving Itzkan, Ramachandra R Dasari, and Michael S Feld. «Ultrasensitive chemical analysis by Raman spectroscopy». In: *Chemical reviews* 99.10 (1999), pp. 2957–2976 (cit. on p. 1).

[6] Giuseppe Pezzotti. «Raman spectroscopy in cell biology and microbiology». In: *Journal of Raman Spectroscopy* 52.12 (2021), pp. 2348–2443 (cit. on p. 1).

[7] L-P Choo-Smith, HGM Edwards, H Ph Endtz, JM Kros, Freerk Heule, Hugh Barr, Joe Sam Robinson Jr, HA Bruining, and GJ Puppels. «Medical applications of Raman spectroscopy: from proof of principle to clinical implementation». In: *Biopolymers: Original Research on Biomolecules* 67.1 (2002), pp. 1–9 (cit. on p. 1).

[8] Penghui Li, Feng Long, Wanling Chen, Jing Chen, Paul K Chu, and Huaiyu Wang. «Fundamentals and applications of surface-enhanced Raman spectroscopy–based biosensors». In: *Current Opinion in Biomedical Engineering* 13 (2020), pp. 51–59 (cit. on pp. 1, 5).

[9] Ata Golparvar, Assim Boukhayma, Christian C Enz, and Sandro Carrara. «Optimized Detection of Hypoglycemic Glucose Ranges in Human Serum by Raman Spectroscopy with 532 nm Laser Excitation.» In: *PHOTOPTICS*. 2022, pp. 158–165 (cit. on p. 1).

[10] Di Wu, Yong He, Pengcheng Nie, Fang Cao, and Yidan Bao. «Hybrid variable selection in visible and near-infrared spectral analysis for non-invasive quality determination of grape juice». In: *Analytica chimica acta* 659.1-2 (2010), pp. 229–237 (cit. on p. 1).

[11] Jeon Woong Kang et al. «Direct observation of glucose fingerprint using in vivo Raman spectroscopy». In: *Science Advances* 6.4 (2020), eaay5206 (cit. on pp. 1, 25).

[12] J Banks, J McArthur, and G Gordon. «Flexible monitoring in the management of patient care processes: a pilot study.» In: *Lippincott's case management: managing the process of patient care* 5.3 (2000), pp. 94–103 (cit. on p. 1).

[13] Stephanie Soon, Hafdis Svavarsdottir, Candice Downey, and David George Jayne. «Wearable devices for remote vital signs monitoring in the outpatient setting: an overview of the field». In: *BMJ Innovations* 6.2 (2020) (cit. on p. 1).

[14] Ata Golparvar, Assim Boukhayma, Christian Enz, and Sandro Carrara. «Rapid, Sensitive and Selective Optical Glucose Sensing with Stimulated Raman Scattering (SRS)». In: *2022 IEEE International Symposium on Medical Measurements and Applications (MeMeA)*. IEEE. 2022, pp. 1–5 (cit. on p. 2).

[15] Marcin Gnyba, Janusz Smulko, Andrzej Kwiatkowski, and Paweł Wierzba. «Portable Raman spectrometer-design rules and applications». In: *Bulletin of the Polish Academy of Sciences. Technical Sciences* 59.3 (2011), pp. 325–329 (cit. on pp. 2, 24).

[16] EB Hanlon et al. «Prospects for in vivo Raman spectroscopy». In: *Physics in Medicine & Biology* 45.2 (2000), R1 (cit. on pp. 5, 73).

[17] CM Penney, LM Goldman, and M Lapp. «Raman scattering cross sections». In: *Nature Physical Science* 235.58 (1972), pp. 110–112 (cit. on p. 5).

[18] Chunfei Li. «Nonlinear optics». In: *Principles and Applications* (2017) (cit. on p. 6).

[19] Thierry Verbiest, Koen Clays, and Vincent Rodriguez. *Second-order nonlinear optical characterization techniques: an introduction*. CRC press, 2009 (cit. on p. 6).

[20] Robin R Jones, David C Hooper, Liwu Zhang, Daniel Wolverson, and Ventsislav K Valev. «Raman techniques: fundamentals and frontiers». In: *Nanoscale research letters* 14.1 (2019), pp. 1–34 (cit. on p. 6).

[21] Ambra Idone, Monica Gulmini, Anne-Isabelle Henry, Francesca Casadio, Lauren Chang, Lorenzo Appolonia, Richard P Van Duyne, and Nilam C Shah. «Silver colloidal pastes for dye analysis of reference and historical textile fibers using direct, extractionless, non-hydrolysis surface-enhanced Raman spectroscopy». In: *Analyst* 138.20 (2013), pp. 5895–5903 (cit. on p. 6).

[22] Katharina Eberhardt, Clara Stiebing, Christian Matthäus, Michael Schmitt, and Jürgen Popp. «Advantages and limitations of Raman spectroscopy for molecular diagnostics: an update». In: *Expert review of molecular diagnostics* 15.6 (2015), pp. 773–787 (cit. on p. 6).

[23] Nicolas Le Thomas, Zuyang Liu, Chupao Lin, Haolan Zhao, and Roel Baets. «Raman on-chip: current status and future tracks». In: *Integrated Optics: Devices, Materials, and Technologies XXV*. Vol. 11689. SPIE. 2021, pp. 7–17 (cit. on p. 6).

[24] Ata Golparvar, Assim Boukhayma, Timothy Loayza, Antonino Caizzone, Christian Enz, and Sandro Carrara. «Very Selective Detection of Low Physiopathological Glucose Levels by Spontaneous Raman Spectroscopy with Univariate Data Analysis». In: *BioNanoScience* 11.3 (2021), pp. 871–877 (cit. on p. 6).

[25] Mikolaj K Schmidt, Ruben Esteban, Alejandro González-Tudela, Geza Giedke, and Javier Aizpurua. «Quantum mechanical description of Raman scattering from molecules in plasmonic cavities». In: *ACS nano* 10.6 (2016), pp. 6291–6298 (cit. on p. 7).

[26] James KG Watson. «The vibration-rotation Hamiltonian of linear molecules». In: *Molecular Physics* 19.4 (1970), pp. 465–487 (cit. on p. 7).

[27] MG Raymer and IA Walmsley. «III The quantum coherence properties of stimulated Raman scattering». In: *Progress in optics*. Vol. 28. Elsevier, 1990, pp. 181–270 (cit. on p. 7).

[28] Sara Mosca, Claudia Conti, Nick Stone, and Pavel Matousek. «Spatially offset Raman spectroscopy». In: *Nature Reviews Methods Primers* 1.1 (2021), pp. 1–16 (cit. on p. 7).

[29] John R Ferraro. *Introductory raman spectroscopy*. Elsevier, 2003 (cit. on p. 8).

[30] RF Begley, AB Harvey, and Robert L Byer. «Coherent anti-Stokes Raman spectroscopy». In: *Applied physics letters* 25.7 (1974), pp. 387–390 (cit. on p. 8).

[31] Derek J. Gardiner. «Introduction to Raman Scattering». In: *Practical Raman Spectroscopy*. Ed. by Derek J. Gardiner and Pierre R. Graves. Berlin, Heidelberg: Springer Berlin Heidelberg, 1989, pp. 1–12. ISBN: 978-3-642-74040-4. DOI: 10.1007/978-3-642-74040-4_1. URL: https://doi.org/10.1007/978-3-642-74040-4_1 (cit. on p. 8).

[32] Phillip G Wilcox and Jason A Guicheteau. «Comparison of handheld Raman sensors through opaque containers». In: *Chemical, Biological, Radiological, Nuclear, and Explosives (CBRNE) Sensing XIX*. Vol. 10629. SPIE. 2018, pp. 64–69 (cit. on pp. 8, 25).

[33] Yukio Yamada and Shinpei Okawa. «Diffuse optical tomography: Present status and its future». In: *Optical Review* 21.3 (2014), pp. 185–205 (cit. on pp. 8, 13, 16).

[34] Joseph M Schmitt. «Optical coherence tomography (OCT): a review». In: *IEEE Journal of selected topics in quantum electronics* 5.4 (1999), pp. 1205–1215 (cit. on pp. 8, 13).

[35] Vega Pradana Rachim and Wan-Young Chung. «Wearable-band type visible-near infrared optical biosensor for non-invasive blood glucose monitoring». In: *Sensors and Actuators B: Chemical* 286 (2019), pp. 173–180 (cit. on pp. 8, 11, 12).

[36] Paola Pinti, Clarisse Aichelburg, Sam Gilbert, Antonia Hamilton, Joy Hirsch, Paul Burgess, and Ilias Tachtsidis. «A review on the use of wearable functional near-infrared spectroscopy in naturalistic environments». In: *Japanese Psychological Research* 60.4 (2018), pp. 347–373 (cit. on pp. 8, 10).

[37] Y Hoshi. «Hemodynamic signals in fNIRS». In: *Progress in brain research* 225 (2016), pp. 153–179 (cit. on p. 8).

[38] Chuen Wai Lee, Robert J Cooper, and Topun Austin. «Diffuse optical tomography to investigate the newborn brain». In: *Pediatric research* 82.3 (2017), pp. 376–386 (cit. on pp. 8, 17).

[39] Ali Kassab et al. *Multichannel wearable f NIRS-EEG system for long-term clinical monitoring*. Tech. rep. Wiley Online Library, 2018 (cit. on p. 9).

[40] Sophie K Piper, Arne Krueger, Stefan P Koch, Jan Mehnert, Christina Habermehl, Jens Steinbrink, Hellmuth Obrig, and Christoph H Schmitz. «A wearable multi-channel fNIRS system for brain imaging in freely moving subjects». In: *Neuroimage* 85 (2014), pp. 64–71 (cit. on p. 9).

[41] L Bokobza. «Near infrared spectroscopy». In: *Journal of Near Infrared Spectroscopy* 6.1 (1998), pp. 3–17 (cit. on p. 11).

[42] Joyce A Wahr, Kevin K Tremper, Satwant Samra, and David T Delpy. «Near-infrared spectroscopy: theory and applications». In: *Journal of cardiothoracic and vascular anesthesia* 10.3 (1996), pp. 406–418 (cit. on p. 11).

[43] Thomas Wriedt. «A review of elastic light scattering theories». In: *Particle & Particle Systems Characterization: Measurement and Description of Particle Properties and Behavior in Powders and Other Disperse Systems* 15.2 (1998), pp. 67–74 (cit. on p. 11).

[44] Katsuhiko Maruo, Mitsuhiro Tsurugi, Jakusei Chin, Tomohiro Ota, Hidenobu Arimoto, Yukio Yamada, Mamoru Tamura, Masataka Ishii, and Yukihiro Ozaki. «Noninvasive blood glucose assay using a newly developed near-infrared system». In: *IEEE Journal of selected topics in quantum electronics* 9.2 (2003), pp. 322–330 (cit. on pp. 11, 12).

[45] Yong Fan and Fan Zhang. «A new generation of NIR-II probes: lanthanide-based nanocrystals for bioimaging and biosensing». In: *Advanced Optical Materials* 7.7 (2019), p. 1801417 (cit. on p. 12).

[46] Nathaniel E Kallmyer, Mohamed Seddik Abdennadher, Sparsh Agarwal, Rebecca Baldwin-Kordick, Rachel L Khor, Alex S Kooistra, Erica Peterson, Marshall D McDaniel, and Nigel F Reuel. «Inexpensive Near-Infrared Fluorimeters: Enabling Translation of nIR-Based Assays to the Field». In: *Analytical Chemistry* 93.11 (2021), pp. 4800–4808 (cit. on p. 12).

[47] Jeroen Lammertyn, Ann Peirs, Josse De Baerdemaeker, and Bart Nicolaı. «Light penetration properties of NIR radiation in fruit with respect to non-destructive quality assessment». In: *Postharvest Biology and Technology* 18.2 (2000), pp. 121–132 (cit. on p. 13).

[48] Paolo Renati, Zoltan Kovacs, Antonella De Ninno, and Roumiana Tsenkova. «Temperature dependence analysis of the NIR spectra of liquid water confirms the existence of two phases, one of which is in a coherent state». In: *Journal of Molecular Liquids* 292 (2019), p. 111449 (cit. on p. 13).

[49] Marena Manley. «Near-infrared spectroscopy and hyperspectral imaging: non-destructive analysis of biological materials». In: *Chemical Society Reviews* 43.24 (2014), pp. 8200–8214 (cit. on p. 13).

[50] David A Boas, Dana H Brooks, Eric L Miller, Charles A DiMarzio, Misha Kilmer, Richard J Gaudette, and Quan Zhang. «Imaging the body with diffuse optical tomography». In: *IEEE signal processing magazine* 18.6 (2001), pp. 57–75 (cit. on p. 13).

[51] Elisabetta Maria Frijia et al. «Functional imaging of the developing brain with wearable high-density diffuse optical tomography: a new benchmark for infant neuroimaging outside the scanner environment». In: *NeuroImage* 225 (2021), p. 117490 (cit. on pp. 13, 15, 17).

[52] Yoko Hoshi and Yukio Yamada. «Overview of diffuse optical tomography and its clinical applications». In: *Journal of biomedical optics* 21.9 (2016), pp. 091312–091312 (cit. on p. 14).

[53] AH Hielscher, AY Bluestone, GS Abdoulaev, AD Klose, J Lasker, M Stewart, U Netz, and dan J Beuthan. «Near-infrared diffuse optical tomography». In: *Disease markers* 18.5-6 (2002), pp. 313–337 (cit. on pp. 14, 17).

[54] Gultekin Gulsen, Ozlem Birgul, Mehmet Burcin Unlu, Roshanak Shafiiha, and Orhan Nalcioglu. «Combined diffuse optical tomography (DOT) and MRI system for cancer imaging in small animals». In: *Technology in cancer research & treatment* 5.4 (2006), pp. 351–363 (cit. on p. 14).

[55] Hamid Dehghani, Subhadra Srinivasan, Brian W Pogue, and Adam Gibson. «Numerical modelling and image reconstruction in diffuse optical tomography». In: *Philosophical Transactions of the Royal Society A: Mathematical, Physical and Engineering Sciences* 367.1900 (2009), pp. 3073–3093 (cit. on p. 14).

[56] Benjamin W Zeff, Brian R White, Hamid Dehghani, Bradley L Schlaggar, and Joseph P Culver. «Retinotopic mapping of adult human visual cortex with high-density diffuse optical tomography». In: *Proceedings of the National Academy of Sciences* 104.29 (2007), pp. 12169–12174 (cit. on pp. 14, 16).

[57] Theodore J Huppert, Maria Angela Franceschini, and David A Boas. «Non-invasive imaging of cerebral activation with diffuse optical tomography». In: *In Vivo Optical Imaging of Brain Function. 2nd edition* (2009) (cit. on p. 14).

[58] Justin C Brown, Sharon D Solomon, Susan B Bressler, Andrew P Schachat, Cathy DiBernardo, and Neil M Bressler. «Detection of diabetic foveal edema: contact lens biomicroscopy compared with optical coherence tomography». In: *Archives of ophthalmology* 122.3 (2004), pp. 330–335 (cit. on p. 16).

[59] Liangbo Shen, Brenton Keller, Oscar Carrasco-Zevallos, Christian Viehland, Paramjit K Bhullar, Gar Waterman, Anthony N Kuo, Cynthia A Toth, and Joseph A Izatt. «Oculus Rift® as a head tracking, stereoscopic head mounted display for intra-operative OCT in ophthalmic surgery». In: *Investigative Ophthalmology & Visual Science* 57.12 (2016), pp. 1701–1701 (cit. on p. 16).

[60] Ruchire Eranga Wijesinghe et al. «Optical coherence tomography-integrated, wearable (backpack-type), compact diagnostic imaging modality for in situ leaf quality assessment». In: *Applied optics* 56.9 (2017), pp. D108–D114 (cit. on pp. 16, 17).

[61] Adrit Rao and Harvey A Fishman. «OCTAI: Smartphone-based Optical Coherence Tomography Image Analysis System». In: *2021 IEEE World AI IoT Congress (AIIoT)*. IEEE. 2021, pp. 0072–0076 (cit. on p. 16).

[62] Stephan Beer, Severin Waldis, and Peter Seitz. «Video-rate optical coherence tomography imaging with smart pixels». In: *European Conference on Biomedical Optics*. Optica Publishing Group. 2003, 5140_69 (cit. on p. 17).

[63] Jaeheung Kim, Sang Min Park, Gyeong Hun Kim, Minyoung Park, Jeesu Kim, and Chang-Seok Kim. «Full-field optical coherence tomography using tunable-path-difference source for three-dimensional multi-layered imaging with enhanced signal-to-noise ratio». In: *Optics and Lasers in Engineering* 147 (2021), p. 106727 (cit. on p. 17).

[64] Shengting Cao, Xinwen Yao, Nischal Koirala, Brigitta Brott, Silvio Litovsky, Yuye Ling, and Yu Gan. «Super-resolution technology to simultaneously improve optical & digital resolution of optical coherence tomography via deep learning». In: *2020 42nd Annual International Conference of the IEEE Engineering in Medicine & Biology Society (EMBC)*. IEEE. 2020, pp. 1879–1882 (cit. on p. 18).

[65] Reena Chopra, Siegfried K Wagner, and Pearse A Keane. «Optical coherence tomography in the 2020s—outside the eye clinic». In: *Eye* 35.1 (2021), pp. 236–243 (cit. on p. 18).

[66] George Kaklamanos, Eugenio Aprea, and Georgios Theodoridis. «11 - Mass spectrometry: principles and instrumentation». In: *Chemical Analysis of Food (Second Edition)*. Ed. by Yolanda Pico. Second Edition. Academic Press, 2020, pp. 525–552. ISBN: 978-0-12-813266-1. DOI: https://doi.org/10.1016/B978-0-12-813266-1.00011-5. URL: https://www.sciencedirect.com/science/article/pii/B9780128132661000115 (cit. on p. 18).

[67] Jinmo Kim, Donggeun Jung, Yongsup Park, Yongki Kim, Dae Won Moon, and Tae Geol Lee. «Quantitative analysis of surface amine groups on plasma-polymerized ethylenediamine films using UV–visible spectroscopy compared to chemical derivatization with FT-IR spectroscopy, XPS and TOF-SIMS». In: *Applied surface science* 253.9 (2007), pp. 4112–4118 (cit. on p. 18).

[68] Jeanette M Cardamone. «Investigating the microstructure of keratin extracted from wool: Peptide sequence (MALDI-TOF/TOF) and protein conformation (FTIR)». In: *Journal of molecular structure* 969.1-3 (2010), pp. 97–105 (cit. on p. 18).

[69] Martin Tanner, Yannick Bussweiler, and Olga Borovinskaya. «Laser ablation and inductively coupled plasma–time-of-flight mass spectrometry—A powerful combination for high-speed multielemental imaging on the micrometer scale». In: *Spectroscopy* 32.5 (2017), pp. 14–20 (cit. on p. 18).

[70] Lei Zhu, Tom Liew, and TC Chong. «A novel method for film thickness measurement of perfluoropolyether lubricant by secondary ion mass spectroscopy». In: *Applied surface science* 189.1-2 (2002), pp. 53–58 (cit. on p. 18).

[71] Luca Cappellin et al. «PTR-ToF-MS and data mining methods: a new tool for fruit metabolomics». In: *Metabolomics* 8 (2012), pp. 761–770 (cit. on p. 18).

[72] Facundo M Fernández, Robert B Cody, Michael D Green, Christina Y Hampton, Rose McGready, Sivong Sengaloundeth, Nicholas J White, and Paul N Newton. «Characterization of solid counterfeit drug samples by desorption electrospray ionization and direct-analysis-in-real-time coupled to time-of-flight mass spectrometry». In: *ChemMedChem: Chemistry Enabling Drug Discovery* 1.7 (2006), pp. 702–705 (cit. on p. 18).

[73] Andrew A Mills, Brian M Siller, Michael W Porambo, Manori Perera, Holger Kreckel, and Benjamin J McCall. «Ultra-sensitive high-precision spectroscopy of a fast molecular ion beam». In: *The Journal of chemical physics* 135.22 (2011), p. 224201 (cit. on p. 18).

[74] Kássio MG Lima, Ketan B Gajjar, Pierre L Martin-Hirsch, and Francis L Martin. «Segregation of ovarian cancer stage exploiting spectral biomarkers derived from blood plasma or serum analysis: ATR-FTIR spectroscopy coupled with variable selection methods». In: *Biotechnology progress* 31.3 (2015), pp. 832–839 (cit. on p. 18).

[75] Yi-Tzu Cho, Hung Su, Wen-Jeng Wu, Deng-Chyang Wu, Ming-Feng Hou, Chao-Hung Kuo, and Jentaie Shiea. «Biomarker Characterization by MALDI-TOF/MS». In: *Advances in clinical chemistry* 69 (2015), pp. 209–254 (cit. on p. 18).

[76] Chia-Yen Cha, Gerd Ganteför, and Wolfgang Eberhardt. «New experimental setup for photoelectron spectroscopy on cluster anions». In: *Review of scientific instruments* 63.12 (1992), pp. 5661–5666 (cit. on p. 18).

[77] Alain Brunelle and Olivier Laprévote. «Recent advances in biological tissue imaging with time-of-flight secondary ion mass spectrometry: polyatomic ion sources, sample preparation, and applications». In: *Current pharmaceutical design* 13.32 (2007), pp. 3335–3343 (cit. on p. 18).

[78] L Zhang et al. «Mechanical properties of filled antimonide skutterudites». In: *Materials Science and Engineering: B* 170.1-3 (2010), pp. 26–31 (cit. on p. 19).

[79] Ryan M Smith and Mark A Arnold. «Terahertz time-domain spectroscopy of solid samples: principles, applications, and challenges». In: *Applied Spectroscopy Reviews* 46.8 (2011), pp. 636–679 (cit. on p. 19).

[80] Caroline B Reid, George Reese, Adam P Gibson, and Vincent P Wallace. «Terahertz time-domain spectroscopy of human blood». In: *IEEE Transactions on Terahertz Science and Technology* 3.4 (2013), pp. 363–367 (cit. on p. 19).

[81] BM Fischer, M Walther, and P Uhd Jepsen. «Far-infrared vibrational modes of DNA components studied by terahertz time-domain spectroscopy». In: *Physics in Medicine & Biology* 47.21 (2002), p. 3807 (cit. on p. 19).

[82] Changlei Wang, Jixian Gong, Qirong Xing, Yanfeng Li, Feng Liu, Xueming Zhao, Lu Chai, Chingyue Wang, and Aleksei M Zheltikov. «Application of terahertz time-domain spectroscopy in intracellular metabolite detection». In: *Journal of Biophotonics* 3.10-11 (2010), pp. 641–645 (cit. on p. 19).

[83] Zhenqi Zhu, Yujing Bian, Xun Zhang, Ruonan Zeng, and Bin Yang. «Evaluation of formation and proportion of secondary structure in γ-polyglutamic acid by terahertz time-domain spectroscopy». In: *Spectrochimica Acta Part A: Molecular and Biomolecular Spectroscopy* 271 (2022), p. 120940 (cit. on p. 19).

[84] Madoka Nakamura, Makoto Okano, and Shinichi Watanabe. «Real-Time Monitoring of Structural Changes in Poly (lactic acid) during Thermal Treatment by High-Speed Terahertz Time-Domain Spectroscopy for Nondestructive Inspection». In: *ACS Applied Polymer Materials* 1.11 (2019), pp. 3008–3016 (cit. on p. 19).

[85] Rong Zhao, Bin Zou, Guling Zhang, Dongqian Xu, and Yuping Yang. «High-sensitivity identification of aflatoxin B1 and B2 using terahertz time-domain spectroscopy and metamaterial-based terahertz biosensor». In: *Journal of Physics D: Applied Physics* 53.19 (2020), p. 195401 (cit. on p. 19).

[86] Daniel M Mittleman, Rune Hylsberg Jacobsen, Ramesh Neelamani, Richard G Baraniuk, and Martin C Nuss. «Gas sensing using terahertz time-domain spectroscopy». In: *Applied Physics B* 67.3 (1998), pp. 379–390 (cit. on p. 19).

[87] Nicholas Klokkou, Jon Gorecki, James S Wilkinson, and Vasilis Apostolopoulos. «Artificial neural networks for material parameter extraction in terahertz time-domain spectroscopy». In: *Optics Express* 30.9 (2022), pp. 15583–15595 (cit. on p. 19).

[88] Weihao Fang, Xiaoqing Lv, Zhengtai Ma, Jian Liu, Weihua Pei, and Zhaoxin Geng. «A flexible terahertz metamaterial biosensor for cancer cell growth and migration detection». In: *Micromachines* 13.4 (2022), p. 631 (cit. on p. 20).

[89] *Bravo handheld raman spectrometer*. URL: `https://www.bruker.com/en/products-and-solutions/infrared-and-raman/raman-spectrometers/bravo-handheld-raman-spectrometer.html` (cit. on pp. 21, 27).

[90] Fanyu Zeng, Wendi Duan, Bin Zhu, Taotao Mu, Lianqing Zhu, Jinhong Guo, and Xing Ma. «based versatile surface-enhanced Raman spectroscopy chip with smartphone-based Raman analyzer for point-of-care application». In: *Analytical chemistry* 91.1 (2018), pp. 1064–1070 (cit. on p. 21).

[91] Fanyu Zeng, Taotao Mou, Chengchen Zhang, Xiaoqing Huang, Bing Wang, Xing Ma, and Jinhong Guo. «based SERS analysis with smartphones as Raman spectral analyzers». In: *Analyst* 144.1 (2019), pp. 137–142 (cit. on p. 21).

[92] Taotao Mu, Su Li, Huanhuan Feng, Chengchen Zhang, Bing Wang, Xing Ma, Jinhong Guo, Bill Huang, and Lianqing Zhu. «High-sensitive smartphone-based Raman system based on cloud network architecture». In: *IEEE Journal of Selected Topics in Quantum Electronics* 25.1 (2018), pp. 1–6 (cit. on pp. 21, 22).

[93] Taotao Mu, Shengnan Wang, Tianshu Li, Bing Wang, Xing Ma, Bill Huang, Lianqing Zhu, and Jinhong Guo. «Detection of pesticide residues using Nano-SERS chip and a smartphone-based Raman sensor». In: *IEEE Journal of Selected Topics in Quantum Electronics* 25.2 (2018), pp. 1–6 (cit. on pp. 21–23).

[94] Lynn Chandler, Bill Huang, and Tao Tao Mu. «A smart handheld Raman spectrometer with cloud and AI deep learning algorithm for mixture analysis». In: *Next-Generation Spectroscopic Technologies XII*. Vol. 10983. SPIE. 2019, pp. 20–28 (cit. on pp. 21–23).

[95] Liping Huang et al. «Rapid, label-free histopathological diagnosis of liver cancer based on Raman spectroscopy and deep learning». In: *Nature Communications* 14.1 (2023), pp. 1–14 (cit. on pp. 21, 22).

[96] MS Wróbel. «Non-invasive blood glucose monitoring with Raman spectroscopy: prospects for device miniaturization». In: *IOP Conference Series: Materials Science and Engineering*. Vol. 104. 1. IOP publishing. 2016, p. 012036 (cit. on p. 24).

[97] Emad L Izake. «Forensic and homeland security applications of modern portable Raman spectroscopy». In: *Forensic science international* 202.1-3 (2010), pp. 1–8 (cit. on p. 24).

[98] Silvia Innocenti, Diego Quintero Balbas, Luca Pezzati, Raffaella Fontana, and Jana Striova. «Portable Sequentially Shifted Excitation Raman Spectroscopy to Examine Historic Powders Enclosed in Glass Vials». In: *Sensors* 22.9 (2022), p. 3560 (cit. on p. 24).

[99] Keith Carron and Rick Cox. *Qualitative analysis and the answer box: a perspective on portable Raman spectroscopy*. 2010 (cit. on p. 24).

[100] Yi Zheng, Xiangping Zhu, Zhe Wang, Zongyu Hou, Fei Gao, Rongzhi Nie, Xiaoxia Cui, Jiangbo She, and Bo Peng. «Noninvasive blood glucose detection using a miniature wearable Raman spectroscopy system». In: *Chinese Optics Letters* 15.8 (2017), p. 083001 (cit. on p. 24).

[101] David S Moore and R Jason Scharff. «Portable Raman explosives detection». In: *Analytical and bioanalytical chemistry* 393.6 (2009), pp. 1571–1578 (cit. on p. 24).

[102] J Jehlička, P Vıtek, HGM Edwards, M Heagraves, and T Čapoun. «Application of portable Raman instruments for fast and non-destructive detection of minerals on outcrops». In: *Spectrochimica Acta Part A: Molecular and Biomolecular Spectroscopy* 73.3 (2009), pp. 410–419 (cit. on p. 24).

[103] Neethu Emmanuel, Raji B Nair, Bini Abraham, and Karuvath Yoosaf. *Fabricating a low-cost Raman spectrometer to introduce students to spectroscopy basics and applied instrument design*. 2021 (cit. on pp. 25, 31, 32).

[104] Edgar Guevara, Juan Carlos Torres-Galván, Francisco Javier González, Claudia Luevano-Contreras, Claudio Cayetano Castillo-Martınez, and Miguel G Ramırez-Elıas. «Feasibility of Raman spectroscopy as a potential in vivo tool to screen for pre-diabetes and diabetes». In: *Journal of biophotonics* 15.9 (2022), e202200055 (cit. on p. 25).

[105] Rishikesh Pandey, Santosh Kumar Paidi, Tulio A Valdez, Chi Zhang, Nicolas Spegazzini, Ramachandra Rao Dasari, and Ishan Barman. «Noninvasive monitoring of blood glucose with Raman spectroscopy». In: *Accounts of chemical research* 50.2 (2017), pp. 264–272 (cit. on p. 25).

[106] *Portables Raman-Spectrometer Cora 100*. URL: https://www.anton-paar.com/ch-it/prodotti/dettagli/spettrometro-raman-portatile-cora-100/ (cit. on p. 27).

[107] Eun Hye Koh, Won-Chul Lee, Yeong-Jin Choi, Joung-Il Moon, Jinah Jang, Sung-Gyu Park, Jaebum Choo, Dong-Ho Kim, and Ho Sang Jung. «A wearable surface-enhanced Raman scattering sensor for label-free molecular detection». In: *ACS Applied Materials & Interfaces* 13.2 (2021), pp. 3024–3032 (cit. on pp. 28, 30).

[108] Hilal Torul, Hakan Çiftçi, Demet Çetin, Zekiye Suludere, Ismail Hakkı Boyacı, and Uğur Tamer. «Paper membrane-based SERS platform for the determination of glucose in blood samples». In: *Analytical and bioanalytical chemistry* 407.27 (2015), pp. 8243–8251 (cit. on p. 28).

[109] Dan Wang et al. «Dual-functional ultrathin wearable 3D particle-in-cavity SF-AAO-Au SERS sensors for effective sweat glucose and lab-on-glove pesticide detection». In: *Sensors and Actuators B: Chemical* 359 (2022), p. 131512 (cit. on p. 28).

[110] Guoran Liu, Zhimei Mu, Jing Guo, Ke Shan, Xiaoyi Shang, Jing Yu, and Xiu Liang. «Surface-enhanced Raman scattering as a potential strategy for wearable flexible sensing and point-of-care testing non-invasive medical diagnosis». In: *Frontiers in Chemistry* 10 (2022) (cit. on p. 28).

[111] Michael Chung, William H Skinner, Colin Robert, Colin J Campbell, René M Rossi, Vasileios Koutsos, and Norbert Radacsi. «Fabrication of a Wearable Flexible Sweat pH Sensor Based on SERS-Active Au/TPU Electrospun Nanofibers». In: *ACS Applied Materials & Interfaces* 13.43 (2021), pp. 51504–51518 (cit. on p. 28).

[112] Xue-Jian Li, Yuan-Ting Li, Hai-Xin Gu, Peng-Fei Xue, Li-Xia Qin, and Sheng Han. «A wearable screen-printed SERS array sensor on fire-retardant fibre gloves for on-site environmental emergency monitoring». In: *Analytical methods* 14.8 (2022), pp. 781–788 (cit. on p. 28).

[113] Dan Luo, Haibo Sun, Qianqian Li, Xin Niu, Yin He, and Hao Liu. «Flexible Sweat Sensors: From Films to Textiles». In: *ACS sensors* (2023) (cit. on p. 28).

[114] Timothy TX Ong, Ewan W Blanch, and Oliver AH Jones. «Surface Enhanced Raman Spectroscopy in environmental analysis, monitoring and assessment». In: *Science of The Total Environment* 720 (2020), p. 137601 (cit. on p. 29).

[115] Surya P Singh, Soumavo Mukherjee, Luis H Galindo, Peter TC So, Ramachandra Rao Dasari, Uzma Zubair Khan, Raghuraman Kannan, Anandhi Upendran, and Jeon Woong Kang. «Evaluation of accuracy dependence of Raman spectroscopic models on the ratio of calibration and validation points for non-invasive glucose sensing». In: *Analytical and bioanalytical chemistry* 410 (2018), pp. 6469–6475 (cit. on p. 29).

[116] Anne Trafton. *Shining a light - literally - on diabetes*. URL: `https://news.mit.edu/2010/glucose-monitor-0809` (cit. on p. 29).

[117] Limei Liu et al. «Highly scalable, wearable surface-enhanced Raman spectroscopy». In: *arXiv preprint arXiv:2203.09042* (2022) (cit. on p. 30).

[118] Mustapha Hajjou, Yanyan Qin, Sanford Bradby, Daniel Bempong, and Patrick Lukulay. «Assessment of the performance of a handheld Raman device for potential use as a screening tool in evaluating medicines quality». In: *Journal of pharmaceutical and biomedical analysis* 74 (2013), pp. 47–55 (cit. on p. 31).

[119] Anel Beganović, Thomas Nuener, Florian Meischl, Stefan E Stuppner, Matthias Rainer, Günther K Bonn, and Christian W Huck. «Quantification of melamine in infant formula using a handheld Raman spectrometer–Performance boost with customized Arduino-controlled rotation setup». In: *Talanta* 209 (2020), p. 120488 (cit. on pp. 31, 32).

[120] Onur Aydogan and Erol Tasal. «Designing and building a 3D printed low cost modular Raman spectrometer». In: *CERN IdeaSquare Journal of Experimental Innovation* 2.2 (2018), pp. 3–14 (cit. on pp. 31, 33).

[121] Khan Nouman, Zaman Asim, and Khan Qasim. «Comprehensive study on performance of PID controller and its applications». In: *2018 2nd IEEE Advanced Information Management, Communicates, Electronic and Automation Control Conference (IMCEC)*. IEEE. 2018, pp. 1574–1579 (cit. on p. 37).

[122] Carl Knospe. «PID control». In: *IEEE Control Systems Magazine* 26.1 (2006), pp. 30–31 (cit. on p. 37).

[123] Yun Li, Kiam Heong Ang, and Gregory CY Chong. «PID control system analysis and design». In: *IEEE Control Systems Magazine* 26.1 (2006), pp. 32–41 (cit. on p. 37).

[124] Rakesh P Borase, DK Maghade, SY Sondkar, and SN Pawar. «A review of PID control, tuning methods and applications». In: *International Journal of Dynamics and Control* 9 (2021), pp. 818–827 (cit. on p. 38).

[125] Yongsheng Cui, Yu Yin, Yulin Wu, Xuxiang Ni, Xiuda Zhang, and Huimin Yan. «Research of high power and stable laser in portable Raman spectrometer based on SHINERS technology». In: *International Symposium on Photoelectronic Detection and Imaging 2013: Imaging Spectrometer Technologies and Applications*. Vol. 8910. SPIE. 2013, pp. 384–393 (cit. on p. 38).

[126] E Farsad, SP Abbasi, A Goodarzi, and MS Zabihi. «Experimental parametric investigation of temperature effects on 60W-QCW diode laser». In: *International Journal of Electronics and Communication Engineering* 5.11 (2011), pp. 1467–1472 (cit. on pp. 38–40).

[127] DS Patil and DK Gautam. «Analysis of effect of temperature on ZnSSe based blue laser diode characteristics at 507 nm wavelength». In: *Physica B: Condensed Matter* 344.1-4 (2004), pp. 140–146 (cit. on pp. 38–40).

[128] Duarte Valério and José Sá Da Costa. «Tuning of fractional PID controllers with Ziegler–Nichols-type rules». In: *Signal processing* 86.10 (2006), pp. 2771–2784 (cit. on p. 38).

[129] Adawiya J Haider. «Effect of Temperature Tuning on Diode Laser Performance». In: *spectrum* 1 (2009), p. 2 (cit. on pp. 39, 40).

[130] Walter Koechner. «Thermal lensing in a Nd: YAG laser rod». In: *Applied optics* 9.11 (1970), pp. 2548–2553 (cit. on p. 39).

[131] PJ Hardman, WA Clarkson, GJ Friel, Markus Pollnau, and DC Hanna. «Energy-transfer upconversion and thermal lensing in high-power end-pumped Nd: YLF laser crystals». In: *IEEE Journal of Quantum Electronics* 35.4 (1999), pp. 647–655 (cit. on p. 39).

[132] Yuhua Huang, Ying Zhou, Charlie Doyle, and Shin-Tson Wu. «Tuning the photonic band gap in cholesteric liquid crystals by temperature-dependent dopant solubility». In: *Optics Express* 14.3 (2006), pp. 1236–1242 (cit. on p. 40).

[133] Chenyi Su, Binglin Shen, Xingqi Xu, Chunsheng Xia, and Bailiang Pan. «Simulation and analysis of the time evolution of laser power and temperature in static pulsed XPALs». In: *High Power Laser Science and Engineering* 7 (2019), e44 (cit. on p. 40).

[134] Dongliang Zhao and Gang Tan. «A review of thermoelectric cooling: materials, modeling and applications». In: *Applied thermal engineering* 66.1-2 (2014), pp. 15–24 (cit. on p. 41).

[135] Reiyu Chein and Guanming Huang. «Thermoelectric cooler application in electronic cooling». In: *Applied Thermal Engineering* 24.14-15 (2004), pp. 2207–2217 (cit. on p. 41).

[136] Guodong Li, Javier Garcia Fernandez, David Alberto Lara Ramos, Vida Barati, Nicolas Perez, Ivan Soldatov, Heiko Reith, Gabi Schierning, and Kornelius Nielsch. «Integrated microthermoelectric coolers with rapid response time and high device reliability». In: *Nature Electronics* 1.10 (2018), pp. 555–561 (cit. on p. 41).

[137] H Bottner. «Micropelt miniaturized thermoelectric devices: small size, high cooling power densities, short response time». In: *ICT 2005. 24th International Conference on Thermoelectrics, 2005.* Ieee. 2005, pp. 1–8 (cit. on p. 41).

[138] Abu Raihan Mohammad Siddique, Shohel Mahmud, and Bill Van Heyst. «A comprehensive review on a passive (phase change materials) and an active (thermoelectric cooler) battery thermal management system and their limitations». In: *Journal of Power Sources* 401 (2018), pp. 224–237 (cit. on p. 41).

[139] Seyed Mohsen Pourkiaei, Mohammad Hossein Ahmadi, Milad Sadeghzadeh, Soroush Moosavi, Fathollah Pourfayaz, Lingen Chen, Mohammad Arab Pour Yazdi, and Ravinder Kumar. «Thermoelectric cooler and thermoelectric generator devices: A review of present and potential applications, modeling and materials». In: *Energy* 186 (2019), p. 115849 (cit. on p. 42).

[140] Mohamed Hamid Elsheikh, Dhafer Abdulameer Shnawah, Mohd Faizul Mohd Sabri, Suhana Binti Mohd Said, Masjuki Haji Hassan, Mohamed Bashir Ali Bashir, and Mahazani Mohamad. «A review on thermoelectric renewable energy: Principle parameters that affect their performance». In: *Renewable and sustainable energy reviews* 30 (2014), pp. 337–355 (cit. on p. 42).

[141] Muhammad Saleheen Aftab and Muhammad Shafiq. «Adaptive PID controller based on Lyapunov function neural network for time delay temperature control». In: *2015 IEEE 8th GCC Conference & Exhibition.* IEEE. 2015, pp. 1–6 (cit. on p. 44).

[142] Thabiso Peter Mpofu, Cephas Mawere, and Macdonald Mukosera. «The impact and application of 3D printing technology». In: (2014) (cit. on p. 53).

[143] Han Jin, Yasmin Shibli Abu-Raya, and Hossam Haick. «Advanced materials for health monitoring with skin-based wearable devices». In: *Advanced healthcare materials* 6.11 (2017), p. 1700024 (cit. on p. 53).

[144] Kyuyoung Kim, Jungrak Choi, Yongrok Jeong, Incheol Cho, Minseong Kim, Seunghwan Kim, Yongsuk Oh, and Inkyu Park. «Highly sensitive and wearable liquid metal-based pressure sensor for health monitoring applications: integration of a 3D-printed microbump array with the microchannel». In: *Advanced healthcare materials* 8.22 (2019), p. 1900978 (cit. on p. 53).

[145] Ashish Kalkal, Sumit Kumar, Pramod Kumar, Rangadhar Pradhan, Magnus Willander, Gopinath Packirisamy, Saurabh Kumar, and Bansi Dhar Malhotra. «Recent advances in 3D printing technologies for wearable (bio) sensors». In: *Additive Manufacturing* 46 (2021), p. 102088 (cit. on p. 53).

[146] Mallikarjuna N Nadagouda, Megan Ginn, and Vandita Rastogi. «A review of 3D printing techniques for environmental applications». In: *Current opinion in chemical engineering* 28 (2020), pp. 173–178 (cit. on p. 53).

[147] Tuan D Ngo, Alireza Kashani, Gabriele Imbalzano, Kate TQ Nguyen, and David Hui. «Additive manufacturing (3D printing): A review of materials, methods, applications and challenges». In: *Composites Part B: Engineering* 143 (2018), pp. 172–196 (cit. on p. 54).

[148] Tessa Jane Gordelier, Philipp Rudolf Thies, Louis Turner, and Lars Johanning. «Optimising the FDM additive manufacturing process to achieve maximum tensile strength: A state-of-the-art review». In: *Rapid Prototyping Journal* 25.6 (2019), pp. 953–971 (cit. on pp. 55, 56).

[149] Mahshid Padash, Christian Enz, and Sandro Carrara. «Microfluidics by additive manufacturing for wearable biosensors: A review». In: *Sensors* 20.15 (2020), p. 4236 (cit. on pp. 56, 58).

[150] Michael P Chae, Warren M Rozen, Paul G McMenamin, Michael W Findlay, Robert T Spychal, and David J Hunter-Smith. «Emerging applications of bedside 3D printing in plastic surgery». In: *Frontiers in surgery* 2 (2015), p. 25 (cit. on pp. 56–58).

[151] Bruce K Gale, Alexander R Jafek, Christopher J Lambert, Brady L Goenner, Hossein Moghimifam, Ugochukwu C Nze, and Suraj Kumar Kamarapu. «A review of current methods in microfluidic device fabrication and future commercialization prospects». In: *Inventions* 3.3 (2018), p. 60 (cit. on p. 56).

[152] Steve Upcraft and Richard Fletcher. «The rapid prototyping technologies». In: *Assembly Automation* 23.4 (2003), pp. 318–330 (cit. on pp. 57, 58).

[153] Orhan Gülcan, Kadir Günaydın, and Aykut Tamer. «The state of the art of material jetting—a critical review». In: *Polymers* 13.16 (2021), p. 2829 (cit. on p. 57).

[154] Rajat Chaudhary, Paride Fabbri, Enrico Leoni, Francesca Mazzanti, Raziyeh Akbari, and Carlo Antonini. «Additive manufacturing by digital light processing: a review». In: *Progress in Additive Manufacturing* (2022), pp. 1–21 (cit. on p. 58).

[155] Alexey Unkovskiy, Franziska Schmidt, Florian Beuer, Ping Li, Sebastian Spintzyk, and Pablo Kraemer Fernandez. «Stereolithography vs. direct light processing for rapid manufacturing of complete denture bases: An in vitro accuracy analysis». In: *Journal of Clinical Medicine* 10.5 (2021), p. 1070 (cit. on p. 58).

[156] *SLA vs. DLP: Guide to resin 3D printers*. URL: `https://formlabs.com/blog/resin-3d-printer-comparison-sla-vs-dlp/` (cit. on pp. 58–60).

[157] *The difference between DLP and SLA 3D printing technology*. Sept. 2022. URL: `https://manufactur3dmag.com/difference-dlp-sla/` (cit. on p. 59).

[158] Jiumeng Zhang, Qipeng Hu, Shuai Wang, Jie Tao, and Maling Gou. «Digital light processing based three-dimensional printing for medical applications». In: *International journal of bioprinting* 6.1 (2020) (cit. on p. 59).

[159] YL Yap and WY Yeong. «Additive manufacture of fashion and jewellery products: a mini review: This paper provides an insight into the future of 3D printing industries for fashion and jewellery products». In: *Virtual and Physical Prototyping* 9.3 (2014), pp. 195–201 (cit. on p. 59).

[160] Wei-Shao Lin, Bryan T Harris, John Pellerito, and Dean Morton. «Fabrication of an interim complete removable dental prosthesis with an in-office digital light processing three-dimensional printer: A proof-of-concept technique». In: *The Journal of prosthetic dentistry* 120.3 (2018), pp. 331–334 (cit. on p. 59).

[161] Zhi Zhao, Xiaoxiao Tian, and Xiaoyan Song. «Engineering materials with light: recent progress in digital light processing based 3D printing». In: *Journal of Materials Chemistry C* 8.40 (2020), pp. 13896–13917 (cit. on p. 60).

[162] Haoyuan Quan, Ting Zhang, Hang Xu, Shen Luo, Jun Nie, and Xiaoqun Zhu. «Photo-curing 3D printing technique and its challenges». In: *Bioactive materials* 5.1 (2020), pp. 110–115 (cit. on p. 60).

[163] Yong Yu, Prasanna V Ramachandran, and Meng C Wang. «Shedding new light on lipid functions with CARS and SRS microscopy». In: *Biochimica et Biophysica Acta (BBA)-Molecular and Cell Biology of Lipids* 1841.8 (2014), pp. 1120–1129 (cit. on p. 72).

[164] Nilam C Shah, Olga Lyandres, Joseph T Walsh, Matthew R Glucksberg, and Richard P Van Duyne. «Lactate and sequential lactate- glucose sensing using surface-enhanced Raman spectroscopy». In: *Analytical chemistry* 79.18 (2007), pp. 6927–6932 (cit. on pp. 72, 73).

[165] W Ranjith Premasiri, Richard H Clarke, and M Edward Womble. «Urine analysis by laser Raman spectroscopy». In: *Lasers in Surgery and Medicine: The Official Journal of the American Society for Laser Medicine and Surgery* 28.4 (2001), pp. 330–334 (cit. on pp. 72, 73).

[166] Belén Hernández, Yves-Marie Coıc, Fernando Pflüger, Sergei G Kruglik, and Mahmoud Ghomi. «All characteristic Raman markers of tyrosine and tyrosinate originate from phenol ring fundamental vibrations». In: *Journal of Raman Spectroscopy* 47.2 (2016), pp. 210–220 (cit. on p. 73).

[167] Belén Hernández, Fernando Pflüger, Sergei G Kruglik, and Mahmoud Ghomi. «Characteristic Raman lines of phenylalanine analyzed by a multiconformational approach». In: *Journal of Raman Spectroscopy* 44.6 (2013), pp. 827–833 (cit. on p. 73).

[168] Sanda Boca, Dumitrita Rugina, Adela Pintea, Nicolae Leopold, and Simion Astilean. «Designing gold nanoparticle-ensembles as surface enhanced Raman scattering tags inside human retinal cells». In: *Journal of Nanotechnology* 2012 (2012) (cit. on p. 73).

[169] Cassiano Junior Saatkamp, Maurıcio Liberal de Almeida, Jeyse Aliana Martins Bispo, Antonio Luiz Barbosa Pinheiro, Adriana Barrinha Fernandes, and Landulfo Silveira Jr. «Quantifying creatinine and urea in human urine through Raman spectroscopy aiming at diagnosis of kidney disease». In: *Journal of biomedical optics* 21.3 (2016), pp. 037001–037001 (cit. on p. 73).